New Control Algorithms for the Robust Operation and Stabilization of Active Distribution Networks

by

Maher Abdelkhalek Azzouz Abdelkhalek

A thesis
presented to the University of Waterloo
in fulfillment of the
thesis requirement for the degree of
Doctor of Philosophy
in
Electrical and Computer Engineering

Waterloo, Ontario, Canada, 2015

AUTHOR'S DECLARATION

I hereby declare that I am the sole author of this thesis. This is a true copy of the thesis, including any required final revisions, as accepted by my examiners.

I understand that my thesis may be made electronically available to the public.

Abstract

The integration of renewable distributed generation units (DGs) alters distribution systems so that rather than having passive structures, with unidirectional power flow, they become active distribution networks (ADNs), with multi-directional power flow. While numerous technical, economic, and environmental benefits are associated with the shift toward ADNs, this transition also represents important control challenges from the perspective of both the supervisory and primary control of DGs. Voltage regulation is considered one of the main operational control challenges that accompany a high penetration of renewable DGs. The intermittent nature of renewable energy sources, such as wind and solar energy, can significantly change the voltage profile of the system and can interact negatively with conventional schemes for controlling on-load tap changers (OLTCs). Another factor is the growing penetration of plug-in electric vehicles (PEVs), which creates additional stress on voltage control devices due to their stochastic and concentrated power profiles. These combined generation and load power profiles can lead to overvoltages, undervoltages, increases in system losses, excessive tap operation, infeasible solutions (hunting) with respect to OLTCs, and/or limits on the penetration of either PEVs or DGs. With regard to the dynamic control level, DG interfaces are typically applied using power electronic converters, which lack physical inertia and are thus sensitive to variations and uncertainties in the system parameters. Grid impedance (or admittance), which has a substantial effect on the performance and stability of primary DG controllers, is nonlinear, time-varying, and not passive in nature. In addition, constant-power loads (CPLs), such as those interfaced through power electronic converters, are also characterized by inherited negative impedance that results in destabilizing effects, creating instability and damping issues.

Motivated by these challenges, the research presented in this thesis was conducted with the primary goal of proposing new control algorithms for both the supervisory and primary control of DGs, and ultimately of developing robust and stable ADNs. Achieve this objective entailed the completion of four studies:

Study#1: Development of a coordinated fuzzy-based voltage regulation scheme with reduced communication requirements

Study#2: Integration of PEVs into the voltage regulation scheme through the implementation of a vehicle-to-grid reactive power (V2GQ) support strategy

Study#3: Creation of an estimation tool for multivariable grid admittance that can be used to develop adaptive controllers for DGs

Study#4: Development of self-tuning primary DG controllers based on the estimated grid admittance so that stable performance is guaranteed under time-varying DG operating points (dispatched by the schemes developed in Study#1 and Study#2) and under changing grid impedance (created by network reconfiguration and load variations).

As the first research component, a coordinated fuzzy-based voltage regulation scheme for OLTCs and DGs has been proposed. The primary reason for applying fuzzy logic is that it provides the ability to address the challenges associated with imperfect information environments, and can thus reduce communication requirements. The proposed regulation scheme consists of three fuzzy-based control algorithms. The first control algorithm was designed to enable the OLTC to mitigate the effects of DGs on the voltage profile. The second algorithm was created to provide reactive power sharing among DGs, which will relax OLTC tap operation. The third algorithm is aimed at partially curtailing active power levels in DGs so as to restore a feasible solution that will satisfy OLTC requirements. The proposed fuzzy algorithms offer the advantage of effective voltage regulation with relaxed tap operation and with utilization of only the estimated minimum and maximum system voltages. Because no optimization algorithm is required, it also avoids the numerical instability and convergence problems associated with centralized approaches. OPAL real-time simulators (RTS) were employed to run test simulations in order to demonstrate the success of the proposed fuzzy algorithms in a typical distribution network.

The second element, a V2GQ strategy, has been developed as a means of offering optimal coordinated voltage regulation in distribution networks with high DG and PEV penetration. The proposed algorithm employs PEVs, DGs, and OLTCs in order to satisfy the PEV charging demand and grid voltage requirements while maintaining relaxed tap operation and minimum curtailment of DG active power. The voltage regulation problem is formulated as nonlinear programming and consists of three consecutive stages, with each successive stage applying the output from the preceding stage as constraints. The task of the first stage is to maximize the energy delivered to PEVs in order to ensure PEV owner satisfaction. The second stage maximizes the active power extracted from the DGs, and the third stage minimizes any deviation of the voltage from its nominal value through the use of available PEV and DG reactive power. The primary implicit objective of the third stage problem is the relaxation of OLTC tap operation. This objective is addressed by replacing

conventional OLTC control with a proposed centralized controller that utilizes the output of the third stage to set its tap position. The effectiveness of the proposed algorithm in a typical distribution network has been validated in real time using an OPAL RTS in a hardware-in-the loop (HiL) application.

The third part of the research has resulted in the proposal of a new multivariable grid admittance identification algorithm with adaptive model order selection as an ancillary function to be applied in inverter-based DG controllers. Cross-coupling between the $d-$axis and $q-$axis grid admittance necessitates multivariable estimation. To ensure persistence of excitation (PE) for the grid admittance, sensitivity analysis is first employed as a means of determining the injection of controlled voltage pulses by the DG. Grid admittance is then estimated based on the processing of the extracted grid dynamics by the refined instrumental variable for continuous-time identification (RIVC) algorithm. Unlike nonparametric identification algorithms, the proposed RIVC algorithm provides a parametric multivariable model of grid admittance, which is essential for designing adaptive controllers for DGs. HiL applications using OPAL RTS have been utilized for validating the proposed algorithm for both grid-connected and isolated ADNs.

The final section of the research is a proposed adaptive control algorithm for optimally reshaping DG output impedance so that system damping and bandwidth are maximized. Such adaptation is essential for managing variations in grid impedance and changes in DG operating conditions. The proposed algorithm is generic so that it can be applied for both grid-connected and islanded DGs. It involves three design stages. First, the multivariable DG output impedance is derived mathematically and verified using a frequency sweep identification method. The grid impedance is also estimated so that the impedance stability criteria can be formulated. In the second stage, multi-objective programming is formulated using the ε -constraint method in order to maximize system damping and bandwidth. As a final stage, the solutions provided by the optimization stage are employed for training an adaptation scheme based on a neural network (NN) that tunes the DG control parameters online. The proposed algorithm has been validated in both grid-connected and isolated distribution networks, with the use of OPAL RTS and HiL applications.

Acknowledgements

First and foremost, I would like to thank God whose guidance lead me this far.

My sincere gratitude goes to my advisor Professor Ehab El-Saadany for his professional guidance, valuable advice, continual support and encouragement shown throughout the period of this research. My appreciation and thanks are also extended to my PhD committee members: Professor Ramadan El-Shatshat, Professor Kankar Bhattacharya, and Professor Fathy Ismail. Thanks to my external examiner, Professor Luiz Lopes, for coming from Concordia University to referee this thesis.

My parents, Abdelkhalek Azzouz and Hamida El-Berri, always receive my deepest thanks, and endless appreciation. My research would not have been possible without their help, their constant support and encouragement, and their blessed wishes and prayers.

I would like to express my special thanks to my wife, Samah Abbas, for whom I would never find the right words to express my gratitude for her endless patience, understanding, and support during all these years of my PhD studies. Also, I would like to thank my son Mohammad and my daughter Malak who always give me love, happiness, and energy.

I wish also to thank my colleagues and friends, Ali Hooshyar, Amr Said, and Mostafa Shaaban, whose fruitful discussions, advices, and support inspired me during my PhD.

Last but not least, I would like to express my appreciation and thanks to Professor Abdel-Latif Elshafei whose support, interest, assistance, and sincere advice during my Master's degree studies at Cairo University had shaped and refined my research character.

Dedication

To my beloved father, Abdelkhalek,

To my beloved mother, Hamida,

To my beloved wife, Samah,

To my sweetheart son, Mohammad,

To my darling daughter, Malak,

in recognition of your endless love, support, and encouragement.

Table of Contents

List of Figures

List of Tables

Nomenclature

a	Transformer turns ratio
ADN	Active distribution network
A_E	Magnitude
a_o	Nominal turns ratio
ARMA	Autoregressive–moving-average
C_f	Capacitance of the DG interfacing filter
C_g	Grid equivalent capacitance
$\mathcal{CH}_{(\mathrm{i})}$	Set of chargers
COC	Centralized OLTC controller
CPL	Constant-power load
CT	Continuous-time
DB	Dead band
DFT	Discrete Fourier transform
DG	Distributed generation unit
DNO	Distribution network operator
DSP	Digital signal processor
DT	Discrete-time
$\tilde{e}$	Chirp excitation signal
$E_{BAT(ch_{(i)})}$	Battery capacity
$E_{D(\mathrm{ch(i),t})}$	Energy delivered to PEVs
E_{dq}	Pulse excitation signals in the $d-q$ frame
EKF	Extended Kalman filter
E_m	Amplitude of the chirp signal
ESS	Energy storage systems
$f_{(ch_{(i)},t)}$	Battery charging/discharging function

f_1	End frequency of the chirp excitation signal
$f_c(p)$	State-variable filter with cut-off frequency α
f_o	Start frequency of the chirp excitation signal
FOC	Fuzzy-based OLTC controller
FPC	Fuzzy-based DG active power curtailment
FPGA	Field-programmable gate array
FQC	Fuzzy-based reactive power control
G_1, G_2, G_3, G_4	Transfer-function components of Y_{Grid} matrix
GA	Genetic algorithms
G_f	Low-pass filter for the DG output power (i.e., $G_f = \omega_p / (s+\omega_p)$)
G_i	DG current controller (i.e., $G_i = K_{ip} + K_{ii} / s$)
G_p	DG power controller (i.e., $G_p = K_{pp} + K_{pi} / s$)
G_{pll}	PLL controller (i.e., $G_{pll} = K_{pll,p} + K_{pll,i} / s$)
G_v	DG voltage controller (i.e., $G_v = K_{vp} + K_{vi} / s$)
$G_{v,dc}$	DC-link voltage controller (i.e., $G_{v,dc} = K_{vp,dc} + K_{vi,dc} / s$)
G_{vf}	PLL voltage low-pass filter (i.e., $G_{vf} = \omega_v / (s+\omega_v)$)
HiL	Hardware-in-the-loop
$I_{(l,t)}$	Current through line $l \in \mathcal{L}$
$\mathcal{I}$	Identity matrix
$\mathcal{I}_b$	Set of system buses
$\mathcal{I}_{DG}$	Set of buses with DG connections
I_d, I_q	$d-q$ components of the DG inverter current
IMU	Impedance measurement unit
"*ini*"	Superscript denoting the initial value of a variable
I_o	DG output current at the PCC
I_{od}, I_{oq}	$d-q$ components of the DG output current at the PCC
$\tilde{I}_{odq}$	$d-q$ components of the perturbed DG output current at the PCC

I_{OLTC}	OLTC current
$\mathcal{I}_{PEV}$	Set of buses with PEV charger connections
IPM	Instrumental product matrix
I_s	Source current
K	Vector containing the DG controller gains
K_c	Scaling factor for the FOC
K_{ip}, K_{ii}	Proportional and integral gains of the DG current controller
K_L , K_U	Lower and upper boundaries of K
K_P	Scaling factor for the FPC
$K_{pll,p}, K_{pll,i}$	Proportional and integral gains of the PLL controller
K_{pp}, K_{pi}	Proportional and integral gains of the DG power controller
K_Q	Scaling factor for the FQC
K_{vp}, K_{vi}	Proportional and integral gains of the DG voltage controller
$\mathcal{L}$	Set of system lines
LDC	Line drop compensators
L_f	Inductance of the DG interfacing filter
L_g	Grid equivalent inductance
LS	Least squares
$\lvert M \rvert$	Magnitude of the modulation index M
m	Static droop gain for active power
m_1, m_2, m_3, m_4	Numerator orders for $G_1, G_2, G_3,$ and G_4
"max", "min"	Subscripts denoting the maximum and minimum values of a variable
M_d, M_q	$d-q$ components of the modulation index M
MF	Membership function
MISO	Multi-input-single-output
MMO	Multi-master operation
MPPT	Maximum power point tracking
n	Static droop gain for reactive power

$n_{(t)}$	Tap position
N	Acquired samples of the system output and input
n_d, n_q	Denominator orders for (G_1, G_2) and (G_3, G_4)
N_g	Total number of DGs connected to a network
$N_{\max}$	Maximum number of taps in one direction from zero compensation
NN	Neural-network
n_p	Number of estimated parameters
"o"	Superscript denoting the steady-state value of a variable
OLTC	On-load tap changer
p	Differential operator
PCC	Point of common coupling
$P_{CH(ch_{(i)},t)}$	Charging power limit
PCL	Primary control level
P_{cov}	Error covariance matrix
PE	Persistence of excitation
PEV	Plug-in electric vehicle
$pf_{(i)}$	DG power factor
PHiL	Power hardware-in-the-loop
$P_{L(i,t)}, P_{G(i,t)}$	Load and generated active powers at bus i
PLL	Phase-locked loop
$P_{NL(i,t)}$	Active power of a normal load at bus i
P_o, p_o	Average and instantaneous DG active powers at the PCC
$P_{o(i,t)}^{MPPT}$	DG available power extracted by a MPPT algorithm
$P_{o(i,t)}^{PEV}$	PEV active power
$P_{o(i,t)}^{R}$	Reached DG Power
$P_{o(i)}^{ref}$	DG active power reference
PV	Photovoltaic

PWM	Pulse width modulation
q^{-1}	Backward shift operator
$Q_{L(i,t)}$, $Q_{G(i,t)}$	Load and generated reactive powers at bus i
$Q_{NL(i,t)}$	Reactive power of a normal load at bus i
Q_o, q_o	Average and instantaneous DG reactive powers at the PCC
$Q_{o(i)}^{\text{Limit}}$	Minimum DG reactive power limit
$Q_{o(i,t)}^{PEV}$	PEV reactive power
$Q_{o(i)}^{pf}$	DG reactive power limit due to power factor constraint
$Q_{o(i)}^{ref}$	DG reactive power reference
$Q_{o(i)}^{S}$	DG reactive power limit due to converter rating constraint
$Q_{o(i)}^{V}$	DG reactive power limit due to converter voltage constraint
RCP	Rapid control prototyping
Re(.)	Real part of
"ref"	Superscript denoting the reference value of a variable
R_f	Resistance of the DG interfacing filter
R_g	Grid equivalent resistance
RIVC	Refined instrumental variable for continuous-time identification
R_T^2	Coefficient of determination
RTS	Real-time simulator
S	Sensitivity matrix
s	Laplace operator
S_{base}	Base power
SCL	Supervisory control level
S_{ij}	Sensitivity transfer function
SiL	Software-in-the-loop
SMO	Single master operation
SNR	Signal-to-noise ratio

SOC	State-of-charge
$SOC^{D}_{(ch_{(i)},t)}$	Desired SOC
$SOC^{F}_{(ch_{(i)},t)}$	Final SOC
$SOC^{I}_{(ch_{(i)},t)}$	Initial SOC
$SOC^{R}_{(ch_{(i)},t)}$	Reached SOC
$S^{PEV}_{o(i,t)}$	Rated power of the PEV converter
t	Time instant
T	Duration of the chirp excitation signal
T_d	Controller time delay
T_E	Width of pulse excitation signals
T_m	Mechanical time delay
TPA	Toronto Parking Authority
$u_i(t)$	i^{th} input of a MISO system
$V_{(i,t)}$	Magnitude of a bus voltage
V^*	No-load DG reference voltage
V2G	Vehicle-to-grid
V2GQ	Vehicle-to-grid reactive power support
$V^{\max}_{c(i)}$	Maximum DG converter voltage
V_{dc}	DC-link voltage
V_d, V_q	$d-q$ components of the DG inverter voltage
V^*_{dq}	Converter reference voltages in the $d-q$ frame
V_F	Output of FQC algorithm
V_g	Grid voltage
V_k	Target point voltage
$\tilde{V}_k$	Estimated target point voltage
V_{Lower}	Standard lower voltage limit (i.e., 0.95 pu)

$V_{\max}^{f}$	Maximum voltage of a feeder
$V_{\max}^{sys}$	System maximum voltage
$V_{\min}$, $V_{\max}$	Maximum and minimum voltage limits
$V_{\min}^{f}$	Minimum voltage of a feeder
$V_{\min}^{sys}$	System minimum voltage
V_o	DG output voltage at the PCC
V_{od}, V_{oq}	$d-q$ components of the DG output voltage at the PCC
$\tilde{V}_{odq}$	$d-q$ components of the perturbed DG output voltage at the PCC
V_s	Source voltage
VSC	Voltage source converters
V_{Upper}	Standard upper voltage limit (i.e., 1.05 pu)
$X_{(i)}$	Total reactance of the DG interfacing transformer and filter
$\mathbb{X}_{(ch_{(i)},t)}$	Vector of the charger decisions
$x(t)$	Noise-free output of a MISO system
X_{eq}	Network equivalent reactance
X_{od} , X_{oq}	$d-q$ components of the noise-free DG output currents
$Y_{(i,j)}$	Magnitude of element (i, j) in the Y-bus admittance matrix
Y_{DG}	DG output admittance matrix
$\mathrm{Y}_{\mathrm{Grid}}$	Grid admittance matrix
YIC	Young's information criterion
$\mathrm{Y}_{\mathrm{Load}}$	Load admittance matrix
Y_s, Y_l	Source and load admittances
Y_T	Transformer series admittance
"z"	Subscript denoting a control zone
Z_{DG}	DG output impedance matrix
$\mathrm{Z}_{\mathrm{Grid}}$	Grid impedance matrix

Z_s, Z_l	Source and load impedances
γ	Decision variables of V2GQ
$\delta_{(i,t)}$	Angle of a bus voltage
Δ	Small perturbation of a variable
Δa	Step change of a_o
ΔT	Algorithm execution time
Δt_{conv}	Converter response time
ΔV	Voltage error of deviation
$\Delta V_{\max}^{DG_{(i)}}$	Difference between the DG voltage and upper voltage limit
$\Delta V_{\min}^{ESS_{(i)}}$	Difference between the lower voltage limit and ESS voltage
ΔV_{sys}	Difference between the system maximum and minimum voltages
$\varepsilon_{dq}(t_k)$	$d-q$ additive noise
$\hat{\xi}$	Damping ratio of the dominant eigenvalue
$\eta_{CH(ch(i))}$	Charging efficiency
θ	Angle in radians
θ_e	Estimated parameters of a MISO system
$\theta_{(i,j)}$	Angle of element (i, j) in the Y-bus admittance matrix
$\hat{\theta}_{(1)}$	Initial Estimate of θ_e
λ_i	Eigenvalue of the system
$\hat{\sigma}$	Real part of the dominant eigenvalue
$\hat{\sigma}^2$	Variance of the model residuals
$\hat{\sigma}_y^2$	Variance of the output signal
τ_o	Time constant of OLTC controller
τ_i	Time constant of the current control loop
$\phi_{(\mathcal{F})}$	Regression vector obtained using a filter $\mathcal{F}$
Φ(s)	Characteristic equation of the system

$\varphi_{(i)}$	DG active power curtailment factor
$\varphi^{*}_{(i)}$	FPC Output
ω	Gird frequency
ω_o	Grid nominal frequency (i.e., 377 rad/s)
ω^{*}	No-load DG reference frequency
ω_p	Cut-off frequency of the power low-pass filter
ω_v	Cut-off frequency of the voltage low-pass filter

Chapter 1
Introduction and Objectives

1.1 Preface

Ongoing rapid advances in power electronics and communication technologies are facilitating the development of small-scale distributed generation (DG) sources, which represent a deregulated paradigm. The dramatic growth in demand for electricity over the last decade has led to a corresponding increase in interest in the integration of additional DGs. This trend has altered distribution systems so that their passive structures, with unidirectional power flow, have shifted, and they are becoming active distribution networks (ADNs), with multi-directional power flow [1]–[3]. DGs are typically integrated into ADNs via two modes of operation: grid connected and islanding (microgrid) [4], [5], as illustrated in Figure 1.1. In grid-connected mode, DGs operate in a current injection manner to supply the grid with active and reactive powers, even though the DGs are not responsible for setting the system voltage and frequency, which are governed primarily by the main grid. The DG units can also participate in power quality and power factor improvements [6]. On the other hand, in microgrid operating mode, a small portion of the network is isolated from the main gain and is fed by a cluster of DGs that share system loading and ensure that the voltage and frequency of the microgrid remains within standard limits.

The transition to ADNs has resulted in a number of benefits: 1) required system upgrades can be deferred because power can be supplied during peak demands, thus releasing line congestion; 2) efficiency is improved through the reduction of system losses; 3) the cost of purchasing electricity is lower; and 4) greenhouse gas emissions are decreased because of the incorporation of renewable DG sources and the implementation of combined heating and power plants [5], [7]–[9]. DGs can also be placed near load centres, offering reliable low-cost power options for commercial loads [10]. On the other hand, the intermittent nature of renewable DG power, such as that derived from wind and solar sources, can significantly change the voltage profile of a system and interfere with the conventional control schemes governing on-load tap changers (OLTCs) [11], [12]. Such interference may lead to overvoltages, undervoltages, increases in system losses, and abnormal wear in the OLTCs due to excessive tapping action. The majority of DGs in ADNs are equipped with power-electronic converters that lack the physical inertia provided naturally by conventional generators. An additional

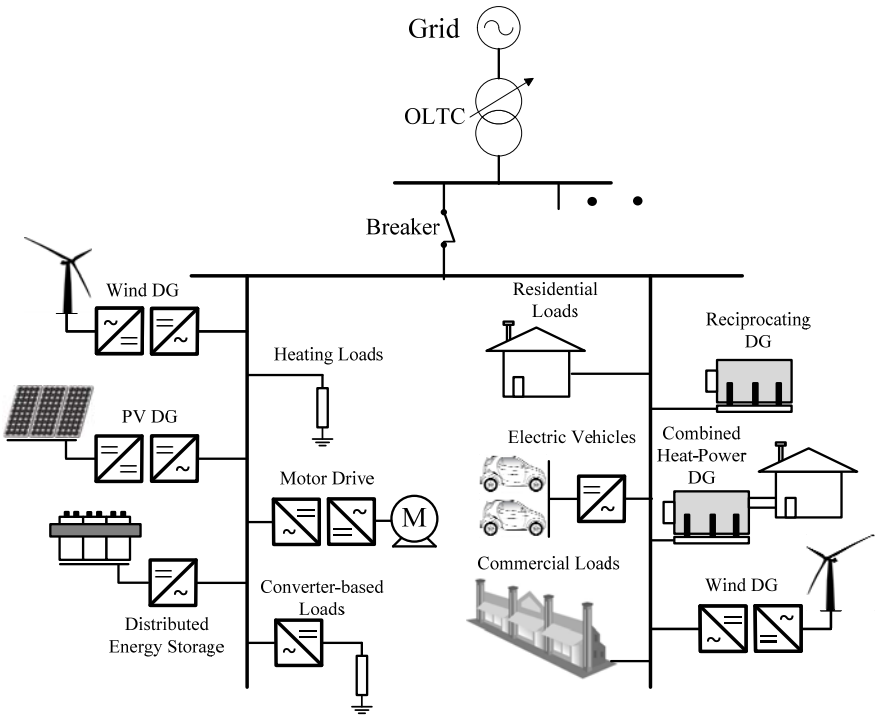

Figure 1.1: Basic ADN structure

factor is that the stability of DGs is dependent on the impedance encountered by the inverter at the interface (i.e., the grid impedance). Such impedance can vary due to grid configurations, cable overload, and temperature effects as well as load variations. These drawbacks make ADNs critically sensitive to disturbances that may be initiated due to changes in the DG operating point and variations in the grid impedance.

1.2 Research Motivation

The uncertainty and dynamic nature of ADNs has created challenges with respect to DG supervisory and dynamic control performance. From a supervisory control perspective, difficulties with voltage regulation appear to be due to the probabilistic nature of renewable DGs and the growing penetration of plug-in electric vehicles (PEVs). From a primary (dynamic) control perspective, uncertainties related to grid impedance can cause system stability to deteriorate, with a negative impact on the dynamic control of DG performance. Since DG impedance is nonlinear, the performance of the primary DG controllers is highly dependent on the DG operating points that are dispatched by the supervisory control.

Seamless and flexible integration of DGs within ADNs requires solutions for a number of control challenges if the potential benefits of implementing ADNs are to be realized. Of these challenges, the following are among the most important:

1. Coordinated fuzzy-logic control algorithms with minimal communication requirements are required in order to 1) achieve effective voltage regulation in the presence of intermittent renewable DG sources, 2) reduce stress on the OLTCs, 3) maximize the active power injection from the DGs, and 4) avoid the numerical instability and convergence problems associated with centralized voltage regulation schemes. Fuzzy logic can be viewed as a tool for emulating human mental capabilities because it can provide rational decisions in an environment of imprecision, uncertainty, and incomplete information: in short, in an environment characterized by imperfect information. ADN voltage regulation can be considered such an environment because not all states in the system are observable. Fuzzy logic controllers can also map nonlinear, multivariable, and heuristic relationships between their input and output, thus offering a high degree of controllability.

2. No vehicle-to-grid reactive power (V2GQ) support strategy exists that can take into account the self-objectives of voltage control devices, such as the requirement for OLTC tap operation to be relaxed so that equipment life is extended, PEV owners' need to maximize their state-of-charge (SOC), and the desire on the part of DG owners to reduce their active power curtailment. The integration of DGs changes the voltage profile significantly and complicates voltage regulation because 1) the voltage trend fails to descend from the substation to the feeder terminal so that a fixed target point (reference) is no longer valid, and 2) voltage estimation, which is based on local measurements, becomes inaccurate in the presence of highly intermittent renewable sources, such as wind and photovoltaics (PV). The integration of PEVs amplifies the stochastic nature of the problem, which diminishes the accuracy of a voltage estimation that is based on local measurements. Inferior voltage estimation can lead to incorrect OLTC decisions, which may result in overvoltages, undervoltages, and excessive wear and tear on the OLTCs. The problem is exacerbated if both an overvoltage and an undervoltage occur simultaneously, a scenario that occurs when some feeders are prone to overvoltages due to a high degree of DG penetration, while others are subject to undervoltages during instances of high loading, such as those that occur with PEV charging. In such cases, the OLTC will produce two contradicting solutions that will

create a hunting problem. An optimal coordinated voltage regulation algorithm is therefore required in order to facilitate a high penetration of both DGs and PEVs, while maintaining relaxed OLTC operation.

3. An accurate grid impedance estimation tool is needed for impedance stability assessment and the effective design of adaptive DG controllers. Previous identification algorithms have been based on the assumption that grid admittance can be represented by a combination of passive elements: R_g, L_g, and C_g, which form a passive model. The growing penetration of inverter-based DGs and loading means that this assumption is no longer sufficiently accurate. Grid impedance is dependent not just on passive elements but also on other factors related to DG and constant-power load (CPL) impedances, which are nonlinear, time-varying, and not passive in nature. Grid admittance must therefore be represented by an active model with a time-varying model structure. The estimation tool should persistently excite the grid impedance dynamics in order to guarantee convergence, and should also avoid over-parameterization. An over-parameterized model tends to increase computational time and can also fail to capture the underlying dynamics represented by excited grid impedance.

4. A further imperative is the development of adaptive DG controllers that can take into account the uncertainty inherent in grid impedance as well as variations in DG operating points, which are governed by the supervisory control level (SCL). With respect to DG adaptive control design, in an effort to simplify the analysis, previously proposed DG control algorithms either ignore the effect of grid impedance on system stability or neglect the resistance of the grid impedance. DG controller gains are also not optimally designed with regard to increasing the system bandwidth and damping. With respect to assessing system stability and designing DG controllers, impedance stability methods are preferred because they divide the system under study into interconnected DG and grid subsystems, offering benefits not available with detailed eigenvalue stability analysis: 1) they avoid the remodeling of the entire network and the repetition of the stability analysis when the grid impedance changes or when more DGs or loads are connected, and 2) they do not require detailed information about network components, such as DG and load parameters, which are often unavailable [4]. If the grid impedance is estimated and the DG output impedance is derived from its design specifications, the DG output impedance can be reshaped according to the

impedance stability criteria in order to maintain system stability and enhance the dynamic performance of the DGs.

1.3 Research Objectives

The ultimate goal of this research was to improve the operational and dynamic performance of ADNs through the development of new control algorithms that can guarantee effective voltage regulation and stability in the presence of network disturbances and uncertainties. The creation of the algorithms was directed primarily at the supervisory and primary DG control levels and was motivated by the previously discussed challenges associated with ADNs. The specific research objectives, which are illustrated in Figure 1.2., can be summarized as follows:

1- Development of coordinated fuzzy-based voltage regulation algorithms with minimal communication requirements for ADNs characterized by a high penetration of renewable DGs

2- Development of an optimal coordinated voltage regulation scheme for ADNs that have a high penetration of PEVs and DGs

3- Development of a multivariable grid impedance (admittance) identification tool for assessing the impedance stability of ADNs

4- Development of an algorithm for reshaping DG output impedance to provide optimal and adaptive tuning of primary DG controllers

1.4 Thesis Organization

The remainder of this thesis is organized as follows:

Chapter 2 provides background and a survey of the literature related to operational and dynamic control algorithms for ADNs.

Chapter 3 presents the proposed coordinated fuzzy logic algorithms that provide effective voltage regulation with minimal communication requirements.

Chapter 4 introduces the proposed optimal coordinated voltage regulation algorithm, which utilizes PEV reactive power and facilitates the achievement of the self-objective of each voltage control device.

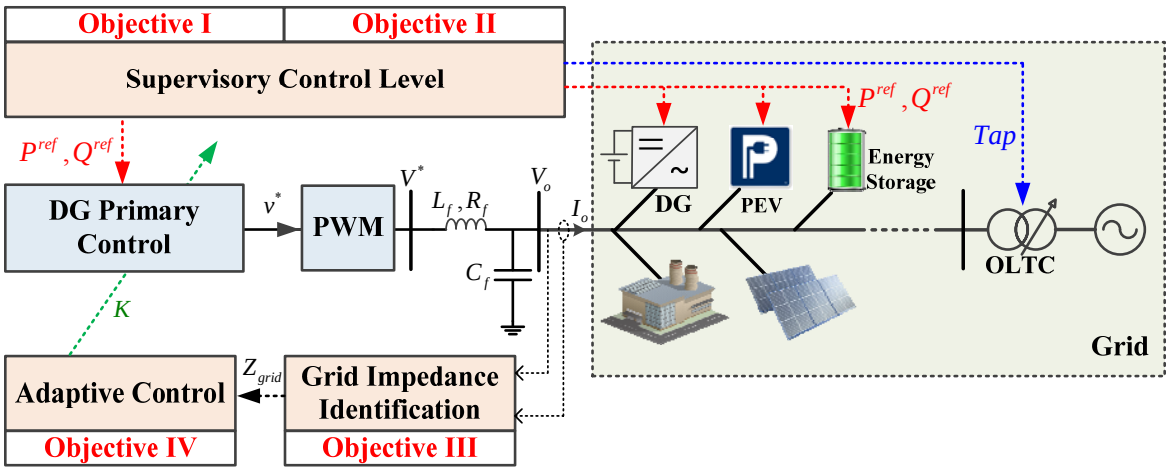

Figure 1.2: Thesis objectives

Chapter 5 explains the proposed multivariable grid admittance (impedance) identification algorithm, which is used as a tool for assessing impedance stability and for designing adaptive DG controllers.

Chapter 6 provides details about the proposed algorithm for reshaping DG output impedance, which enables optimal tuning of the adaptive DG controllers under variations in grid impedance and time-varying DG operating conditions.

Chapter 7 presents the thesis conclusions and contributions as well as suggestions for future work.

Chapter 2
Background and Literature Review

2.1 Introduction

ADNs must be able to perform demand side management individually and solve energy problems so that they can increase flexibility and reliability. Based on their ADN interface, DGs can be classified as 1) rotary DGs, in which rotary machines are connected directly to the grid without a power-electronic interface, or 2) converter-based DGs, which require a power electronic interface. The relatively high penetration of converter-based DGs has resulted in ADN control strategies and dynamic behaviour that differ significantly from those of conventional power systems [4].

The power flow control of a DG interface is dependent on whether the DG is dispatchable or non-dispatchable. With dispatchable units, the supervisory control system sends the set points (references) to the DG power control loops, such as in reciprocating DGs. However, non-dispatchable units usually operate according to a maximum power point tracking (MPPT) algorithm, as in variable-speed wind turbines and PV systems.

2.1.1 DG Control Structure

Due to the revolution in power electronics technology and the control flexibility of converter-based DGs, this type of DG plays an important role in the formation of ADNs. The primary control objective of converter-based DGs is the regulation of their active and reactive output power through control of the current output from the converter. As indicated in Figure 2.1, DG control strategies can be categorized as operating in either grid-connected or islanded (microgrid) mode. Each of these categories can be subdivided according to whether the grid control strategy is interactive or non-interactive [4].

A. Grid-connected mode

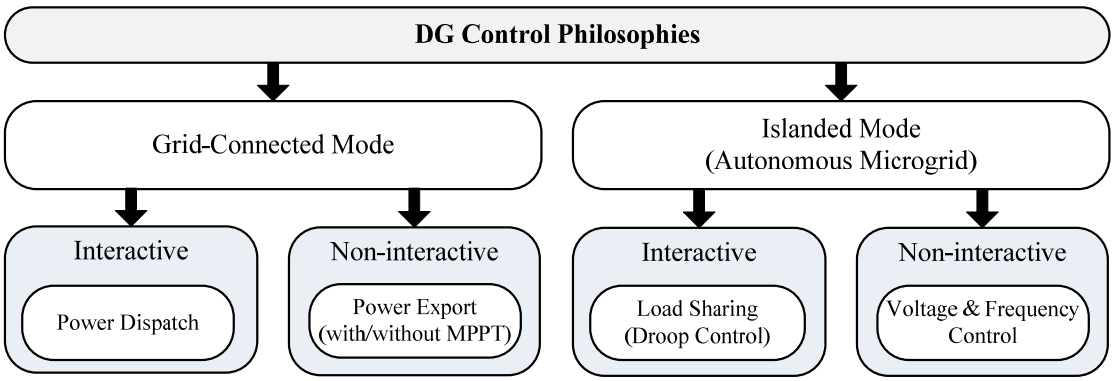

Figure 2.1: DG control philosophies for different operating modes

A phase-locked loop (PLL) is typically used as a means of synchronizing the DG output voltage and controlled current in the $d-q$ reference frame. The PLL measures the DG voltage at the point of common coupling (PCC) and outputs its frequency and angle, which are used for implementing the current control strategy in the synchronous frame, thus allowing independent control of the active and reactive powers of the DG.

In interactive grid-connected mode, DG reference currents are generated in order to inject dispatchable active and reactive powers. The power references are set using a SCL (i.e., power dispatch) or a prespecified power profile based on local calculations (active reactive power support) [4]. The $q-$axis reference current is always responsible for the reactive power support at the PCC. For unity power factor operation, the $q-$axis reference current is set to zero. When a DG operates in non-interactive grid-connected mode, the $d-$axis reference current is generated so that it regulates a dc-link voltage or follows an MPPT algorithm. The main advantages of DG current control are that it ensures internal stability and enables current limiting, which acts as inherent overcurrent protection.

B. Islanding (microgrid) mode

To operate safely in islanded mode (as an autonomous microgrid), the microgrid should be able to keep the system frequency and voltage within the standard parameters. In non-interactive islanded control mode, one DG acts as a slack bus by regulating its PCC voltage and frequency through control of its output reactive and active powers, respectively. This DG must also have enough reserve capacity to ensure a balanced power supply. On the other hand, interactive islanded control mode implies the participation of all microgrid DGs in stabilizing the frequency and regulating the voltage by implementing virtual frequency-droop $(\omega-P)$ and voltage-droop $(v-Q)$ strategies. Droop

characteristics define the reference voltage and frequency of converter-based DGs so that they can share the system loading. The offset points of the droop characteristics can be controlled during the restoration process in order to retain the nominal frequency and voltage of the system. The restoration process is typically very slow, with the error signals being calculated every 5 sec to 10 sec by the dispatch centre [13].

2.1.2 Centralized ADN Control

Centralized ADN control is provided by a SCL whose main purpose is to optimize the operation, ensuring efficient, reliable, and robust performance. In grid-connected mode, this goal can be realized by setting the operating points of the DGs, loads, and network control devices to achieve a global objective, e.g., minimizing system losses, operating costs, and/or voltage deviations. Two-way communication between the SCL and the primary control level (PCL) of the DG is necessary and can be implemented via telephone lines, power line carriers, or a wireless medium [4]. Supervisory control is very slow, making decisions at every prespecified time interval, e.g., 10 min. Control algorithms that are utilized by the SCL should take into account any network security constraints as well as the DG and load power forecasts.

Microgrid mode entails two main supervisory control strategies: 1) single master operation (SMO) and multi-master operation (MMO). In SMO mode, one master DG acts as a slack bus (voltage reference), while the other DG units (slaves) operate in active/reactive power dispatch mode (PQ control) by regulating the DG output current. The master DG should have enough capacity to ensure a stable voltage and frequency. In MMO mode, a number of master DGs implement different $(\omega - P)$ and $(v - Q)$ droop characteristics in order to regulate the frequency and voltage within the microgrid. The remaining DGs (slaves) operate in PQ control mode [14]. To implement PQ control, the load powers are measured and sent to the SCL, which calculates and sends the reference PQ/current to each DG. The DG current control strategy locally regulates the measured output current from each DG so that it conforms to the reference PQ/current [15], [16]. The primary drawback of centralized control is the dependence on communication strategies, which adds to system costs and decreases reliability and system modularity.

2.1.3 Decentralized ADN Control

Decentralized control has been introduced as a means of overcoming the disadvantages of the centralized approach. In this type of control, whose name implies no communication, each DG is controlled only via its primary controller. In grid-connected mode, DGs can operate locally (without SCL) in order to generate a prespecified power profile based on the forecasted network load/generation. Alternatively, microgirds can also operate in a decentralized manner by implementing droop characteristics so that converter-based DGs emulate the behaviour of synchronous generators [17] (Figure 2.2). In contrast to the centralized approach, rather than maximizing revenue, the primary goal of the decentralized approach is to improve load sharing as well as microgrid robustness and reliability [4]. However, although decentralized control does not require communication, it can lead to voltage and frequency deviations, depending on the loading conditions.

To compensate for such deviations, a secondary control level is needed. This approach regulates the frequency and voltage of the microgrid so that any changes in operating conditions can be accommodated [14]. The frequency and voltage amplitudes are measured and compared to prespecified reference values. Based on the error between the reference and the measured values, the secondary control level sends restoration signals via communication links, instructing all DGs to shift their droop characteristics up or down [17].

2.2 Converter-Based DG Control

Since the late 1980s, the application of power electronic converters in power systems has rapidly attracted increased attention for the following reasons [18]:

1. Accelerated development of power electronics technology
2. Evolutionary advances in microelectronic technology, which facilitates the real-time development of complicated control and signal processing algorithms
3. The necessity for stability enhancements due to the continuous growth of the demand for energy
4. The application of power electronic converters in utility reconfigurations as a means of addressing power line congestion

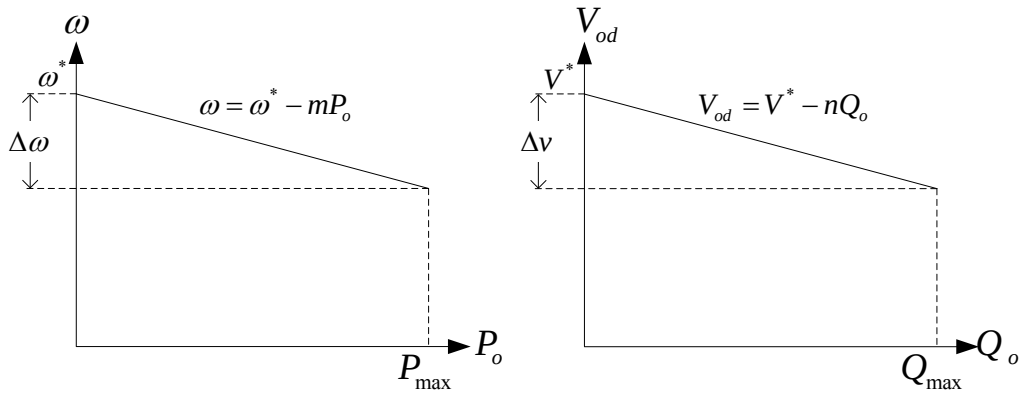

Figure 2.2: DG droop characteristics

5. The growing momentum toward further utilization of green energy, which is associated with new operational concepts, such as mircogrids, active networks, and smart grids

2.2.1 DG Current Control

For converter-based DGs, the control strategy usually involves two cascaded loops: inner and outer. The inner loop is a current control loop, which regulates the DG inverter current in the $d-q$ reference frame. The outer control loop, on the other hand, can have different control objectives depending on whether the ADN is operating in grid-connected or microgrid mode. Figure 2.3 shows a inverter-based DG that is controlled in current injection mode. A DG inverter model in the $d-q$ synchronous frame represents the dynamics of the interfacing LC filter [19], [20], i.e.,

$$L_f \frac{dI_d}{dt} = -R_f I_d + V_d - V_{od} + \omega L_f I_q \tag{2.1}$$

$$L_f \frac{dI_q}{dt} = -R_f I_q + V_q - V_{oq} - \omega L_f I_d \tag{2.2}$$

$$C_f \frac{dV_{od}}{dt} = I_d - I_{od} + \omega C_f V_{oq} \tag{2.3}$$

$$C_f \frac{dV_{oq}}{dt} = I_q - I_{oq} - \omega C_f V_{od} \tag{2.4}$$

$$\omega = \frac{d\theta}{dt} \tag{2.5}$$

where I_{dq} and I_{odq} represent the $d-q$ components of the inverter output current and DG current at the PCC, respectively, V_{dq} and V_{odq} are the $d-q$ components of the inverter terminal voltage and

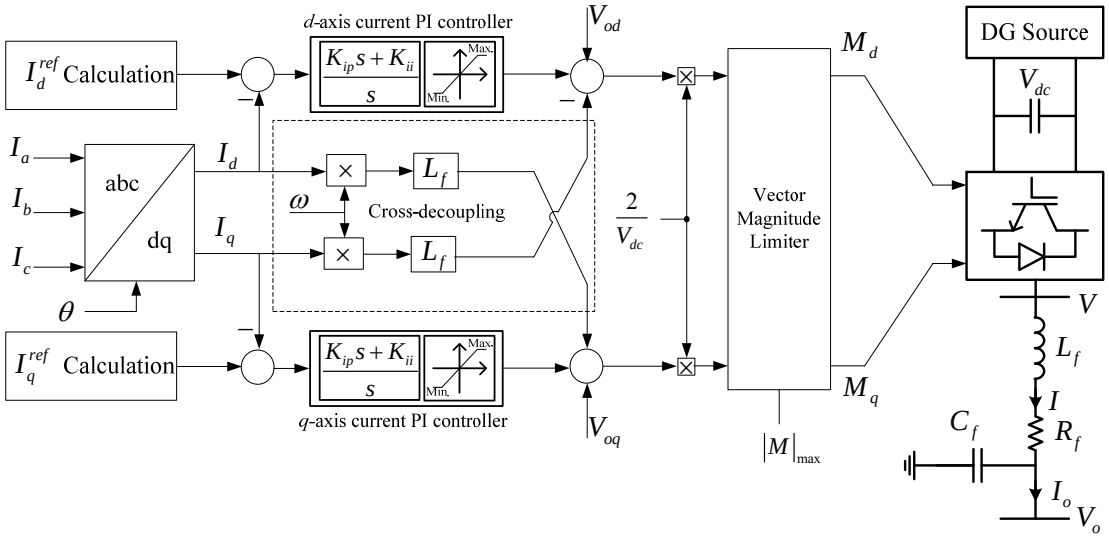

Figure 2.3: Power circuit and current control diagram for a converter-based DG

DG voltage at the PCC, respectively, R_f , L_f , and C_f are the resistance, inductance, and capacitance of the DG interfacing filter, respectively, and ω is the grid frequency.

The current equations, i.e., (2.1) and (2.2), are coupled through the $\omega L_f I_q$ and $-\omega L_f I_d$ terms. For independent control of both the I_d and I_q currents, the decoupled terms must be eliminated, which can be accomplished if new variables $V_d^{'}$ and $V_q^{'}$ are defined as follows [21]:

$$V_d^{'} = V_d - V_{od} + \omega L_f I_q \tag{2.6}$$

$$V_q^{'} = V_q - V_{oq} - \omega L_f I_d \tag{2.7}$$

Substituting from (2.6) and (2.7) into (2.1) and (2.2) yields

$$L_f \frac{dI_d}{dt} = -R_f I_d + V_d^{'} \tag{2.8}$$

$$L_f \frac{dI_q}{dt} = -R_f I_q + V_q^{'} \tag{2.9}$$

Eq. (2.8) and (2.9) represent decoupled first order models for I_d and I_q, respectively. The PI current controllers are designed based on the transfer functions expressed in (2.8) and (2.9). If the gains of the PI current controllers are selected as

$$\begin{cases} K_{ip} = \dfrac{L_f}{\tau_i} \\ K_{ii} = \dfrac{R_f}{\tau_i} \end{cases}, \tag{2.10}$$

then the equivalent closed loop transfer functions for the current loops can be given by

$$\frac{I_d(s)}{I_d^{ref}(s)} = \frac{I_q(s)}{I_q^{ref}(s)} = \frac{1}{\tau_i s + 1} \tag{2.11}$$

where τ_i is the time constant of the closed loop system. The vector magnitude of the reference current $\left(\sqrt{\left(i_d^{ref}\right)^2 + \left(i_q^{ref}\right)^2}\right)$ should be limited according to the maximum allowable current, typically 20 % greater than the rated current of the inverter [19], in order to provide overcurrent protection. The vector magnitude of the modulation index $\left(|M| = \sqrt{M_d^2 + M_q^2}\right)$ should also be limited to $|M|_{\max} = 1.0$ pu so that DG operates in a linear modulation region. Figure 2.3 shows the vector magnitude limiter, which implies a limit on the magnitude of $|M|$ without a change in the phase angle between M_d and M_q.

2.2.2 Droop-Based DG Control

As previously mentioned, the outer control loop of a converter-based DG is dependent on an ADN mode of operation. In decentralized microgrid operation, the DGs should emulate the behaviour of synchronous generators with respect to implementing droop characteristics. Assuming that the network impedance between the PCC and the grid is inductive, the power exchange between a DG and the grid is given by

$$P_o = \frac{V_o V_g}{X_{eq}} \sin(\delta) \tag{2.12}$$

$$Q_o = \frac{V_o V_g \cos(\delta) - V_g^2}{X_{eq}} \tag{2.13}$$

where X_{eq} is the network equivalent reactance, and δ is the phase angle between the DG output voltage V_o and the grid voltage V_g. These two equations reveal that the active power P_o is primarily dependent on δ, while the reactive power Q_o is reliant on the amplitude of the output voltage V_o.

Implementing the droop characteristics requires the calculation of the average active P_o and reactive Q_o powers at the PCC. In the synchronous $d-q$ frame, the instantaneous active (p_o) and reactive powers (q_o) at the PCC are given by

$$p_o = 1.5\left(V_{od}I_{od} + V_{oq}I_{oq}\right) \tag{2.14}$$

$$q_o = 1.5\left(V_{oq}I_{od} - V_{od}I_{oq}\right) \tag{2.15}$$

P_o and Q_o can then be calculated by filtering the instantaneous powers using a low-pass filter (LPF) with a cut-off frequency ω_p in order to enhance power quality injection:

$$P_o = \frac{\omega_p}{s+\omega_p}p_o, \qquad Q_o = \frac{\omega_p}{s+\omega_p}q_o \tag{2.16}$$

The droop characteristics define the reference frequency and voltage for the outer control loops:

$$\omega = \omega^* - mP_o \tag{2.17}$$

$$V_{od}^{ref} = V_{od}^* - nQ_o \tag{2.18}$$

where

$$m = \frac{\omega_{\max} - \omega_{\min}}{P_{\max}}, \qquad n = \frac{V_{od,\max} - V_{od,\min}}{Q_{\max}} \tag{2.19}$$

The output voltage is aligned with the $d-\text{axis}$; i.e., $V_{oq}^{ref} = 0$, such that V_{od} has full controllability of the reactive power Q_o. Figure 2.4(a) illustrates how droop characteristics are utilized to generate the reference voltage and frequency, which dynamically controls the angle. Both the reference voltage and the angle control the reactive and active power transfer from the DG to the grid, respectively. The angle is also used for calculating the $d-q$ components for both I_o and V_o. The dynamic model for the output voltage V_o in the $d-q$ frame is governed by (2.3) and (2.4). To provide a decoupled control for both V_{od} and V_{oq}, the following terms are defined:

$$I_d^{'} = I_d - I_{od} + \omega C_f V_{oq} \tag{2.20}$$

$$I_q^{'} = I_q - I_{oq} - \omega C_f V_{od} \tag{2.21}$$

Substituting from (2.20) and (2.21) in (2.3) and (2.4) yields

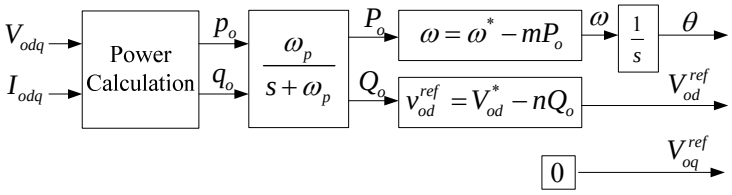

(a)

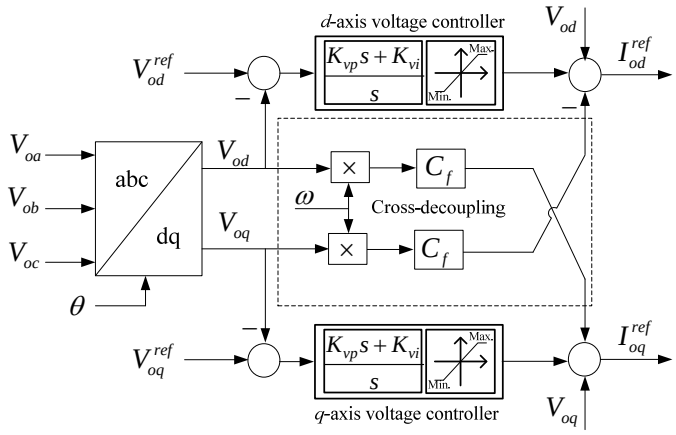

(b)

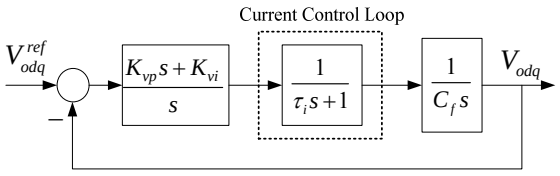

(c)

Figure 2.4: Control schemes for droop-based DGs: (a) droop control stage; (b) outer loops for voltage control; (c) inner loops for current control

$$C_f \frac{dV_{od}}{dt} = I_d^{'} \tag{2.22}$$

$$C_f \frac{dV_{oq}}{dt} = I_q^{'} \tag{2.23}$$

Eq. (2.22) and (2.23) define a decoupled model of the output voltage. Figure 2.4(b) shows outer loops for voltage controllers with the decoupled terms. When the decoupling terms are ignored, the closed loop system with both current and voltage controllers is as shown in Figure 2.4(c). This control loop consists of two cascaded loops: the current control loop and the voltage control loop. The inner control loop is normally designed to have a time constant (τ_i) between 3 ms and 5 ms [22]. However,

the outer voltage control loop should be designed to be three to five times slower than the inner current loop [23].

2.2.3 Constant PQ Control

For dispatchable DGs, such as fuel cells and biomass, the grid can interact with each DG by sending the reference active and reactive powers. For decoupled control of the active and reactive powers, a PLL should be used for aligning V_{od} with the output voltage V_{oa} so that $V_{oq} = 0$. Figure 2.5(a) shows a block diagram of the PLL, which utilizes a PI controller to force a zero value of V_{oq} by changing the $d-q$ frame angle θ. Figure 2.5(b) indicates the outer control loops for a PQ-based DG that are employed in order to regulate the active and reactive powers of the DG. Based on Eq. (2.14) and Eq. (2.15), the $d-\text{axis}$ current controls the active power, while the $q-\text{axis}$ current controls the reactive power. The PI controllers of the outer control loops are designed in the same way as the voltage controller discussed previously, and the design of the PI controller of the PLL is based on the small-signal analysis provided in [24].

The PLL shown in Figure 2.5(a) is called a synchronous frame PLL (SF-PLL), which can achieve fast and accurate phase and frequency detection without harmonics or imbalance if the utility voltage is ideal. If the bandwidth of the SF-PLL is reduced, it can act as a filter for high-order harmonics but at the cost of a decrease in response speed. However, reducing the bandwidth is not recommended in the case of an unbalanced grid voltage [24], because the phase error oscillates at double the supply frequency. In [25], an enhanced PLL (EPLL) was proposed for the extraction of the positive sequence voltage. The EPLL incorporates an adaptive notch filter that tunes its frequency based on the estimated supply frequency. The EPLL has two main advantages: 1) it is immune to frequency variations, and 2) its utilization of a band-pass filter (BPF) in order to obtain a 90-degree phase shift makes it less sensitive to harmonics.

The authors of [26] proposed a sinusoidal signal integrator PLL (SSI-PLL) for synchronizing a distorted grid voltage. The SSI-PI applies an adaptive band-pass filter (BPF) around the fundamental frequency in order to extract the positive sequence component of the grid voltage. The positive sequence voltage is then fed into the conventional SF-PLL in order to obtain the phase and frequency. In the study reported in [27], the researchers proposed a decomposition method that extracts the positive-, negative-, and zero-sequence components of three-phase signals. The proposed method estimates the magnitude, phase-angle, and frequency as a means of generating the sequence

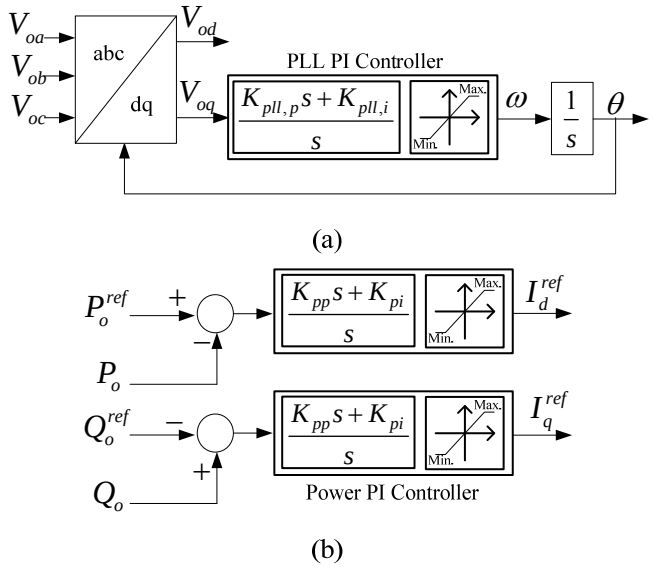

Figure 2.5: PQ-based DG control: (a) conventional PLL block diagram, (b) outer power control loops

components in the time domain. A conventional SF-PLL is then used for aligning v_{od} with the output voltage v_{oa}. The method introduced in [27] overcomes the drawbacks of a conventional SF-PLL and can provide the phase-angles of the sequence components. In [28], a new three-phase PLL is proposed for eliminating the redundancy that exists in the EPLL described in [25], which requires three-phase signals for the estimation of a single value for the frequency. The methods proposed in [27], [28] are similar, with only one discrepancy: in the version introduced in [28], the phase signals are estimated first followed by the calculation of the sequence components. In applications in which the sequence components are less important than the phase angles, the method presented in [28] provides a faster solution, but when the reverse is true, the method described in [27] is more efficient. In this thesis the SF-PLL is employed as a synchronization mean to avoid complicating the system nonlinearity, and thus simplifying the stability analysis.

2.3 DG Volt/VAR Control in ADNs

The intermittent nature of renewable power sources can significantly alter the system voltage profile and interfere with conventional OLTC control schemes. As well, the growing penetration of PEVs can add additional stress on voltage control devices due to the stochastic and concentrated power profile associated with PEVs. Such power profiles can lead to excessive tap operation, infeasible OLTC solutions (hunting), and/or limits imposed on the penetration of either PEVs or DGs. The literature mentions a number of control schemes for overcoming the negative effects of DGs on the

system voltage. In general, DG volt/var control (i.e., voltage regulation) can be classified as either centralized or distributed [29].

The centralized approach employs state estimation to dispatch DG reactive power, a technique that involves investment in communication links and remote terminal units. The authors of [30] used genetic algorithms (GA) to develop a multi-objective optimal voltage regulation algorithm as a means of minimizing voltage deviations and system losses. However, the DGs are not considered as voltage control devices. In [31], an optimal volt/var control technique was suggested in order to provide appropriate voltage regulation with minimal DG reactive support. However, neither coordination with other voltage control devices, such as OLTCs, nor minimization of DG active power curtailment is considered. In the study described in [32], to reduce the size and complexity of the optimization problem, the distribution network is divided into subnetworks using ε decomposition, but coordination with OLTCs is not taken into account. Other researchers [33] proposed two-stage optimal voltage regulation that coordinates the OLTC and static var compensators (SVCs). Their algorithm was designed to minimize system losses and tap operation in the case of radial distribution networks. To reduce the searching space for the second stage, the first stage obtains discrete settings for the OLTC and SVCs based on one-day-ahead power forecasting. However, DGs are assumed to operate at a unity power factor with no contribution to voltage regulation. In [34], the authors introduced an optimal coordination technique that minimizes tap operation through the utilization of the PV reactive power based on one-day-ahead forecasting for both loads and DG powers, but PV active power curtailment is not reflected in the case of limited DG reactive power support. Given the high degree of uncertainty inherent in renewable power generation, the conventional one-day-ahead optimization approach, which provides the basis for the scheduling of the operation of voltage and reactive power control devices, is severely prone to forecasting errors. In [35], optimal PV voltage regulation is proposed as a means of establishing optimal DG reactive power references. The reactive power references are then provided to DG primary-level controllers, which ensure decoupled active/reactive power control through feedback linearization. However, the proposed method fails to coordinate the DGs with other voltage control devices.

A distributed (intelligent) approach is considered to be an expert-based control or model-free approach, which coordinates a variety of voltage control devices with the goal of providing effective and non-optimal voltage regulation with fewer communication requirements. The authors of [36] developed an agent-based algorithm for DG reactive power dispatch that offers effective voltage

regulation with fewer communication requirements than with a centralized approach. However, coordination between the DG reactive power support and the OLTC was not taken into consideration. A further drawback is that no solution is provided when the DG is unable to regulate the voltage after the DG reactive power reaches its limit. Other research [37] involved a new voltage estimation methodology for estimating the minimum and maximum voltages for multi-feeder distribution systems, but the OLTC is assumed to be the only device responsible for voltage regulation, meaning that the daily stress on the OLTC is ignored. Relying only on OLTCs may also result in an infeasible solution when the difference between the maximum and minimum voltages in the system exceeds the standard regulation band. Coordinated control between the distributed energy storage systems (ESS) and the OLTC was suggested in [38]. When the network is lightly loaded, the suggested method relies on the minimization of the reverse power flow through the activation of the ESS charging controllers. The underlying assumption is that an ESS is attached to every DG, which is an uncommon practice. The coordinated control technique also fails to take into account cases in which the ESS is fully charged. In [11], a multi-agent-based voltage regulation algorithm was proposed as means of coordinating the DGs and other voltage control devices. The authors then extended their work to include diverse loads and high DG penetration [39]. In general, compared to a centralized approach, a distributed approach can reduce communication requirements, but this method is case specific because of the reliance on intelligent-based coordination, which must be reformulated from scratch when the system topology changes, and it is also unable to provide an optimal solution because it fails to include an optimization algorithm.

Vehicle-to-grid (V2G) technology can shift PEVs from a passive to an active load, which can then contribute to voltage regulation through reactive power support. Few studies report the utilization of PEV reactive power as grid voltage support [40]–[43]. The potential benefits of using PEVs as voltage control devices are discussed in [40]. In [41], a PEV coordinated charging algorithm was proposed for peak power shaving and minimization of losses, based on consideration of voltage regulation as a grid constraint. The authors of [43] introduced intelligent-based PEV voltage support that utilizes the reactive power available from all PEVs installed at the same feeder. However, this method fails to guarantee optimal voltage regulation and ignores the interaction between PEVs and DGs. In another study [42], local voltage compensation was based on the use of PEV reactive power for counteracting undervoltages caused by household loads and PEV charging.

This review of the literature reveals that considerable research has been conducted with respect to voltage regulation in ADNs, yet all of the previous work falls short in two respects:

1. No consideration has been given to a coordinated fuzzy logic control that can provide effective voltage regulation with minimal communication requirements, reduce stress on the OLTCs, maximize DG active power injection, and avoid the numerical instability and convergence problems associated with centralized voltage regulation schemes.
2. PEV reactive power support has yet to be incorporated into voltage regulation or to be coordinated with DG volt/var control. Such PEV reactive power support would take into account the self-objectives of the voltage control devices, such as the need for OLTC tap operation to be relaxed so as to extend equipment life, for PEV owners to maximize their SOC, and for DG owners to reduce their active power curtailment.

2.4 Stability of ADNs

As with large power systems, the stability of ADNs can be classified as small-signal, transient, or voltage. The study of each type of stability is related to different problems. In general, small-signal stability is associated with feedback controllers, small load changes, and system damping, while faults and islanding introduce most of the transient stability problems that arise in ADNs. Voltage stability problems, on the other hand, are linked to reactive power limits, load dynamics, and tap changers. One of the primary objectives of the research presented in this thesis was to improve the small-signal stability of ADNs.

Small-signal stability involves the evaluation of local ADN stability at a specific operating point based on a linearized mathematical model of the ADN around that operating point. The authors of [44] developed a small-signal model of a single inverter connected to a stiff grid. In [45], they reported an extension of their work [44] to include consideration of two inverters connected to an isolated microgrid. The primary drawbacks inherent in the studies presented in [44] and [45] are that both voltage and current control loops are neglected and that network dynamics are ignored. Although DG inner control loops are included in the detailed procedure for modelling ADNs for small-signal stability studies that was proposed in [46], the network dynamics are still omitted. In conventional power systems, network dynamics are typically neglected with respect to slow synchronous generator dynamics. However, this assumption is invalid for the ADN paradigm because most DGs are converter-based and consequently exhibit fast dynamics.

To address these problems, the authors of [21], [47], [48] developed complete small-signal ADN models that represent DG inner control loops as well as network dynamics. Their small signal model divides the network into subsystems, with each DG in the network considered a subsystem and modelled in its individual reference frame. One DG reference frame is arbitrarily selected to represent the common system reference frame to which all of the other DG models are mapped. The loads and network are treated as separate subsystems and modelled in the common reference frame. A complete state-space model of the entire system is then obtained by combining all of the subsystem models. The eigenvalues of the state-space system model are calculated at a specific operating point in order to assess system stability.

Impedance-based stability analysis can replace detailed eigenvalue stability analysis as a means of evaluating small-signal stability. The impedance stability criterion, first proposed by Middlebrook [49] for dc power electronic systems, divides the system under study into interconnected DG source and grid subsystems. In [50], the researchers used a multivariable $d-q$ domain model to extend the impedance stability concept to include three-phase systems. An additional extension of the impedance stability criterion for grid-connected DGs was proposed by Sun [51], [52]. When the stability of the DG control system is the primary factor of interest, it is preferable to assess stability using impedance stability criteria, an approach that offers the following benefits not available with detailed eigenvalue stability analysis [51]–[53]:

1. Remodeling the entire network becomes unnecessary, as does repeating the stability analysis when the network impedance changes or when additional DG or loads are connected.
2. Detailed information is no longer required with respect to network components, such as DG and load parameters, which are often unavailable [54].

To examine impedance stability, the system under study can be modelled using its Thévenin equivalent circuit, as shown in Figure 2.6. When the voltage division principle is applied to the circuit shown in Figure 2.6(a), the load voltage V_o can be given as

$$V_o(s) = V_s(s)\frac{1}{1+Z_s(s)/Z_l(s)} \tag{2.24}$$

where $Z_s(s)$ and $Z_l(s)$ are the source and load impedances in the s-domain. Eq. (2.24) is analogous to the equivalent transfer function of a feedback control system, in which $Z_s(s)/Z_l(s)$ represents the open loop transfer function. Assuming that the voltage source is stable when unloaded, stability is

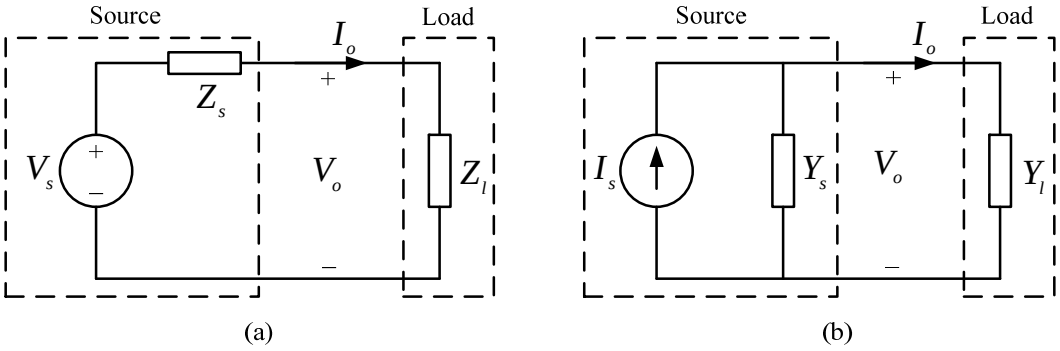

Figure 2.6: Small-signal representation of a DG load system: (a) voltage-controlled VSC; (b) current-controlled VSC

achieved when the $Z_s(s)/Z_l(s)$ ratio satisfies the Nyquist stability criterion over the entire frequency range. It is worth noting that the stability condition expressed in (2.24) is applicable for voltage-controlled voltage-source converters (VSCs) [51].

Alternatively, developing an impedance stability criterion for a current-controlled VSC requires the derivation of the Norton equivalent circuit of the system, as illustrated in Figure 2.6(b). Applying the current division principle to the circuit shown in Figure 2.6(b) results in the following load voltage V_o:

$$V_o(s) = \frac{I_s(s)}{Y_l(s)} \cdot \frac{1}{1 + Y_s(s)/Y_l(s)} \tag{2.25}$$

Similarly, (2.25) is analogous to a feedback control system, where $Y_s(s)/Y_l(s)$ is the open loop transfer function. Assuming that the current source is stable when unloaded, stability is achieved when the $Y_s(s)/Y_l(s)$ ratio satisfies the Nyquist stability criterion over the entire frequency range. From (2.24) and (2.25), it is apparent that opposite impedance stability conditions are associated with voltage-controlled and current-controlled VSCs. A current-controlled VSC is stable when it has high output impedance (ideally infinite), whereas a voltage-controlled VSC is stable when it has low output impedance (ideally zero).

2.5 Impedance Stability Assessment and Improvement

Addressing variations in grid impedance requires both the identification of the grid impedance (admittance) and the adaptation of the DG output impedance so that impedance stability can be assessed and improved.

2.5.1 Grid Impedance Estimation

Grid impedance identification can be classified as either noninvasive or invasive. A noninvasive approach utilizes existing grid transients, such as load variations, as a means of estimating grid impedance. In most cases, accurate estimations are not provided by DG voltage and current distortions because they fail to represent persistently exciting signals. An invasive approach, on the other hand, intentionally disturbs the grid and then performs acquisition and signal processing [55]–[63].

In [55], an online grid impedance identification method based on active and reactive power variations was proposed for single-phase converters, but active and reactive power variations are applicable only for this type of converter. Other researchers [56] employed controlled resonance of the LCL filter in order to excite the grid and to measure grid impedance. The authors of [57] introduced a grid impedance method for monitoring DG converters based on a recursive least-squares (LS) algorithm. The impedance identification algorithm proposed in [58] was also developed using a recursive LS method but with a forgetting factor that employed phasor measurements for bus voltages and currents. In [59], the authors proposed a small-signal impedance measurement algorithm that entailed injecting an unbalanced line-to-line current between two lines of the ac system. Another study [60] involved the introduction of an online grid impedance identification method that uses pulse perturbation with a 1.5 pu amplitude. Such a high amplitude may excite the nonlinear response of the system, thus affecting the accuracy of the linearized grid admittance. Although the methods proposed in [59], [60] can estimate multivariable grid admittance, they are also characterized by the following drawbacks: 1) they involve the application of a discrete Fourier transform (DFT) over the acquired measurements, which is time consuming and inappropriate for online applications; 2) they cannot provide the parametric admittance model that is more appropriate for online adaptive control design [64]. The method proposed in [12] also requires extra hardware for the estimation of grid admittance.

The authors of [61] presented a method for measuring multivariable DG impedance in the $d-q$ frame. Their technique involves connecting and disconnecting resistive and capacitive loads in order to identify inverter impedance, which is impractical for online grid impedance identification and requires additional equipment. Other researchers [62] proposed a wide bandwidth grid impedance identification method that provides an accurate measurement of the converter's output inductance, which is essential for modelling the nonlinear characteristics of powered iron cores. A minimally invasive grid impedance estimation technique based on an extended Kalman filter is described in

[63]. However, the proposed impedance model is ineffective when the power network includes capacitive components (e.g., capacitor banks used for reactive power compensation).

Previous identification algorithms have been based on the assumption that grid admittance can be represented by a combination of passive elements: R_g, L_g, and C_g, which form a passive model. Due to the growing penetration of inverter-based generation and loading, this assumption lacks sufficient accuracy. Grid admittance is dependent not just on passive elements but also on other DG and CPL impedance factors. Such types of impedance are nonlinear, time-varying, and not passive in nature, which means that grid admittance must be represented by an active model with a time-varying model structure.

Based on the above review of the literature, it is obvious that sufficient work has been conducted with respect to estimating passive grid impedance. However, a need still exists for an accurate grid admittance (impedance) identification tool that can estimate active grid impedance, i.e., impedance characterized by a time-varying and nonlinear structure. Such a tool should persistently excite the grid impedance dynamics as a means of guaranteeing convergence and should avoid over-parameterization. Such a grid admittance identification tool can be then used for assessing impedance stability and for designing adaptive DG controllers.

2.5.2 Adaptive DG Control

The literature includes reports related to the design of adaptive controllers for three-phase converters with the goal of managing unknown system parameters and ensuring robust performance. To modify the voltage control parameters when system conditions change, the authors of [65] proposed an adaptive voltage control algorithm based on a heuristic approach. However, the control topology utilized failed to incorporate the current dynamics and unsuitable for islanded operation. In [66], an adaptive current control scheme was presented for use with grid-connected DGs, taking into account the parametric uncertainties in DG filter parameters. The proposed scheme employs a model reference adaptive control with a resonant filter as a means of extending the bandwidth of the controller. Other work [67] involved the development of a nonlinear adaptive controller for three-phase pulse-width-modulation (PWM) rectifiers, which included consideration of load uncertainty. To address the resonance-frequency uncertainty associated with a DG LCL filter, a gain-scheduling control scheme for grid-connected DGs based on the estimation of grid inductance was introduced in [68]. In another study [69], with the goal of damping the resonance of LCL filters, the researchers

suggested a discrete-time model reference adaptive current controller for grid-connected DGs with LCL filters. However, gain-scheduling methods are simpler to analyze and do not introduce additional nonlinearity to the DG control system.

The work presented in [70] involved the development of an adaptive controller for active shunt filters, which included consideration of the uncertainties associated with grid voltage harmonics. The authors of [71] proposed an adaptive control scheme for tracking a time-varying frequency reference signal, thus reducing harmonic distortions in the current. In [72], an adaptive controller for VSCs that operates as a static synchronous compensator for power factor corrections was introduced. However, none of these studies has taken into account the effect of grid impedance on DG performance from an impedance stability perspective. The developers of the adaptive control algorithm for a grid-connected DG presented in [73] used a Routh-Hurwitz impedance stability analysis approach and included consideration of grid impedance. However, the analysis was based on neglecting the resistance of the grid, an assumption that results in insufficient accuracy because distribution networks are characterized by a high R/X ratio. The proposed algorithm is also unsuitable for islanded DG operation.

This literature review clearly demonstrates the lack of an adaptive DG control algorithm that can take into account the uncertainty associated with grid impedance as well as variations in the DG operating points, which are governed by supervisory-level control. To simplify the analysis, previously proposed adaptive DG control algorithms either rely on the assumption that grid impedance is an uncertain parameter, or neglect the resistance of the grid impedance. They are also marred by the following shortcomings: 1) they fail to include consideration of the adaptation of the outer control loops, 2) they are inappropriate for isolated microgrids, and 3) they cannot be optimally designed to increase system bandwidth and damping. Estimating grid impedance and deriving the DG output impedance based on its design specifications enable the DG output impedance to be reshaped according to impedance stability criteria so that system stability is maintained and the dynamic performance of the DG is enhanced.

2.6 Discussion

The information presented in this chapter has shown that DG supervisory and primary control levels have attracted increasing interest due to the intermittent nature of renewable DGs as well as the uncertainty associated with grid impedance. The critical review of the literature has provided details

of the research that has been conducted with the goals of improving supervisory and primary DG controllers and facilitating the implementation of ADNs. However, the work presented in existing reports has failed to provide adequate solutions for a number of supervisory and primary control challenges. First, no coordinated fuzzy-based control algorithms have been developed that offer effective DG volt/var control with minimal communication requirements. Second, surplus PEV reactive power must become an essential component of voltage regulation, an issue that has not yet been successfully resolved. Third, a new grid impedance identification algorithm is required for accurately estimating both passive and active grid impedance. The final element absent from research efforts to date is an examination of methods for adaptively reshaping DG output impedance for the mitigation of changes in grid impedance and DG operating points.

Chapter 3
Fuzzy Voltage Regulation with High Penetration of Renewable DGs

3.1 Introduction

In this chapter, the effect of the intermittent nature of renewable DGs on OLTC performance is investigated and discussed. The intermittent nature of renewable energy sources such as wind and solar energy can significantly change the system voltage profile and interact with the conventional control of OLTCs. This interference may lead to overvoltage, undervoltage, and abnormal wear of OLTCs due to excessive tap operation. A new fuzzy-based coordination scheme between the OLTC and DGs is proposed, offering the following benefits: 1) provision of proper voltage regulation without overvoltage or undervoltage; 2) relaxation of OLTC operation to extend its lifetime; and 3) avoidance of unnecessary DG active power curtailments.

The proposed voltage regulation scheme consists of three fuzzy-based control algorithms. The first control algorithm is proposed for the OLTC to mitigate the effect of DGs on the voltage profile. The second control algorithm is proposed to provide a DG reactive power support in order to relax OLTC tap operation. The third control algorithm aims to partially curtail DG active powers to restore a feasible solution from the OLTC perspective. As an additional advantage, the proposed fuzzy algorithms can reduce the communication burden compared with distributed and centralized techniques, because they rely only on the estimated system minimum and maximum voltages. Finally, the proposed approaches avoid the problems associated with centralized approaches (i.e., high computational burden, numerical instability, and convergence problems) because they do not need to run an optimization algorithm.

The remainder of this chapter is organized as follows. Section 3.2 illustrates the need for applying fuzzy logic in the voltage regulation of ADNs. The proposed fuzzy-based OLTC control is explained in Section 3.3, while the proposed fuzzy-based DG voltage support is discussed in Section 3.4. In Section 3.5, the proposed coordination scheme between all fuzzy controllers is clarified. Real-time simulations are provided in Section 3.6, and Section 3.7 concludes the chapter by summarizing its main contributions.

3.2 Application of Fuzzy Logic in Voltage Regulation

According to Lotfi Zadah [74], fuzzy logic can be viewed as a tool to emulate human mental capability. It can make rational decisions in an environment of imperfect information characterized by imprecision, uncertainty, and incompleteness. Voltage regulation in ADNs can be considered as an environment of imperfect information because the proposed fuzzy controllers utilize only the system maximum and minimum voltages to determine DG reactive power support and active power curtailment [75].

To prove the claim that the environment under study is of imperfect information and that there is thus a need to apply fuzzy logic, the following analysis is conducted. The sensitivity matrix S can be calculated from the Jacobian matrix of the Newton power flow as follows:

$$\begin{bmatrix} \Delta\theta \\ \Delta V \end{bmatrix} = \underbrace{\begin{bmatrix} S_{\theta P} & S_{\theta Q} \\ S_{VP} & S_{VQ} \end{bmatrix}}_{\mathrm{S}} \begin{bmatrix} \Delta P \\ \Delta Q \end{bmatrix} \tag{3.1}$$

To calculate DG reactive and active powers, which are needed to bring an initial voltage $V_{(b)}^{ini}$ at a certain bus b to a reference voltage $V_{(b)}^{ref}$, the following linear relation can be used, based on the sensitivity matrix S [32]

$$V_{(b)}^{ref} = V_{(b)}^{ini} + S_{VQ} x_Q + S_{VP} x_P \tag{3.2}$$

with,

$$\begin{cases} x_Q = Q_{\mathrm{o}(i)}^{ref} - Q_{\mathrm{o}(i)}^{ini} = \left[x_Q^{DG_1}, x_Q^{DG_2}, \cdots, x_Q^{DG_{Ng}} \right]^T \\ x_P = P_{\mathrm{o}(i)}^{ref} - P_{\mathrm{o}(i)}^{ini} = \left[x_P^{DG_1}, x_P^{DG_2}, \cdots, x_P^{DG_{Ng}} \right]^T \end{cases}, \; i \in \mathcal{I}_{DG} \tag{3.3}$$

where $\left(P_{\mathrm{o}(i)}^{ini}, Q_{\mathrm{o}(i)}^{ini}\right)$ and $\left(P_{\mathrm{o}(i)}^{ref}, Q_{\mathrm{o}(i)}^{ref}\right)$ are the DG active and reactive powers before and after voltage regulation at bus $i \in \mathcal{I}_{DG}$, respectively, $\mathcal{I}_{DG}$ is the set of buses with DG connections, N_g is the total number of DGs. Suppose that the system maximum voltage $V_{\max}^{sys}$ happens at bus b_1, while the system minimum voltage $V_{\min}^{sys}$ occurs at bus b_2. The main objective of the DG voltage support is determining the DG reactive and active powers that bring both $V_{\max}^{sys}$ and $V_{\min}^{sys}$ to the standard voltage limits V_{Upper} and V_{Lower}, i.e., 1.05 and 0.95 pu, respectively. Applying (3.2) at b_1 and b_2 leads to

$$\begin{cases} V_{(b_1)}^{ref} = V_{Upper} = V_{(b_1)}^{ini} + S_{VQ}x_Q + S_{VP}x_P \\ V_{(b_2)}^{ref} = V_{Lower} = V_{(b_2)}^{ini} + S_{VQ}x_Q + S_{VP}x_P \end{cases} \tag{3.4}$$

As can be seen from (3.4), we have two equations in $2 \times N_g$ unknowns, assuming that the system maximum and minimum voltages are estimated. This problem cannot be solved deterministically due to the lack of system information. Alternatively, such a problem can be solved using a centralized control scheme (which runs an optimization algorithm), an approach which requires access to all of the nodes' active and reactive powers and is susceptible to convergence problems. In terms of acquired information, the proposed fuzzy controllers require only the system minimum and maximum voltages to provide proper voltage regulation. For instance, the authors in [76] have proposed a fuzzy logic controller for the OLTC to have an adaptive nature that can deal with load uncertainty. However, the proposed fuzzy controllers do not consider the DG contribution in the voltage regulation problem, which adds to its uncertainty and complexity. The proposed fuzzy controllers also have the following advantages over conventional controllers such as hysteresis or PI controllers [75]:

1. They are multivariable controllers, as they accept two inputs (i.e., the system maximum and minimum voltages). Accepting multi-inputs increases the controller's degree of freedom and allows for emulating an adaptive reference. This feature is not available with conventional controllers, as they accept a single input, i.e., the error between a fixed reference and a regulated variable. For instance, a voltage violation may occur if the OLTC controller regulates the voltage at a fixed target point, because the voltage trend from the substation to the feeder terminal is not descending in the presence of DGs.
2. They can map nonlinear and heuristic relations between their inputs and output, a feature which cannot be provided by conventional controllers.

3.3 Fuzzy-based OLTC Control

The OLTC can vary the tap position $n_{(t)}$ from zero (no voltage compensation) to $\pm N_{\max}$ (maximum voltage compensation). Typically, the process of tap changing involves two time delays: 1) a controller time delay T_d, which is intentionally introduced to avoid tap changing during fast voltage transients, and 2) a mechanical time delay T_m due to the motor drive mechanism of the OLTC. The mechanical time delay T_m has a constant value, which usually varies from 3 to 10

seconds, while the controller time delay T_d commonly depends on the voltage error ΔV and controller dead band DB [77], [78]. Therefore,

$$T_d = \tau_o \frac{DB}{|\Delta V|} \tag{3.5}$$

where τ_o is a constant selected based on the tap changing mechanism.

Currently, most OLTCs employ line drop compensators (LDCs), as shown in Figure 3.1(a). The LDC measures the secondary voltage V_1 and the OLTC current I_{OLTC} to estimate the voltage drop at a target point V_k, and then regulates the estimated value of V_k (i.e., $\tilde{V}_k$) by adaptively adjusting V_1. However, the integration of DGs changes the voltage profile significantly and complicates the voltage regulation for the following two reasons:

1. The voltage trend is not descending from the substation to the feeder terminal, so a fixed target point is no longer valid.
2. The voltage estimation, based on local measurements, worsens in the presence of highly intermittent renewable sources, such as wind and PV.

A local voltage estimation with fixed target point operation can lead to improper decisions of OLTCs, which may result in overvoltage, undervoltage and/or excessive wear and tear of OLTCs. In this section, a fuzzy-based OLTC controller (FOC) is proposed to mitigate the drawbacks of conventional OLTC control. Communication links are required to provide proper estimation of $V_{\max}^{sys}$ and $V_{\min}^{sys}$. In this work, the state estimation algorithm in [37] is adapted to estimate $V_{\max}^{sys}$ and $V_{\min}^{sys}$.

Figure 3.1(b) demonstrates the block diagram of the proposed OLTC controller. The proposed fuzzy control adapts the voltage error ΔV such that $V_{\max}^{sys}$ and $V_{\min}^{sys}$ stay within the acceptable range; thus, it can guarantee a proper voltage regulation at all buses. The proposed FOC imitates the behavior of distribution network operators (DNOs), i.e., varying the OLTC tap setting in order to keep the system voltages within the standard limits. In other words, the proposed FOC emulates adaptive reference behaviour for OLTC control.

The membership functions (MFs) which are assigned for $V_{\max}^{sys}$ and $V_{\min}^{sys}$ are shown in Figure 3.2. Each input is assigned three MFs, namely, *V.Low*, *Low*, and *Normal* for $V_{\min}^{sys}$; and *Normal*, *High*, and *V.High* for $V_{\max}^{sys}$, where the letter *V* stands for very. The consequent part, i.e., ΔV, is assigned

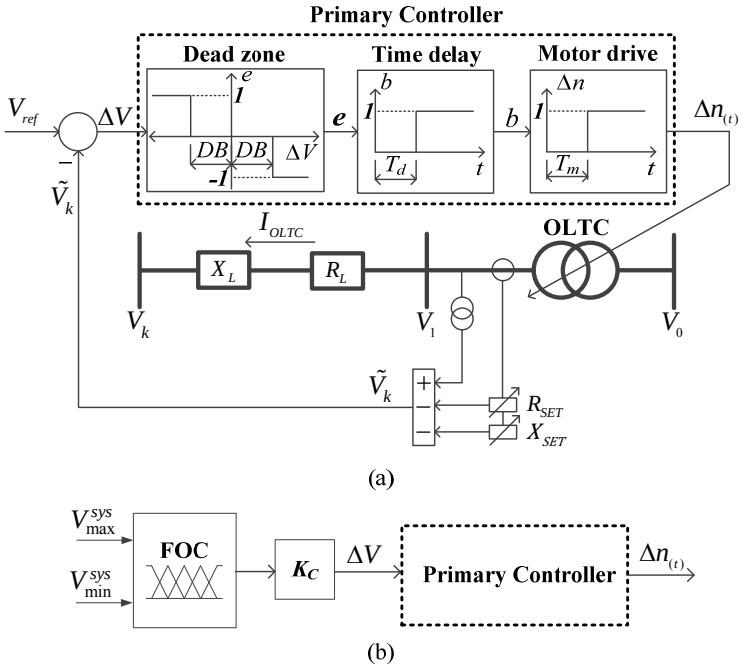

Figure 3.1: OLTC control: (a) conventional controller; (b) proposed FOC

five singleton MFs, namely, PL, P, Z, N, and NL, where the letters P, L, Z, and N stand for positive, low, zero, and negative, respectively. The output singleton values are 2, 1, 0, -1, and -2 for PL, P, Z, N, and NL, respectively. The scaling factor K_c of the FOC is tuned in order to normalize the fuzzy output with respect to the maximum expected deviation in ΔV. The rule base of the FOC is illustrated in Table 3.1, in which the MIN function is used for the fuzzy AND operator. The final crisp output of the controller is derived using the weighted average defuzzification method. The shaded rules in Table 3.1 represent the infeasible scenarios at which the OLTC fails to provide a proper action and thus should hold its tap position.

3.4 Fuzzy-based DG Voltage Support

Typically, OLTCs are considered the main devices responsible for voltage regulation in distribution systems. The application of the OLTC in ADNs introduces two challenges. The first challenge is the excessive wear and tear of OLTCs, especially when ADNs have high penetration of variable power sources. The second challenge is that OLTCs fail to provide proper tap settings when both $V_{\max}^{sys}$ and $V_{\min}^{sys}$ violate their specified limits simultaneously. On the other hand, DGs are incorporated in the voltage regulation by 1) reactive power support and 2) active power curtailment. In this section, two

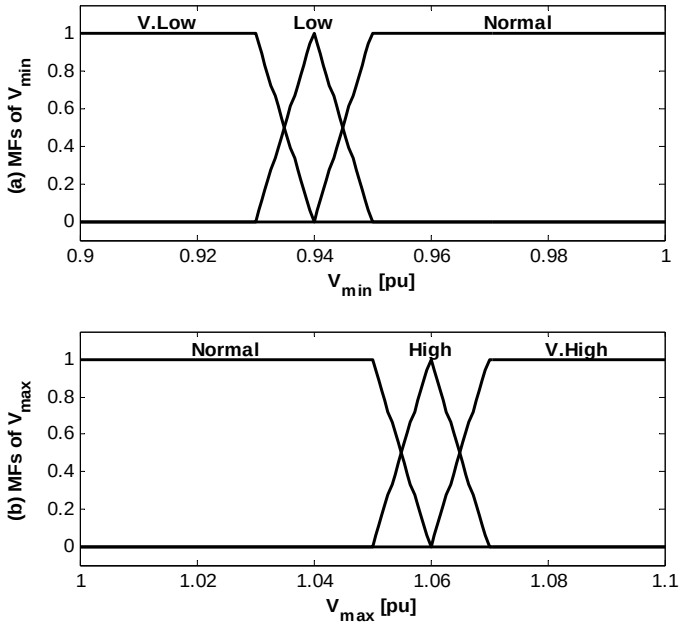

Figure 3.2: Input MFs of proposed FOC

Table 3.1: Rule Base of Proposed FOC

$V_{\min}^{sys}$	$V_{\max}^{sys}$		
	Normal	*High*	*V. High*
V. Low	PL	P	Z
Low	P	Z	N
Normal	Z	N	NL

fuzzy-based control algorithms are proposed for DG reactive power support and active power curtailment.

3.4.1 Fuzzy-based Reactive Power Support

Figure 3.3(a) shows a block diagram of the proposed fuzzy-based reactive power control (FQC), which is dedicated for all DGs connected to a certain feeder. The FQC receives the feeder minimum $V_{\min}^{f}$ and maximum $V_{\max}^{f}$ voltages to generate its output ΔV_F, which is then integrated to produce V_F. The main reason for the integration is to avoid resetting the DG reactive power after recovering a voltage violation, which can lead to unnecessary tap operation. The FQC algorithm utilizes the same rule base of the FOC, as given by Table 3.1.

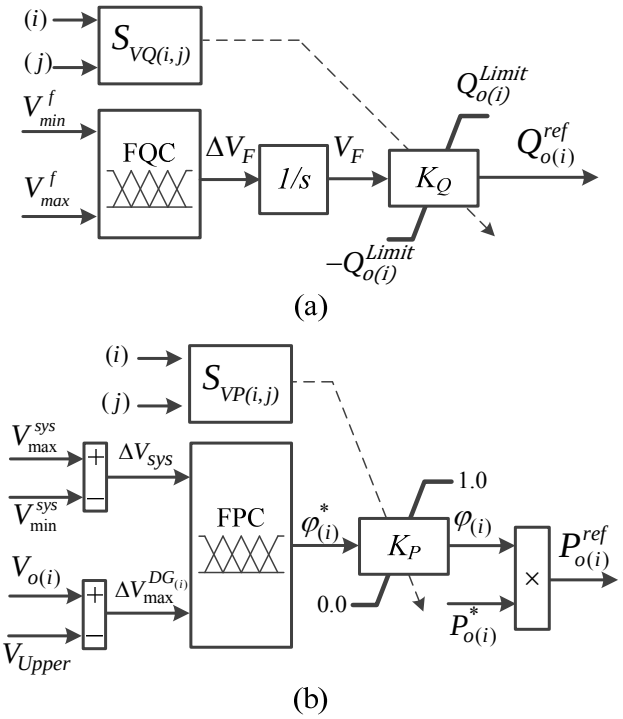

Figure 3.3: Proposed DG voltage support algorithms: (a) FQC; (b) FPC

To achieve proper reactive power sharing among all DGs at the same feeder, the reactive power reference $Q^{ref}_{o(i)}$ is determined by multiplying V_F by a voltage sensitivity factor K_Q proportional to $S_{VQ(\mathrm{i,j})}$, where i is the DG local bus and j is the bus at which $V^f_{\min}$ or $V^f_{\max}$ occurs. Voltage sensitivity analysis can determine the most effective nodes and amounts of DG reactive powers to support the grid voltage. A voltage sensitivity matrix S is calculated by solving load flow equations and determining the inverse of the Jacobian matrix [79]. A modified Newton-Raphson load flow is used to calculate the sensitivity factors, since it has the following merits: 1) it can avoid the convergence problems associated with the conventional Newton-Raphson load flow when the distribution network has low X/R ratio; and 2) it can be applied in meshed networks [81]. The variations of S are small for a wide range of operating conditions. Typically, the entries of S remain within 3% of their average values [80], and thus, they are assumed to be fixed.

The DG reactive power reference $Q^{ref}_{o(i)}$ is limited by the DG power factor and reactive power capability curves discussed in [82]. The reactive power capability curves set the DG reactive power limits based on the DG power rating and dc-link voltage. Hence, $Q^{\mathrm{Limit}}_{o(i)}$ can be calculated as

$$Q_{o(i)}^{\text{Limit}} = \min\left(Q_{o(i)}^{pf}, Q_{o(i)}^{S}, Q_{o(i)}^{V}\right) \tag{3.6}$$

where

$$\begin{cases} Q_{o(i)}^{pf} = P_{o(i)} \tan\left(\cos^{-1}\left(pf_{(i)}\right)\right) \\ Q_{o(i)}^{S} = \sqrt{S_{o(i)}^2 - P_{o(i)}^2} \\ Q_{o(i)}^{V} = \sqrt{\left(\dfrac{V_{\text{c}(i)}^{\max} V_{o(i)}}{X_{(i)}}\right)^2 - P_{o(i)}^2} - \dfrac{V_{o(i)}^2}{X_{(i)}} \quad , \; i \in \mathcal{I}_{DG} \end{cases} \tag{3.7}$$

Here, $P_{o(i)}$ is the DG active power at bus $i \in \mathcal{I}_{DG}$, $S_{o(i)}$ is the DG rating, $pf_{(i)}$ is the DG power factor, $V_{o(i)}$ is the PCC voltage, $V_{\text{c}(i)}^{\max}$ is the maximum DG converter voltage that depends on the dc-link voltage, and $X_{(i)}$ represents the total reactance of the DG interfacing transformer and filter.

Once $V_{\min}^{f}$ or $V_{\max}^{f}$ violates the standard limits, the FQC is energized to increase or decrease ΔV_F in order to mitigate the voltage violation problem. For instance, if a certain feeder suffers from undervoltage, the FQC generates a positive ΔV_F. Based on their voltage sensitivities, all DGs inject reactive power in order to boost $V_{\min}^{f}$ to the standard lower limit, and vice-versa. The proposed FQC has the following advantages:

1. Relieving the excessive OLTC operation,
2. Reducing the possibility of having infeasible solutions because it shrinks the gap between $V_{\min}^{sys}$ and $V_{\max}^{sys}$, and
3. Increasing the reactive power capability that is required to mitigate the problem of voltage violation, where all DGs at a certain feeder participate in solving the problem, irrespective of the locations at which the voltage violations occur.

It is worth noting that the proposed fuzzy algorithms are designed to deal with radial networks, which are the common topology of distribution networks. The proposed FOC is generic and can be applied in both radial and meshed networks because it is system configuration-independent (i.e., at any state(s), a change in the substation voltage magnitude has the same effect on all downstream buses regardless of their topology). Nonetheless, the proposed FQC needs to be modified for meshed distribution networks because the DG influence is not limited to its feeder but can propagate to other

feeders. Thus, the typical inputs of the proposed FQC, i.e., $V_{\min}^{f}$ and $V_{\max}^{sys}$, should be replaced by $V_{\min}^{sys}$ and $V_{\max}^{sys}$ in meshed networks.

3.4.2 Fuzzy-based Active Power Curtailment

When the difference between $V_{\max}^{sys}$ and $V_{\min}^{sys}$ is greater than the difference between the standard upper and lower voltages, i.e., V_{Upper} and V_{Lower}, the solution becomes infeasible from an OLTC perspective. The problem worsens when the FQC is unable to provide the required reactive power due to the DG's reactive power limitations. In such a case, the OLTC fluctuates severely and the solution can only be provided by two means: DG active power curtailment to decrease $V_{\max}^{sys}$, or load-shedding to increase $V_{\min}^{sys}$. Due to the utility commitments, the second option is not proposed. Instead, a fuzzy-based DG active power curtailment (FPC) is proposed to provide shared DG active power curtailments based on DG participation in the overvoltage problem. As shown in Figure 3.3(b), the proposed FPC has two inputs and one output. The FPC inputs are ΔV_{sys} and $\Delta V_{\max}^{DG_{(i)}}$, defined as

$$\begin{aligned} \Delta V_{sys} &= V_{\max}^{sys} - V_{\min}^{sys} \\ \Delta V_{\max}^{DG_{(i)}} &= V_{o(i)} - V_{Upper} \end{aligned} \tag{3.8}$$

The FPC generates $\varphi_{(i)}^{*}$, which is then rescaled based on the sensitivity factor K_P to obtain the DG active power curtailment factor $\varphi_{(i)}$. The sensitivity factor K_P is inversely proportional to $S_{VP(i,j)}$, where i is the DG local bus and j is the bus at which $V_{\max}^{sys}$ occurs. Therefore, all DGs share the active power curtailments based on their contributions to the overvoltage problem. Also, the second input, i.e., $\Delta V_{\max}^{DG_{(i)}}$, is used as a measure of the DG contribution to ΔV_{sys}. For a certain DG, a large $\Delta V_{\max}^{DG_{(i)}}$ implies that such a DG has a relatively greater impact on ΔV_{sys}, and thus its power curtailment should be greater, and vice-versa. Similarly, when ΔV_{sys} is large, the power curtailment should increase, and vice-versa. It is worth noting that the active power curtailment is applied only to DGs whose feeder maximum voltage is equal to $V_{\max}^{sys}$.

As shown in Figure 3.4, both ΔV_{sys} and $\Delta V_{\max}^{DG_{(i)}}$ have three triangle MFs, namely, normal *(N)*, high *(H)*, and very high *(VH)*. The output $\varphi_{(i)}^{*}$ is assigned five singleton values,

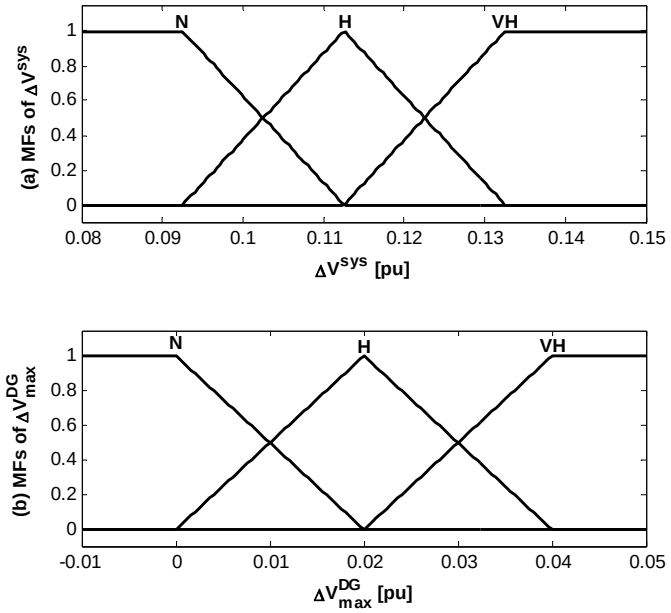

Figure 3.4: Input MFs of proposed FPC

Table 3.2: Rule Base of Proposed FPC

$\Delta V_{\max}^{DG_{(i)}}$	ΔV^{sys}		
	N	H	VH
N	U	H	M
H	H	M	L
VH	M	L	Z

namely, unity *(U)*, high *(H)*, medium *(M)*, low *(L)*, and zero *(Z)*. The singleton values of the output MFs are 1, 0.75, 0.5, 0.25, and 0 for *(U)*, *(H)*, *(M)*, *(L)*, and *(Z)*, respectively. The FPC rule base is summarized in Table 3.2. For a certain DG, $\varphi_{(i)}$ is multiplied by its active power reference $P_{o(i)}^{*}$ to determine the updated reference $P_{o(i)}^{ref}$. According to Table 3.2, *IF* a DG has normal $\Delta V_{\max}^{DG_{(i)}}$ *AND* ΔV_{sys}, *THEN* $\varphi_{(i)}^{*}$ is unity, which implies no active power curtailment.

3.4.3 Application of ESS in Voltage Regulation

Distributed ESS are typically interfaced through power electronic converters, similar to DGs [83], [84]. The interfacing converters have the two main tasks of regulating both active and reactive powers. Hence, ESS can be incorporated in the reactive-power voltage support by applying the

proposed FQC. Unlike renewable DG units, ESS are dispatchable power sources and have bi-directional power flow (i.e., charging and discharging). During discharging, ESS act as DGs, and hence, the proposed FPC can be applied without any modification. During the charging, ESS are treated as loads. Thus, ESS participate in the undervoltage rather than the overvoltage. In such a case, the proposed FPC needs to be slightly modified to fit the ESS. During the charging mode of operation, the second input of the proposed FPC, i.e., $\Delta V_{\max}^{DG_{(i)}}$, should be replaced by $\Delta V_{\min}^{ESS_{(i)}}$, which is defined as

$$\Delta V_{\min}^{ESS_{(i)}} = V_{Lower} - V_{o(i)}, \quad i \in \mathcal{I}_{ESS} \tag{3.9}$$

where $V_{o(i)}$ is the PCC voltage of an ESS unit connected at bus $i \in \mathcal{I}_{ESS}$. It is worth nothing that the proposed FPC has the same inference system (i.e., rule base and input-output MFs) during ESS charging and discharging.

3.5 Coordination between the Fuzzy algorithms

Coordination between the proposed fuzzy controllers is essential to provide efficient operation of the OLTC, with minimum DG active power curtailment. The flowchart of the proposed coordination scheme that manages the three fuzzy controllers is illustrated in Figure 3.5. First, the maximum and minimum voltages for each feeder and for the entire distribution system are estimated. When a voltage violation occurs, the FQC is activated to mitigate the voltage violation by injecting or absorbing reactive power under pre-specified reactive power limits. After activating either FQC or FPC, a time delay Δt_{conv} is introduced to ensure that all DG converters reach the desired reactive or active power references. This time delay depends on the settling times of the converter primary controllers, which can vary from 50 to 100 ms [18]. In this study, Δt_{conv} is assumed to be 200 ms, while the total update time of the proposed coordination algorithm ΔT is 5 min. If the proposed FQC cannot alleviate the voltage violation, the OLTC activates the FOC when a feasible solution exists. To guarantee a feasible solution using the FOC, the following condition has to be satisfied:

$$\Delta V_{sys} \le \Delta V_{Limit} - \Delta a \tag{3.10}$$

where Δa is the step change of the transformer turns ratio, and ΔV_{Limit} is the difference between V_{Upper} and V_{Lower}. To allow a margin of change up or down for the tap operation, Δa is considered in (3.10). If Condition (3.10) is not satisfied (indicating an infeasible scenario), the FPC will be

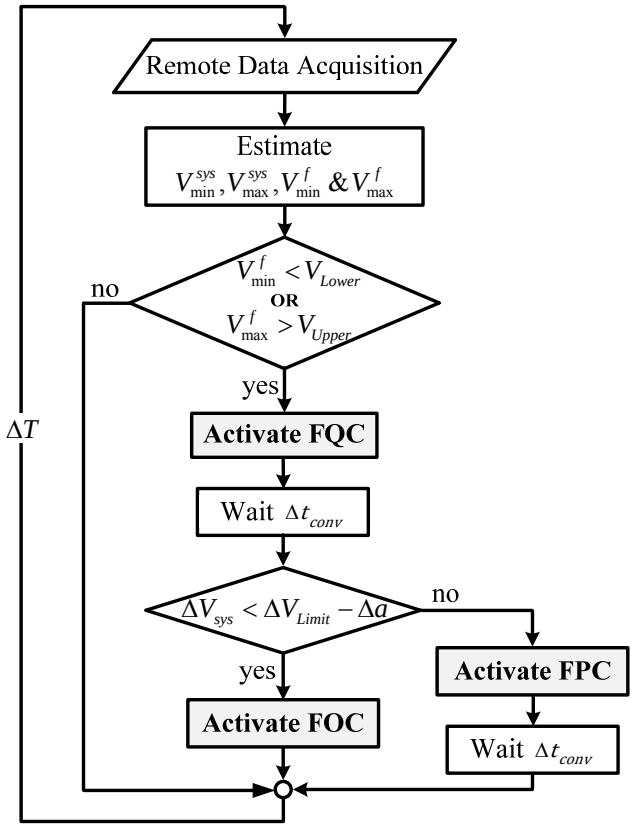

Figure 3.5: Proposed coordination scheme between fuzzy algorithms

energized in order to decrease $V_{\max}^{sys}$, which results in decreasing ΔV_{sys} to restore a feasible solution for the FOC.

3.6 Real-Time Simulations

Real-time simulators (RTS) provide parallel computations which allow for the distribution of large and complex models over several processors to perform powerful computations with high accuracy and low-cost real-time execution. In addition, RTS increase system reliability by increasing the test coverage, including faulty and abnormal operating conditions, and integrating other control and protection systems. The RTS typically has four applications:

1. Rapid control prototyping (RCP), where the plant controller is implemented using the RTS and then connects to a physical plant, as shown in Figure 3.6(a). The main advantages of implementing the plant controller using the RTS are flexibility as well as ease of implementation and debugging.

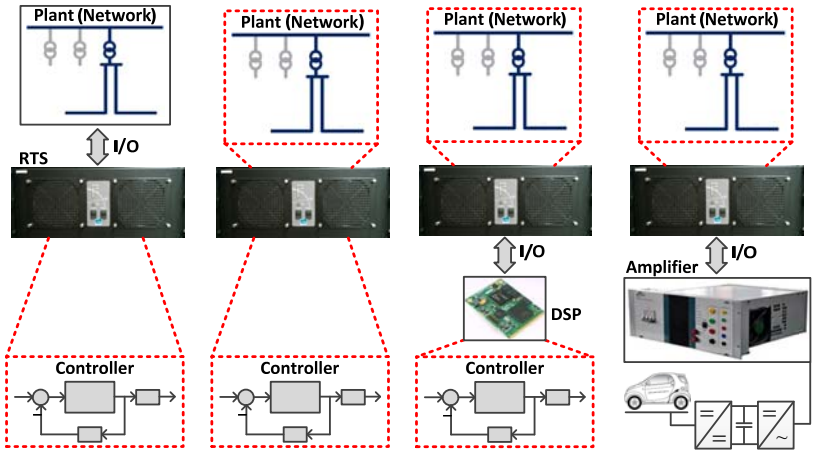

(a) RCP (b) SiL (c) HiL (d) PHiL

Figure 3.6: RTS applications

2. Software-in-the-loop (SiL): Utilizing the powerful commutation of the RTS, both the plant and its controller can be simulated in real time using the same RTS, as illustrated in Figure 3.6(b). The SiL is ideal for accelerated simulations because both the plant and controller run on the same simulator, and thus, synchronization with the outside world in not necessary.
3. Hardware-in-the-loop (HiL): In this approach, the physical controller is connected to a virtual plant modeled using the RTS (see Figure 3.6(c)). This physical controller can be implemented using another RTS, creating a RCP, or any digital-signal-processor (DSP) based controller. The controller and virtual plant are connected in real time through I/O channels.
4. Power hardware-in-the-loop (PHiL): The key component of the PHiL is a power amplifier, which is characterized by high bandwidth and rating. In this application, the RTS is used to model a virtual network similar to the HiL application. The main difference between the PHiL and HiL is that part of the network is physically realized outside the RTS and interfaced to the RTS through the power amplifier, as shown in Figure 3.6(d). This part of the network can be a DG converter, a PEV charger, etc.

The proposed fuzzy algorithms are modeled by the OPAL RTS using the SimPowerSystems blockset and ARTEMiS plug-in. The real-time simulations are considered to prove the applicability of the fuzzy algorithms as prototype controllers, which is an important stage before practical implementations. The RTS is used to perform two main functions: RCP and HiL applications. The

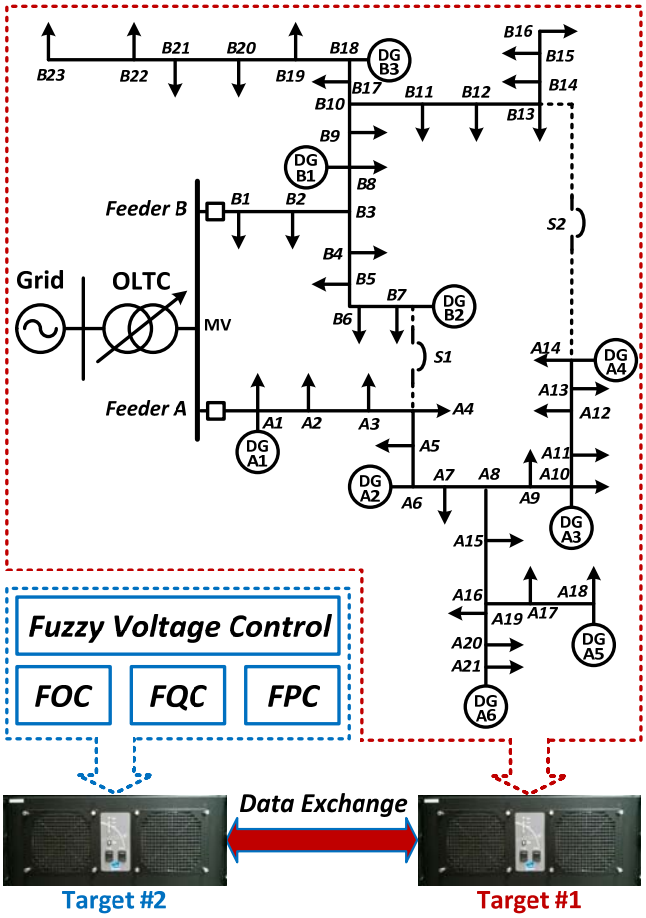

Figure 3.7: Distribution test network, implemented using HiL setup

RCP realization is used to implement the proposed fuzzy controllers to mimic actual voltage regulators. Compared with actual voltage regulators, RCP controllers are more flexible, easier to debug, and faster to implement. The HiL application is needed to test the proposed controllers, implemented as RCP controllers, when attached to a visual distribution network modeled in real time. The PHiL application is not implemented due to hardware limitations and the time frame of the point under study. The PHIL application is typically used to test the dynamic behavior of devices during fast disturbances [85]. However, the time frame of our study is 24 hours, as this is best suited to HiL applications.

Figure 3.7 demonstrates the test network realized by the HiL application. The RTS lab consists of two processors (targets), each with 12-3.33 GHz dedicated cores to perform parallel computations. To

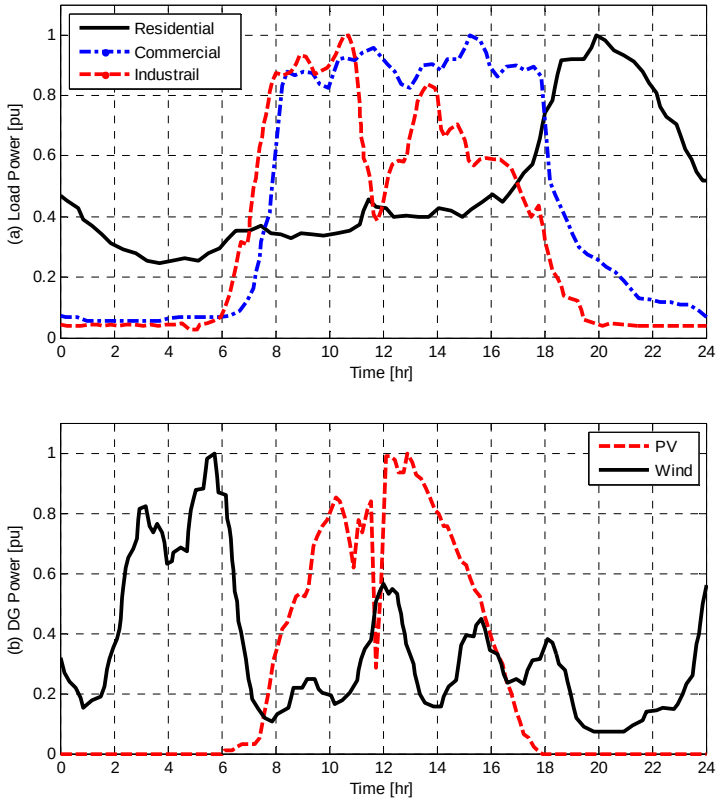

Figure 3.8: Typical daily load and generation power profiles

achieve the HiL realization, the network and DG models are implemented in Target #1. Each DG model is assigned to one core similar to the network model to achieve parallel computation. The fuzzy controllers are implemented in Target # 2. Each DG voltage support, i.e., FQC and FPC, is assigned to one core similar to the FOC. Both targets exchange data in real time to test the fuzzy controllers as prototyping controllers. The sampling time used to realize the HiL application is 100 µs. For more details about OPAL-RT and HiL applications, readers can refer to [86]–[90].

The distribution test system consists of two feeders at 20 kV, namely, Feeder A and B, with 46 buses [91]. Feeder A has residential load profiles and 6 wind-based DGs, while Feeder B has different load types (residential, commercial, and industrial) and 3 PV-based DGs. The typical daily load and generation power profiles are shown in Figure 3.8 [91]–[93]. All DGs are assumed to be inverter-based, and thus have the capability of supplying reactive power. The total connected load at Feeder A is equal to 14.31 MW/4.13 Mvar, while Feeder B has a total connected load equal to 13.88 MW/5.22 Mvar. A detailed description of the system data can be found in Appendix A. To test the robustness of the proposed algorithms, four scenarios are considered. These are detailed in the following sections.

3.6.1 Comparison with Conventional Control

In this case study, real-time simulations are performed to compare the following control schemes:

1. The conventional OLTC control (based on LDC),
2. The proposed FOC without incorporating FQC and FPC,
3. The proposed coordination algorithm without considering a power factor limitation,
4. The proposed coordination algorithm with 0.95 power factor limitation.

Figure 3.9 illustrates the response of the OLTC under the control schemes discussed above. Although, the conventional OLTC control results in no excessive tap operation (6 taps/day), the system voltages violate their specified limits at different operating conditions. The overvoltage problem is introduced during the peak wind power generation at Feeder A. Contradictorily, the undervoltage happens during the peak loading condition at Feeder B. To tackle this voltage violation, the proposed FOC should be introduced. Without incorporating the proposed FQC and FPC, the proposed FOC can recover the system voltages, but with relatively excessive tap operation (15 taps/day). To avoid such excessive tap operation, the DG fuzzy voltage support needs to be integrated in the voltage regulation. The proposed coordination, with no restriction on the power factor limits, results in a relaxed tap operation (3 taps/day). To detect the robustness of the proposed fuzzy algorithms, the DG power factor is limited to be within a 0.95 lag or lead. Although the DG power factors are limited, the proposed coordination scheme can solve the voltage violation problem with a reasonable number of taps (8 taps/day). Obviously, the number of taps has increased because the reactive power capability is limited. Also, the OLTC responds with extra two taps during peak loading (approximately between 19:00 and 20:00) because the PV-based DGs at Feeder B have no active power, so their reactive power contribution is null. It is worth noting that the FPC is not activated in this scenario because the solution is feasible, i.e., Condition (3.10) is satisfied in all operating points.

3.6.2 Active Power Curtailment Scenario

In this case study, the effectiveness of the proposed FPC is examined. This algorithm is only activated when Condition (3.10) is not satisfied, indicating a DG reactive power deficiency in supporting the system voltage. To stimulate this scenario, DG A2, DG A4 and DG A5 are replaced with PV-based

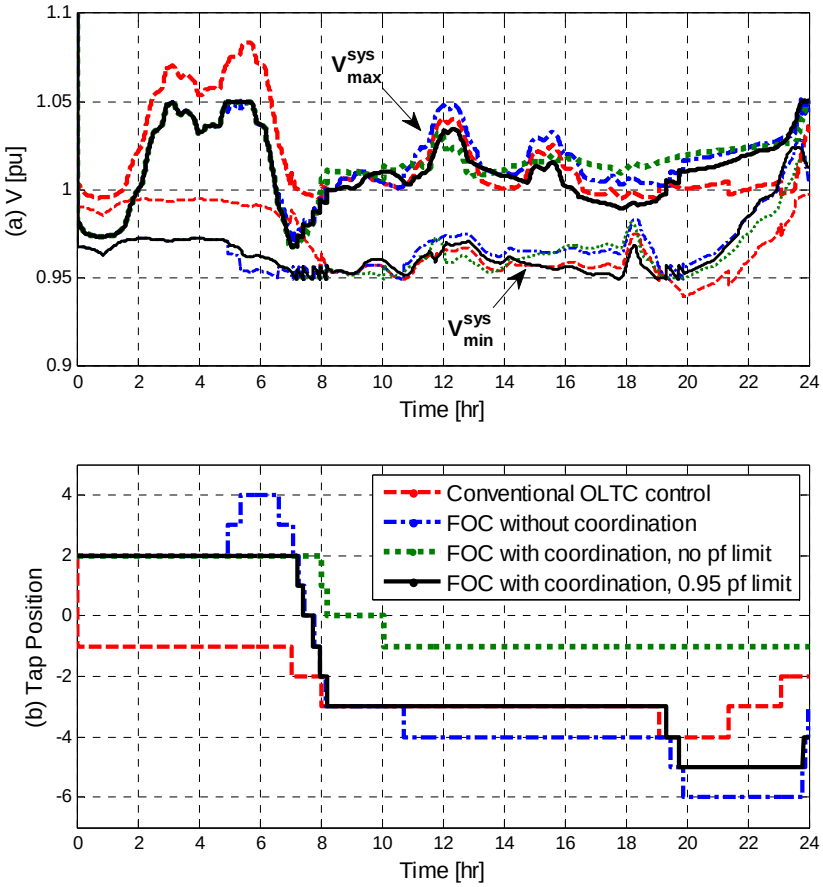

Figure 3.9: OLTC responses under different control schemes: (a) V^{sys}_{min} and V^{sys}_{max} ; (b) tap position

DGs, while DG B2 is replaced with a wind-based DG. All other system parameters remain as in the previous case study. Figure 3.10 shows comparative studies between the conventional OLTC control and proposed fuzzy algorithms at different incorporations, during an infeasible scenario. The conventional OLTC control results in voltage deviations, where V^{sys}_{min} and V^{sys}_{max} occur at the same time interval, i.e., approximately from 9:00 to 16:00. Thus, the OLTC feasibility condition is violated. Activating the FOC without incorporating the FQC and FPC results in a hunting problem. In such a case, the FOC cannot solve the voltage violation problem alone and must be either coordinated with the FQC and FPC, or deactivated. To detect the effectiveness of the proposed fuzzy algorithms, the DG power factors are limited to be within a 0.95 lag or lead. Integrating the FQC with the FOC can solve the problem partially; however, the OLTC still has a fluctuating response, approximately from 12:00 to 13:00, due to the power factor limit implemented

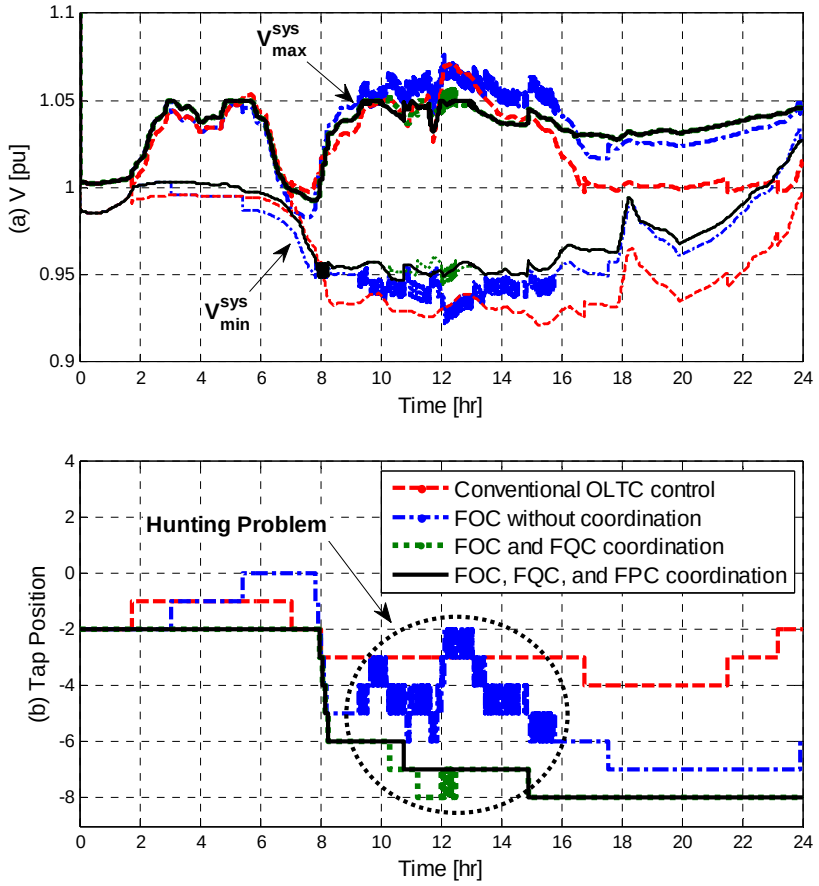

Figure 3.10: OLTC responses during an infeasible scenario: (a) $V^{sys}_{\min}$ and $V^{sys}_{\max}$; (b) tap position

in the FQC. Finally, the overall coordination scheme is examined. The proposed FPC provides a solution for the infeasible case with a reasonable number of taps (6 taps/day).

It is worth noting that the active power curtailment is activated only for the DGs at Feeder A, as they are the reason behind the system overvoltage. Figure 3.11 shows the active power curtailment factors for all DGs at Feeder A. The FPC curtails active powers based on the DG participation in the overvoltage problem. The largest active power curtailments are made for DGA5 and DGA6 because they have the largest ratings and are connected at the feeder terminals. Hence, their contribution to the system overvoltage is significant. The results indicate that the largest active power curtailments for DGA5 and DGA6 are 18% and 13%, respectively, and occur around 12:00. At that time, DGA5 has higher active power injection than DGA6, so the FPC curtails more power from DGA5 than from DGA6.These results show the effectiveness of the proposed FPC in identifying the curtailment factors based on the contribution of each DG in the overvoltage problem.

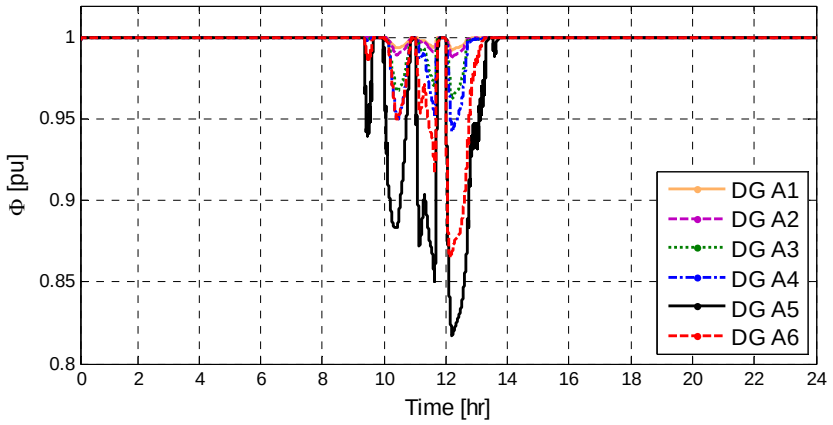

Figure 3.11: Active power curtailment factors for all DGs at Feeder A

3.6.3 Meshed Network Scenario

In order to investigate the effectiveness of the proposed algorithms in meshed networks, the tie switches (**S1** and **S2**) are closed to form a meshed distribution network (see Figure 3.7). The DG power profiles are similar to Case B. Figure 3.12 illustrates a comparative study between the conventional and proposed control algorithms at different incorporations for the meshed network scenario. Again, the conventional OLTC control fails to provide a proper voltage regulation in ADNs. Without coordination, FOC cannot solve the problem and fluctuates approximately between 12:00 and 13:00, since Condition (3.10) is not satisfied. Alternatively, the proposed coordination algorithm solves the hunting problem with relaxed tap operation (5 taps/day). It is worth noting that the FOC and FQC can solve the problem without the need of active power curtailment as compared with the radial configuration. From the above results, it can be concluded that the proposed coordination scheme can deal with meshed networks if, as discussed previously, the FQC considers the system minimum and maximum voltages instead of the feeder minimum and maximum voltages.

3.6.4 ESS Charging Scenario

ESS can play a considerable role in the undervoltage problem during the charging. In such a case, the proposed FPC acts as a smart charger to avoid the undervoltage problem. To examine the robustness of the proposed algorithms during ESS charging, two 0.5 MW ESS are added at B16 and B23, respectively. All other system parameters remain as in Case B. The conventional control results in a

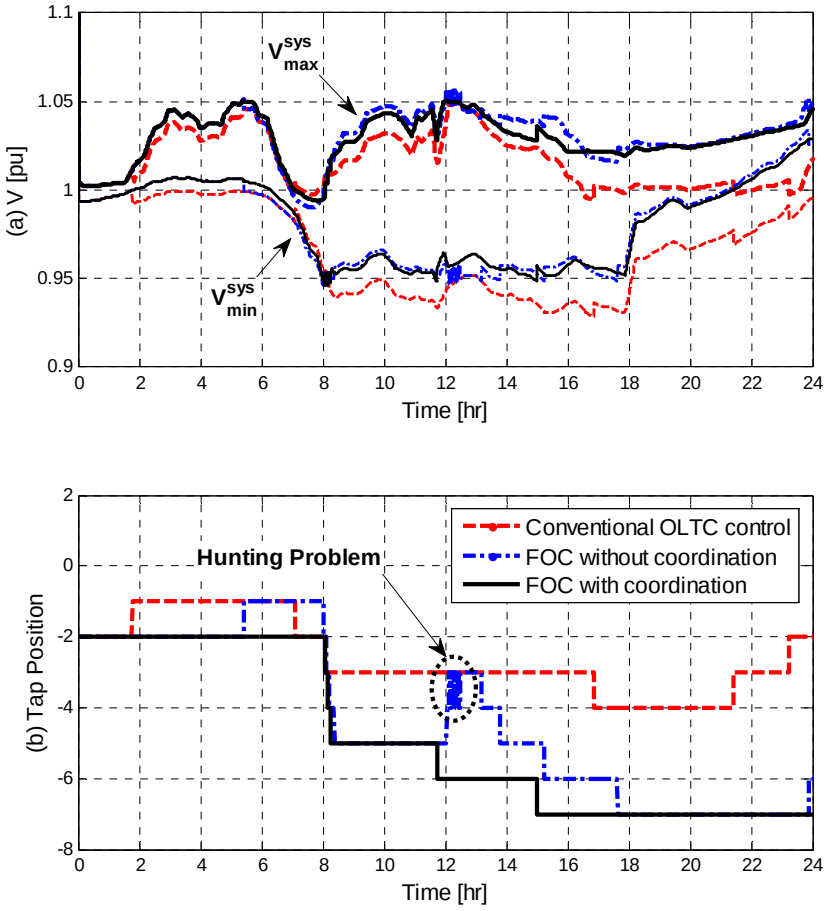

Figure 3.12: OLTC responses in a meshed network: (a) $V_{\min}^{sys}$ and $V_{\max}^{sys}$; (b) tap position

voltage violation, in which the difference between $V_{\min}^{sys}$ and $V_{\max}^{sys}$ violates the OLTC feasibility constraint, as shown in Figure 3.13. The application of the proposed FOC without introducing the FQC and FPC results in a hunting problem. Merging all fuzzy controllers, using the proposed coordination scheme, leads to proper voltage regulation with relaxed tap operation. Figure 3.14 demonstrates the active power curtailment factors for the DGs at Feeder A, which suffers from overvoltage, and ESS at Feeder B, which suffers from undervoltage. The ESS at B23 has more active power curtailment compared with the ESS at B16, as $V_{\min}^{sys}$ occurs at B23. These results demonstrate the effectiveness of the proposed FPC in dealing with the ESS charging.

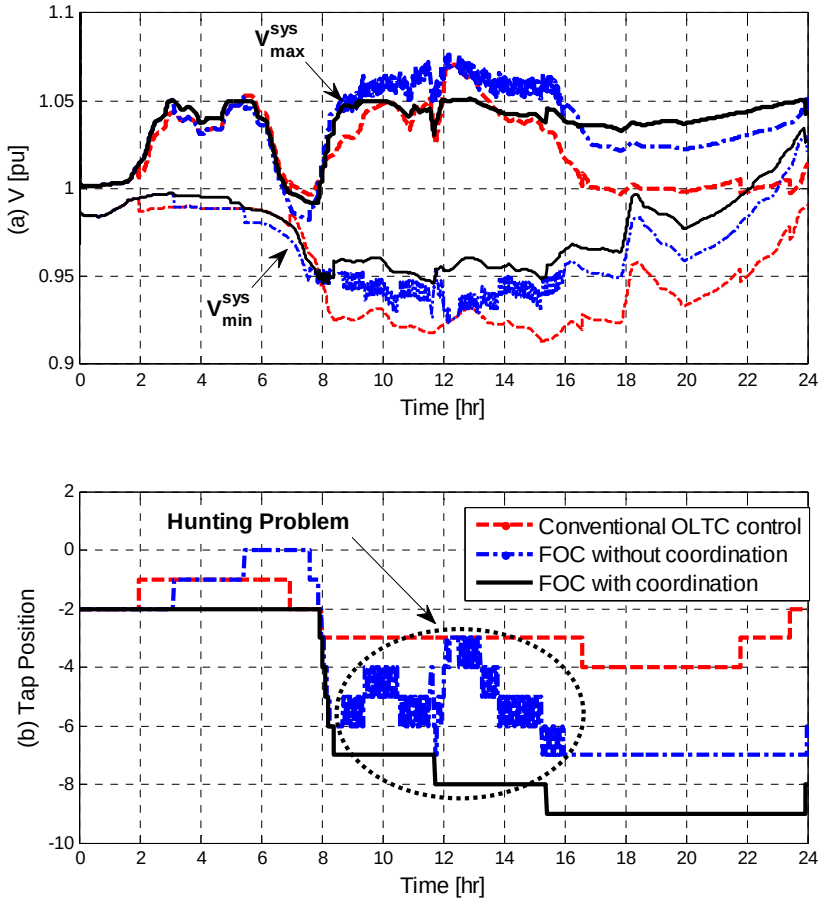

Figure 3.13: OLTC responses during ESS charging: (a) $V^{sys}_{\min}$ and $V^{sys}_{\max}$; (b) tap position

3.7 Discussion

The conventional control of OLTCs relies on a fixed target point and does not take into account the DG effect, which complicates the voltage regulation due to reverse power flow and voltage estimation difficulties. In this chapter, three fuzzy-based voltage regulators were proposed to tackle voltage violation problems associated with high DG penetration. As we saw, DGs started to fix the voltage violation by controlling their reactive powers. Then, if the problem persisted due to the reactive power limits of DGs, the proposed fuzzy OLTC controller began to solve the problem, if the solution was feasible. In cases of infeasible scenarios, DGs curtailed their active powers to restore a feasible solution from the OLTC perspective.The proposed fuzzy algorithms can also deal with ESS. All DGs and ESS share their reactive- and active-power supports according to their relative contributions to the problem. Incorporating the proposed fuzzy algorithms using the proposed coordination scheme

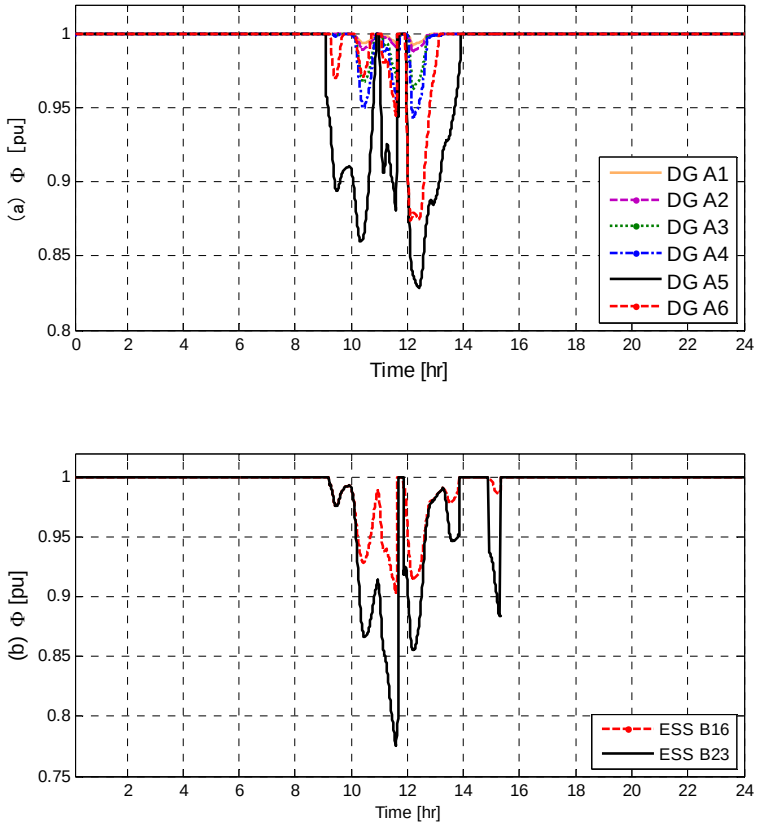

Figure 3.14: Active power curtailment factors during ESS charging: (a) for DGs at Feeder A; (b) for ESS at Feeder B

can provide proper voltage regulation with relaxed tap operation and proportionate DG and ESS active power curtailments.

Furthermore, the proposed fuzzy algorithms can be integrated as ancillary services within DSP-based controllers of voltage control devices. However, communication links are still necessary to estimate maximum and minimum voltages. Compared with distributed and centralized voltage regulation approaches, the proposed algorithms have a relatively low communication cost because they rely only on the estimated minimum and maximum voltages. The proposed coordination also mitigates the numerical instability and convergence problems associated with centralized approaches that run the power flow algorithms in each time step. This is especially relevant in cases involving a low X/R ratio. Real-time simulations were performed to show the effectiveness and robustness of the proposed algorithms using OPAL-RTS. The results demonstrated the success of the proposed fuzzy algorithms under various operating conditions and system configurations.

Chapter 4
Optimal Voltage Regulation with High Penetration of PEVs

4.1 Introduction

If CO2 emissions are the primary cause of global warming, then focusing on the sectors that contribute the most to these emissions (i.e., electricity generation and transportation) might be the best way to handle the problem. Thus, a shift towards renewable energy sources with electrification of vehicles could provide a cleaner future [2], [3]. However, the growing penetration of both DGs and PEVs can significantly change the system voltage profile and interfere with the conventional control schemes of OLTCs. This is because both technologies have stochastic and concentrated power profiles, along with occasional chronological profiles. Such power profiles can lead to excessive tap operation when hunting from the OLTC perspective and/or limited action on the penetration of either PEVs or DGs.

In Chapter 3, the proposed fuzzy logic controllers were not designed to tolerate the effect of the PEV charging on the system voltage profile. In addressing this shortfall, the main contribution of this chapter is to propose an optimal voltage regulation algorithm that maximizes PEV power demand and satisfies grid voltage requirements with relaxed tap operation and minimum DG active power curtailment. The voltage regulation is formulated as non-linear programming with three-stage optimization algorithms. The first stage aims to maximize the energy delivered to PEVs, the second stage aims to maximize the DG active power extraction, and the third stage minimizes the system voltage deviation using PEV and DG reactive power surplus. The third stage implicitly relaxes the OLTC operation by considering PEV and DG voltage support as the first line of defense when a voltage violation occurs. Consequently, the OLTC utilizes the output of the third stage to set its tap position, using a proposed OLTC centralized controller which employs the system maximum and minimum voltages. As a means of testing the robustness and effectiveness of the proposed optimal coordinated voltage regulation, its performance is validated using OPAL-RT in an HiL application.

The rest of this chapter is organized as follows. In Section 4.2, the contribution of both PEVs and DGs in the voltage violation problem is clarified. The proposed centralized OLTC controller is explained in Section 4.3. In Section 4.4, the proposed optimal coordinated voltage regulation

algorithm is illustrated. Section 4.5 demonstrates the real time simulations, and a discussion and conclusion are presented in Sections 4.6 and 4.7, respectively.

4.2 PEV Contribution to the Voltage Violation

Traditional distribution networks are passive, which means that power is transferred from the substation to the customers in a uni-directional power flow. However, in the presence of DGs and PEVs, the distribution network is subjected to a bi-directional power flow. Figure 4.1 represents a simplified multi-feeder distribution network connected to a substation through an OLTC. The test network has PV-based DG and PEV parking lots, which are connected at different feeder terminals. The per-unit voltage deviation for both DG and PEV buses can be approximated as

$$\begin{aligned} \Delta V_{PV} &\approx \left(P_{PV} - P_{L_1}\right) R_{f_1} + \left(Q_{PV} - Q_{L_1}\right) X_{f_1} \\ \Delta V_{EV} &\approx -\left(P_{EV} + P_{L_2}\right) R_{f_2} - \left(Q_{EV} + Q_{L_2}\right) X_{f_2} \end{aligned} \tag{4.1}$$

where P_{PV}, P_{EV} and P_L are DG, PEV, and load active powers, respectively, and Q_{PV}, Q_{EV}, and Q_L are DG, PEV, and load reactive powers, respectively.

Furthermore, Eq. (4.1) shows that the two worst-case scenarios are overvoltage, when the DG generates its maximum power during lightly loaded networks, and undervoltage, during the peak load demand and low DG output. The integration of DGs changes the voltage profile significantly and complicates the voltage regulation. This is due to two reasons: 1) the voltage trend not descending from the substation to the feeder terminal, thereby invalidating the target point (reference); and 2) the voltage estimation, based on local measurements, becoming inaccurate in the presence of highly intermittent renewable sources, such as wind. The integration of PEVs augments the stochastic nature of the problem, and thus the voltage estimation based on local measurements becomes inferior [94].

Poor voltage estimation can lead to improper decisions of OLTCs, which may result in overvoltage, undervoltage, and excessive wear and tear of OLTCs. The problem worsens if both overvoltage and undervoltage take place simultaneously. This scenario occurs when feeders suffer from overvoltage due to high DG penetration, while others suffer from undervoltage during high loading, such as PEV charging. In this instance, the OLTC will have two contradicting solutions. Decreasing the transformer's secondary voltage relaxes the overvoltage problem but complicates the undervoltage problem, and vice-versa. Figure 4.2 shows two power profiles for typical PV-based DG

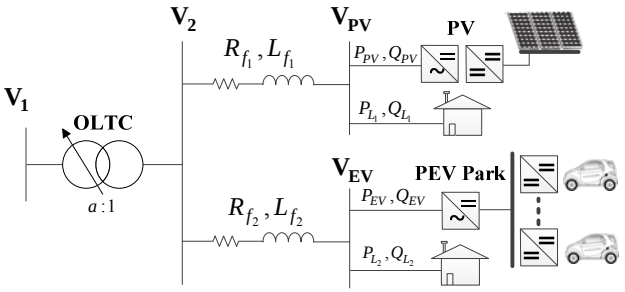

Figure 4.1: Simplified distribution network with DG and PEVs

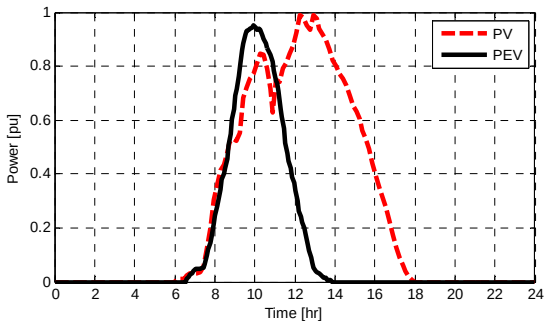

Figure 4.2: DG and PEV power profiles

and PEV uncontrolled[1] charging loads, which are based on practical data provided by the Toronto Parking Authority (TPA). Due to the nature of PEV and PV power profiles, there is a high probability for both overvoltage and undervoltage to occur at the same time. In order to avoid such a problem, the OLTC should rely on the system maximum and minimum voltages. A centralized-based control of the OLTC can provide a partial solution to the problem, but with excessive tap operation.

To relax the tap operation, both PEV and DG should be incorporated in the voltage regulation. Two possible solutions can be provided using DGs: DG reactive power support, and DG active power curtailment. Although it is not preferable to curtail active power (as it represents an economic waste), DG reactive power support is limited by its power rating, and thus may not be able to fully address the problem. Alternatively, the PEV can be employed to provide its surplus reactive power to increase the reactive power capability for voltage regulation, reducing the need for the DG active power curtailment [94]. In this chapter, a novel optimal coordinated voltage regulation scheme is proposed to coordinate PEV, DG, and OLTC to achieve optimal voltage regulation and satisfy the self-objectives of each voltage control device.

[1] In uncontrolled charging schemes, the PEVs start charging as soon as they are plugged in.

4.3 OLTC Centralized Control

In this section, both modeling and conventional control of OLTC are explained, along with the proposed OLTC centralized controller. As shown in Figure 4.3, the OLTC is represented by a π-circuit model [77], [95]. The taps are assumed to be at the primary side (high voltage). Subsequently, the OLTC secondary voltage and current can be calculated as

$$\begin{bmatrix} V_{(1,t)} \\ I_{(1,t)} \end{bmatrix} = \begin{bmatrix} \frac{1}{a} & -\frac{a}{Y_T} \\ 0 & -a \end{bmatrix} \begin{bmatrix} V_{(0,t)} \\ I'_{(0,t)} \end{bmatrix} \tag{4.2}$$

where Y_T is the transformer series admittance, a is the turns ratio, and t denotes the time instant. To take the physical buses in to account, (4.2) can be rewritten as

$$\begin{bmatrix} I_{(0,t)} \\ I_{(1,t)} \end{bmatrix} = \underbrace{\begin{bmatrix} g_F + jb_\mu + \frac{Y_T}{a^2} & -\frac{Y_T}{a} \\ -\frac{Y_T}{a} & Y_T \end{bmatrix}}_{Y_{OLTC}} \begin{bmatrix} V_{(0,t)} \\ V_{(1,t)} \end{bmatrix} \tag{4.3}$$

where Y_{OLTC} is the OLTC Y-bus admittance matrix, which represents the OLTC admittance in the power flow equations. The taps are changed linearly; hence a can be given as

$$a = a_o + n_{(t)}\Delta a \tag{4.4}$$

where a_o is the nominal turns ratio that usually equals 1.0 pu, Δa is the step change of a_o, and $n_{(t)}$ is the tap position. This position can be given by

$$n_{(t)} = n_{(t-1)} + \Delta n_{(t)} \tag{4.5}$$

where $n_{(t-1)}$ is the previous tap position, and $\Delta n_{(t)}$ is the integer change of $n_{(t-1)}$. The OLTC can vary the tap position from zero (no voltage compensation) to $\pm N_{max}$ (maximum voltage compensation).

Figure 4.4 shows both conventional and proposed OLTC controllers. In order for the OLTC to deal with multiple feeders with high penetration of both DGs and PEVs, the conventional OLTC control should be modified to emulate an adaptive reference by considering the system minimum and maximum voltages. The system minimum and maximum voltages, i.e., V_{min}^{sys} and V_{max}^{sys}, can either be acquired from the proposed central control unit, which is discussed in Section 4.4, or estimated using the state estimation algorithm proposed in [37]. The proposed centralized OLTC controller (COC) can emulate an adaptive reference because it changes the voltage error ΔV based on V_{min}^{sys} and V_{max}^{sys}

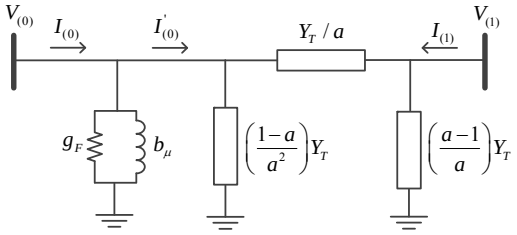

Figure 4.3: Equivalent π-circuit model of OLTC

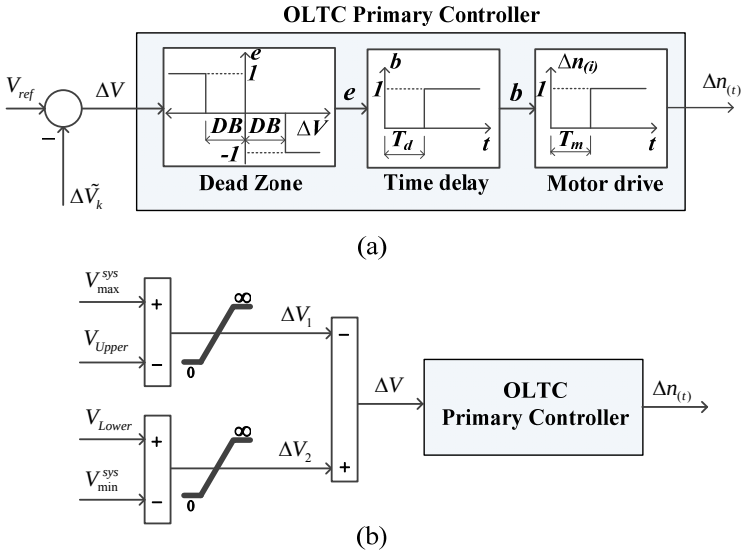

Figure 4.4: The OLTC control: (a) conventional local controller, (b) proposed centralized OLTC controller (COC)

rather than a fixed reference V_{ref} . It is worth mentioning that the proposed COC represents the classical logic implementation of the proposed FOC because both rely on the same inputs and perform the same logic control.

The proposed COC is straightforward to fit real-time applications. It controls the tap position, such that $V_{\min}^{sys}$ and $V_{\max}^{sys}$ are within the standard limits V_{Upper} and V_{Lower} (i.e., 1.05 and 0.95 pu), respectively. For instance, if the network suffers from overvoltage only, the ΔV will be negative. In this way, the primary controller increases the tap position to decrease the transformer secondary voltage, and vice-versa. During normal conditions, $V_{\min}^{sys}$ and $V_{\max}^{sys}$ are within the standard limits, hence both ΔV_1 and ΔV_2 are saturated at zero, resulting in no change in the tap position.

When the system simultaneously suffers from both overvoltage and undervoltage, the COC should be deactivated to avoid hunting [11]. To guarantee a feasible solution using the proposed COC, Condition (3.10) should to be satisfied. Although Condition (3.10) can prevent the hunting problem, the system may still suffer from voltage violation due to the inability of the OLTC to restore the system voltages during a synchronized overvoltage and undervoltage. The hunting problem can be fully addressed by relaxing the OLTC operation via the proposed optimal PEV and DG reactive power support, which is explained in Section 4.4.

4.4 Proposed Optimal Coordinated Voltage Regulation

This section explains the proposed optimal coordinated scheme that provides an optimal voltage regulation while satisfying the self-objectives of each voltage control device. Both PEV and DG units need to be incorporated in the voltage regulation by reactive power support to relax the OLTC. Figure 4.5 shows the proposed coordination scheme, integrating the V2GQ. The main advantage of the proposed V2GQ technology over typical V2G technology is that the former does not discharge the PEV batteries. Thus, the V2GQ sustains its battery life-time, which is one of the highest customer priorities. Unlike the V2G, the V2GQ cannot be used in power management applications, such as peak power shaving, because the PEV batteries are not reversing power to the grid. In this study, customer satisfaction is considered the highest priority, and so the typical V2G is avoided.

The proposed optimal voltage regulation is formulated as three-stage nonlinear programming, in which Stage (I) maximizes the energy delivered to PEV, Stage (II) maximizes the DG extracted power, and Stage (III) minimizes the system voltage deviation. The proposed COC utilizes the output of Stage (III) to meet the standard voltage limits with relaxed tap operation. The choice between maximizing the renewable energy or fleet energy might be a country-specific viewpoint. In other words, Stage (II) may be exchanged with Stage (I), if maximizing the DG energy has the highest priority. The details of each stage are given below.

4.4.1 Problem Formulation of Stage (I)

The main objective of Stage (I) is maximizing the energy delivered to PEV owners, i.e.,

$$\max_{\gamma} \sum_{i \in \mathcal{I}_{PEV}} \sum_{ch_{(i)} \in \mathcal{CH}_{(i)}} E_{D(ch_{(i)},t)} \qquad \forall t \tag{4.6}$$

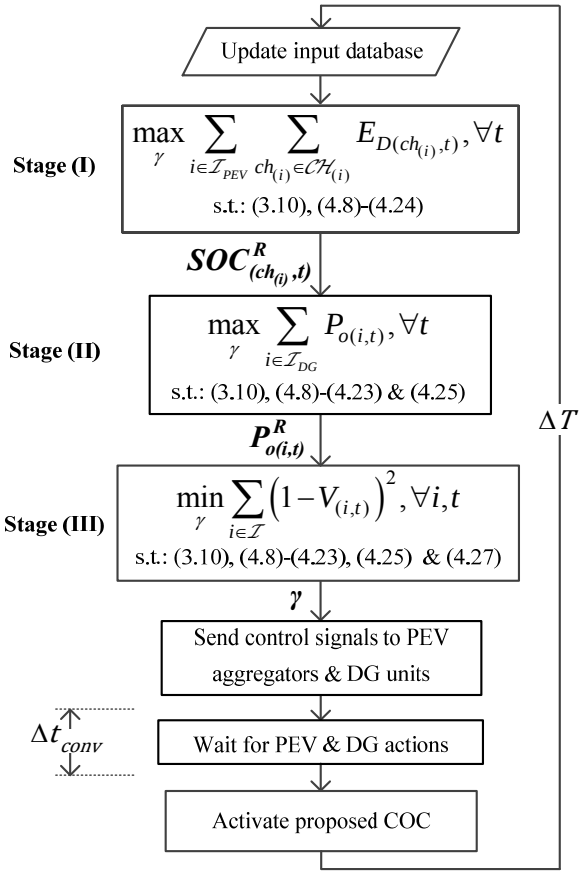

Figure 4.5: Proposed PEV/DG voltage support scheme

where $E_{D(\mathrm{ch(i),t})}$ is the energy delivered to the PEV connected to charger $ch_{(\mathrm{i})} \in \mathcal{CH}_{(\mathrm{i})}$ at PEV bus $i \in \mathcal{I}_{PEV}$; $\mathcal{I}_{PEV}$ is the set of buses with PEV charger connections; $\mathcal{CH}_{(\mathrm{i})}$ is the set of chargers connected to bus i; and γ is the decision variables vector. The PEV and DG voltage support depends mainly on γ, which can generally take the following form:

$$\gamma = \left[\mathbb{X}_{(ch_{(i)},t)}, Q^{PEV}_{o(i,t)}, P_{o(i,t)}, Q_{o(i,t)} \right] \tag{4.7}$$

where $\mathbb{X}_{(ch_{(i)},t)}$ and $Q^{PEV}_{o(i,t)}$ are the vector of the charger decisions and PEV reactive power at bus $i \in \mathcal{I}_{PEV}$, respectively; $P_{o(i,t)}$ and $Q_{o(i,t)}$ are the DG active and reactive powers at bus $i \in \mathcal{I}_{DG}$, respectively; and $\mathcal{I}_{DG}$ is the set of buses with DG connections. The charging decisions are continuous, i.e., $\mathbb{X} \in [0,1]$ where "0" stands for no charging and "1" stands for full charging. According to the grid operator, γ can be partially constrained. For instance, the PEV reactive powers

can be set to zero, i.e., $Q_{o(i,t)}^{PEV} = 0, \forall i \in \mathcal{I}_{PEV}, t$, when the PEV voltage support is disregarded. Stage (I) should satisfy the power flow constraints, as given by

$$P_{G(i,t)} - P_{L(i,t)} = \sum_{j \in \mathcal{I}_b} V_{(i,t)} V_{(j,t)} Y_{(i,j)} \cos\left(\theta_{(i,j)} + \delta_{(j,t)} - \delta_{(i,t)}\right) \qquad \forall i \in \mathcal{I}_b, t \tag{4.8}$$

$$Q_{G(i,t)} - Q_{L(i,t)} = \sum_{j \in \mathcal{I}_b} V_{(i,t)} V_{(j,t)} Y_{(i,j)} \sin\left(\theta_{(i,j)} + \delta_{(j,t)} - \delta_{(i,t)}\right) \qquad \forall i \in \mathcal{I}_b, t \tag{4.9}$$

where $P_{G(i,t)}$ and $Q_{G(i,t)}$ denote the generated active and reactive powers, respectively; $P_{L(i,t)}$ and $Q_{L(i,t)}$ are the active and reactive power demands, respectively; $V_{(i,t)}$ and $\delta_{(i,t)}$ denote the magnitude and angle of the voltage, respectively; $\mathcal{I}_b$ is the set of system buses, and $Y_{(i,j)}$ and $\theta_{(i,j)}$ are the magnitude and angle of the Y-bus admittance matrix, respectively.

The voltage and feeder thermal limits should also hold, and thus,

$$V_{\min} \le V_{(i,t)} \le V_{\max}, \quad \forall i \in \mathcal{I}_b, t \tag{4.10}$$

$$I_{(l,\mathrm{t})} \le I_{(l)}^{CAP}, \quad \forall l \in \mathcal{L}, t \tag{4.11}$$

where $V_{\min}$ and $V_{\max}$ are the maximum and minimum voltage limits, i.e., 0.9 and 1.1 pu, respectively; $I_{(l,\mathrm{t})}$ denotes the per unit current through line $l \in \mathcal{L}$; $\mathcal{L}$ is the set of system lines, and $I_{(l)}^{CAP}$ is the current carrying capacity. Constraint (4.10) should be accompanied with the OLTC feasibility constraint, defined in (3.10), to guarantee proper operation of the proposed COC.

Typically, there are two stages to interface PEVs and PVs: dc/dc conversion, and ac/dc conversion, as shown in Figure 4.1. The main function of the first stage is performing the MPPT in the case of PVs, or controlling the charging pattern of PEVs. The second stage regulates the dc-link voltage and controls the reactive power injection or absorption [18]. The power generated at each bus should match the output power of the DG connected to that bus:

$$\begin{cases} P_{G(i,t)} = P_{o(i,t)} \\ Q_{G(i,t)} = Q_{o(i,t)} \end{cases}, \qquad \forall i \in \mathcal{I}_{DG}, t \tag{4.12}$$

$$P_{o(i,t)} \le P_{o(i,t)}^{MPPT}, \qquad \forall i \in \mathcal{I}_{DG}, t \tag{4.13}$$

where $P_{o(i,t)}^{MPPT}$ is the DG available power extracted by a MPPT algorithm. In both PEVs and PVs, the ac/dc conversion is realized through a full converter similar to Type 4 wind farms. Thus, the reactive

power capability limits, defined in [82], can be adapted to fit PV and PEV reactive power applications. In [82], the reactive power is limited by the converter rating and dc-link voltage. Accordingly, the DG reactive powers limits are given by

$$Q_{o(i,t)}^2 \le S_{o(i,t)}^2 - P_{o(i,t)}^2, \qquad \forall i \in \mathcal{I}_{DG}, t \tag{4.14}$$

$$\left(Q_{o(i,t)} + \frac{V_{(i,t)}^2}{X_{(i)}} \right)^2 \le \left(\frac{V_{c(i)}^{\max} V_{(i,t)}}{X_{(i)}} \right)^2 - P_{o(i,t)}^2, \qquad \forall i \in \mathcal{I}_{DG}, t \tag{4.15}$$

where $S_{o(i,t)}$ is the DG rated power; $V_{c(i)}^{\max}$ is the maximum converter voltage which is limited by the converter dc-link voltage [82], [96]; $X_{(i)}$ represents the total reactance of the converter interfacing transformer and filter of the DG at bus i. It is worth mentioning that if the ac/dc converter is used to regulate the dc-link voltage at higher values to relax Constraint (4.15), then the dc/dc converter will operate at a higher duty cycle, which decreases its efficiency [97]. Thus, the dc-link voltage is considered as a limiting factor for the reactive power support, as reported in [82].

The total loading power should equal the sum of the power consumed by regular loads and PEV:

$$P_{L(i,t)} = P_{NL(i,t)} + P_{o(i,t)}^{PEV}, \qquad \forall i \in \mathcal{I}_b, t \tag{4.16}$$

$$Q_{L(i,t)} = Q_{NL(i,t)} + Q_{o(i,t)}^{PEV}, \qquad \forall i \in \mathcal{I}_b, t \tag{4.17}$$

where $P_{o(i,t)}^{PEV}$ is the PEV active power, and $P_{NL(i,t)}$ and $Q_{NL(i,t)}$ are the active and reactive powers of normal loads, respectively. Both $P_{o(i,t)}^{PEV}$ and $P_{o(i,t)}$ are independent on the grid voltage because the ac/dc converter keeps a constant dc-link voltage, which is considered a buffer between the ac and dc sides. Hence, PEV charging loads are modeled as CPLs in the power flow analysis [98]. The main differences between the PEVs and DGs are the power profile and direction. The PV power profile relies mainly on solar insolation, whereas $P_{o(i,t)}^{PEV}$ depends on charging decisions $\mathbb{X}_{(ch_{(i)},t)}$, the charging power limit in kW $P_{CH(ch_{(i)},t)}$, and the charging efficiency $\eta_{CH(ch(i))}$, as given by

$$P_{o(i,t)}^{PEV} = \sum_{ch_{(i)} \in \mathcal{CH}_{(i)}} \frac{\mathbb{X}_{(ch_{(i)},t)} P_{CH(ch_{(i)},t)}}{\eta_{CH(ch_{(i)})} S_{base}}, \quad \forall i \in \mathcal{I}_{PEV}, t \tag{4.18}$$

where S_{base} is the base power for the per unit system in kW. The charging power limit P_{CH} is a function of the PEV battery SOC and is limited by the capacity of the charger, i.e., $P_{CH} \le P_{rated}^{Charger}$. This function is dependent on the characteristics of the battery, which can be expressed as

$$P_{CH(ch_{(i)},t)} = f_{(ch_{(i)},t)}\left(SOC^{F}_{(ch_{(i)},t)}\right), \quad \forall i \in \mathcal{I}_{PEV}, ch_{(i)}, t \tag{4.19}$$

where $f_{(ch_{(i)},t)}$ is the function that represents the characteristics of the PEV battery, $SOC^{F}_{(ch_{(i)},t)}$ is the reached SOC. The relationship between the energy delivered to a PEV battery and its SOC can be given by

$$E_{D(ch_{(i)},t)} = E_{BAT(ch_{(i)})} \times \frac{\left(SOC^{F}_{(ch_{(i)},t)} - SOC^{I}_{(ch_{(i)},t)}\right)}{100}, \quad \forall i \in \mathcal{I}_{PEV}, ch_{(i)}, t \tag{4.20}$$

where $E_{BAT(ch_{(i)})}$ is the battery capacity in kWh and $SOC^{I}_{(ch_{(i)},t)}$ denotes the PEV initial SOC. The SOC of different PEVs are updated according to:

$$SOC^{F}_{(ch_{(i)},t)} = SOC^{I}_{(ch_{(i)},t)} + \frac{\mathbb{X}_{(ch_{(i)},t)} P_{CH(ch_{(i)},t)} \left(\frac{\Delta T}{60}\right)}{E_{BAT(ch_{(i)})}}, \quad \forall i \in \mathcal{I}_{PEV}, ch_{(i)}, t \tag{4.21}$$

where ΔT is the time step to collect the system data, run the program, and implement the decisions. Similar to DGs, the injected reactive powers from the PEVs should be limited by their converter ratings and dc-link voltages, as given by

$$\left(Q^{PEV}_{o(i,t)}\right)^2 \le \left(S^{PEV}_{o(i,t)}\right)^2 - \left(P^{PEV}_{o(i,t)}\right)^2, \qquad \forall i \in \mathcal{I}_{PEV}, t \tag{4.22}$$

$$\left(Q^{PEV}_{o(i,t)} + \frac{V^2_{(i,t)}}{X_{(i)}}\right)^2 \le \left(\frac{V^{\max}_{c(i)} V_{(i,t)}}{X_{(i)}}\right)^2 - \left(P^{PEV}_{o(i,t)}\right)^2, \qquad \forall i \in \mathcal{I}_{PEV}, t \tag{4.23}$$

where $S^{PEV}_{o(i,t)}$ is the rated power of the PEV converter. In addition, the final achieved SOC, i.e., $SOC^{F}_{(ch_{(i)},t)}$, should be limited by the SOC desired by the PEV owners $SOC^{D}_{(ch_{(i)},t)}$:

$$SOC^{F}_{(ch_{(i)},t)} \le SOC^{D}_{(ch_{(i)},t)}, \quad \forall i \in \mathcal{I}_{PEV}, ch_{(i)}, t \tag{4.24}$$

The upper bound of $SOC^{F}_{(ch_{(i)},t)}$ is considered to avoid the problem infeasibility, in case of high PEV penetration. These infeasible scenarios may occur due to the violation of some system constraints, such as the current carrying capacity constraint given by (4.11). If the solution is feasible, the

optimizer will maximize the energy delivered to PEVs, i.e., Stage (I) objective, which implies maximizing $SOC^{F}_{(ch_{(i)},t)}$ and targeting $SOC^{D}_{(ch_{(i)},t)}$. In other words, the optimizer always tries to narrow the gap between $SOC^{D}_{(ch_{(i)},t)}$ and $SOC^{F}_{(ch_{(i)},t)}$.

4.4.2 Problem Formulation of Stage (II)

In Stage (II), the objective is to minimize the DG active power curtailment, where the final SOC reached in Stage (I), i.e., $SOC^{R}_{(ch_{(i)},t)}$, must be attained to ensure maximum customer satisfaction, which is the highest priority of the proposed approach. Therefore, this stage is subject to all of the constraints in Stage (I) except for (4.24), which is replaced by

$$SOC^{F}_{(ch_{(i)},t)} = SOC^{R}_{(ch_{(i)},t)}, \quad \forall i \in \mathcal{I}_{PEV}, ch_{(i)}, t \tag{4.25}$$

Thus, Stage (II) can be defined as

$$\max_{\gamma} \sum_{i \in \mathcal{I}_{DG}} P_{o(i,t)}, \qquad \forall t \tag{4.26}$$

subject to (3.10), (4.8)-(4.23), and (4.25).

4.4.3 Problem Formulation of Stage (III)

The objective of Stage (III) is to minimize the voltage deviation and thus relax the OLTC operation. This problem is subject to all of the constraints of Stage (II). In addition, the maximum injected powers from the DGs reached in Stage (II), i.e., $P^{R}_{o(i,t)}$, must be maintained, as given by

$$P_{o(i,t)} = P^{R}_{o(i,t)}, \quad \forall i \in \mathcal{I}_{DG}, t \tag{4.27}$$

Therefore, the objective function of this stage can be defined as

$$\min_{\gamma} \sum_{i \in \mathcal{I}_{b}} \left(1 - V_{(i,t)}\right)^{2}, \quad \forall i, t \tag{4.28}$$

subject to (3.10), (4.8)-(4.23), (4.25), and (4.27).

4.4.4 Coordination with the proposed COC

The defined voltage control band, defined by (4.10), is wider than the standard voltage band, i.e., from 0.95 to 1.05, to avoid infeasible solutions, which may occur due to PEV and DG reactive power limits. Hence, Stage (III) has two objectives: 1) a direct objective, which aims to get the minimum possible voltage deviation using PEV/DG voltage support; and 2) indirect objective, which relaxes

the tap operation by considering the PEV/DG voltage support as the first line of defense in case of voltage violation.

As shown in Figure 4.5, the control signals generated by Stage (III) are sent to all PEV parking lots and DGs. A time delay Δt_{conv} is introduced to ensure that the PEV and DG converters reach the desired active and reactive power references. This time delay depends on the settling times of the converter primary controllers, which can vary from 50 to 100 ms [18]. According to IEC 61850, for slow automatic interactions, the maximum communication time delay is 100 ms [99]. Thus, Δt_{conv} is assumed to be 200 ms, to consider the worst case of 100 ms for the converter settling time and 100 ms for the communication latency. The total update time of the proposed coordination algorithm ΔT is 5 minutes. Lastly, the implemented solution from Stage (III) is refined using the proposed COC to ensure that both $V_{\min}^{sys}$ and $V_{\max}^{sys}$ are within the standard voltage band.

It is worth mentioning that the COC is coordinated with the optimal PEV and DG voltage supports rather than being incorporated in the optimization stages. To integrate the OLTC in the optimization stages, the problem needs to be solved for one day ahead [34], which makes it susceptible to forecasting errors and complicates the problem significantly. Such an approach is avoided in this study. If the OLTC is integrated in the optimization problem without considering the daily time window, the OLTC may suffer from excessive tap operation. The reason for the excessive tap operation is that the optimizer would have several options to regulate the voltage, i.e., the DG and PEV reactive powers, and the tap position. Considering PEV and DG voltage supports prior to activating the OLTC can result in a relaxed tap operation without the need for one-day-ahead optimization.

4.5 Real-Time Validation

Various case studies are presented in this section to test the robustness and effectiveness of the proposed optimal coordinated voltage regulation algorithm. The 38-bus 12.66-kV system, shown in Figure 4.6, is used as a test system [100]. It contains a mix of residential, commercial, and industrial loads that share 23 %, 67 %, and 10 % of the total system load, respectively. The system data are given in Appendix A. The total peak load of the system is 4.37 MVA. The system is modified to accommodate four PV-based DGs and two PEV parking lots, with power ratings given in Figure 4.6.

Information on the two parking lots is provided by TPA for a weekday in 2013. Both parking lots are commercial, with P1 representing a real parking lot located near a train station, and P2

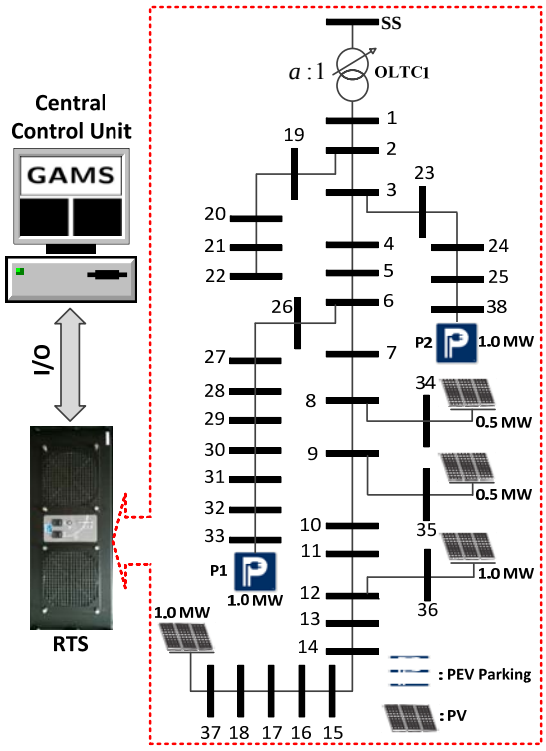

Figure 4.6: Test network with an HiL realization

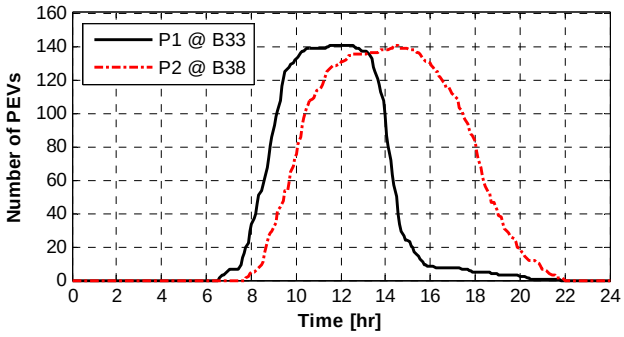

Figure 4.7: Number of vehicles in the parking lots

representing a real parking lot located close to downtown. Figure 4.7 shows the total PEVs at each time instant for the two parking lots. Due to confidentiality, the addresses of the real parking lots are not mentioned. The proposed central control unit receives the desired SOCs and sends the charging decisions to all vehicles in the parking lots. The RTS models the visual test network using the SimPowerSystems blockset, which is available in Simulink/Matlab, and an ARTEMiS plug-in from OPAL-RT. The network, PEV, and DG models are distributed between the RTS cores for performing parallel computations. The RTS it is used to perform the HiL realization, where a central control unit,

emulated by a host computer running GAMs, exchanges real-time data with the test network modeled in the RTS. The sampling time used to realize the HiL application is 100 μs. The PHiL application is avoided in this study due to hardware limitations and the time frame of the proposed supervisory control level. To test the robustness of the proposed algorithm, three scenarios are considered for the OLTC control. The parameters of the OLTCs are reported in Appendix A.

4.5.1 OLTC Control without PEV/DG Voltage Support

This section illustrates the interaction between PEVs, DGs, and OLTC under both conventional and proposed COC controllers. It is assumed that neither PEVs nor DGs participate in the voltage regulation. Figure 4.8(a) and Figure 4.8(b) illustrate the response of the OLTC over a 24-hour period, based on the conventional local control. Although there is no excessive tap operation (13 taps/day), the system voltage violates the standard limits at different operation conditions. The overvoltage problem is introduced during peak PV power generation. Contradictorily, the undervoltage happens during peak PEV charging. To tackle this voltage violation, the COC is introduced. Figure 4.8(c) and Figure 4.8(d) demonstrate the response of the proposed COC without the PEV/DG voltage support. Although the COC can provide a partial solution, it suffers from a hunting problem, and thus should be deactivated. The hunting problem happens because both the overvoltage and undervoltage occur simultaneously. In other words, Condition (3.10) is not satisfied.

4.5.2 OLTC Control with PEV/DG Voltage Support

To address the hunting problem, presented in the previous case, the PEV/DG voltage support needs to cooperate with the COC. Four case studies dealing with PEV/DG voltage support are carried out, as follows:

1. DG active power curtailment, without PEV and DG reactive power supports, i.e., $\gamma = \left[\mathbb{X}_{(ch_{(i)},t)}, P_{o(i,t)} \right]$, where $Q^{PEV}_{o(i,t)} = 0, \forall i \in \mathcal{I}_{PEV}$, and $Q_{o(i,t)} = 0, \forall i \in \mathcal{I}_{DG}$;

2. PEV reactive power dispatch, without DG reactive power support, i.e., $\gamma = \left[\mathbb{X}_{(ch_{(i)},t)}, Q^{PEV}_{o(i,t)}, P_{o(i,t)} \right]$, with $Q_{o(i,t)} = 0, \forall i \in \mathcal{I}_{DG}$;

3. DG reactive power dispatch, without PEV reactive support, i.e., $\gamma = \left[\mathbb{X}_{(ch_{(i)},t)}, P_{o(i,t)}, Q_{o(i,t)} \right]$, where $Q^{PEV}_{o(i,t)} = 0, \forall i \in \mathcal{I}_{PEV}$; and

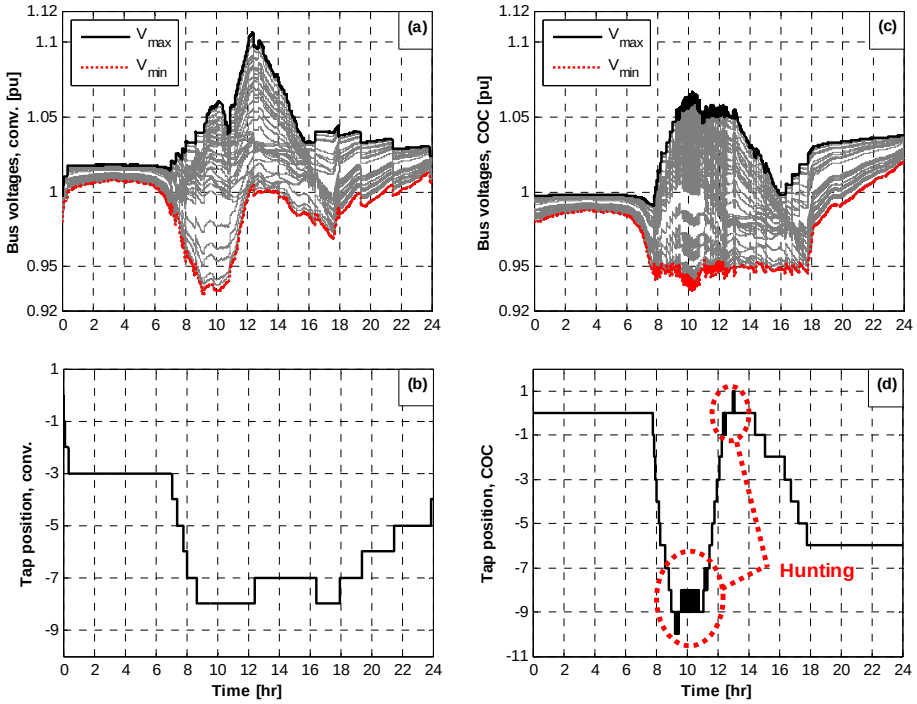

Figure 4.8: OLTC response: (a & b) conventional control, (c & d) proposed COC

4. PEV and DG reactive power dispatch, i.e., $\gamma = \left[\mathbb{X}_{(ch_{(i)},t)}, Q^{PEV}_{o(i,t)}, P_{o(i,t)}, Q_{o(i,t)} \right]$.

As discussed previously, DGs can provide voltage regulation by either reactive power support or active power curtailment. Figure 4.9 clarifies the response of the proposed coordination algorithm when the DG active power curtailment is merely considered. The proposed coordination algorithm results in a proper voltage regulation with reasonable tap operation (16 taps/day), as shown in Figure 4.9(a) and Figure 4.9(b). Furthermore, it satisfies the PEV charging demand by delivering all the required energy, as illustrated in Figure 4.9(c). However, 6.14 % of the DG available energy is curtailed, as shown in Figure 4.9(d). This is due to the highest priority given to the PEV charging load in the proposed approach. According to the distribution system code developed by the Ontario Energy Board, a local distribution company may disconnect loads for the following reasons: non-payment, emergency, safety, or technical limit violation [101]. In this work, it is assumed that the utility delivers the required PEV charging energy unless there is a technical limit violation. Hence, the PEV and DG reactive power support are essential to allow more DG-generated power injection with relaxed tap operation.

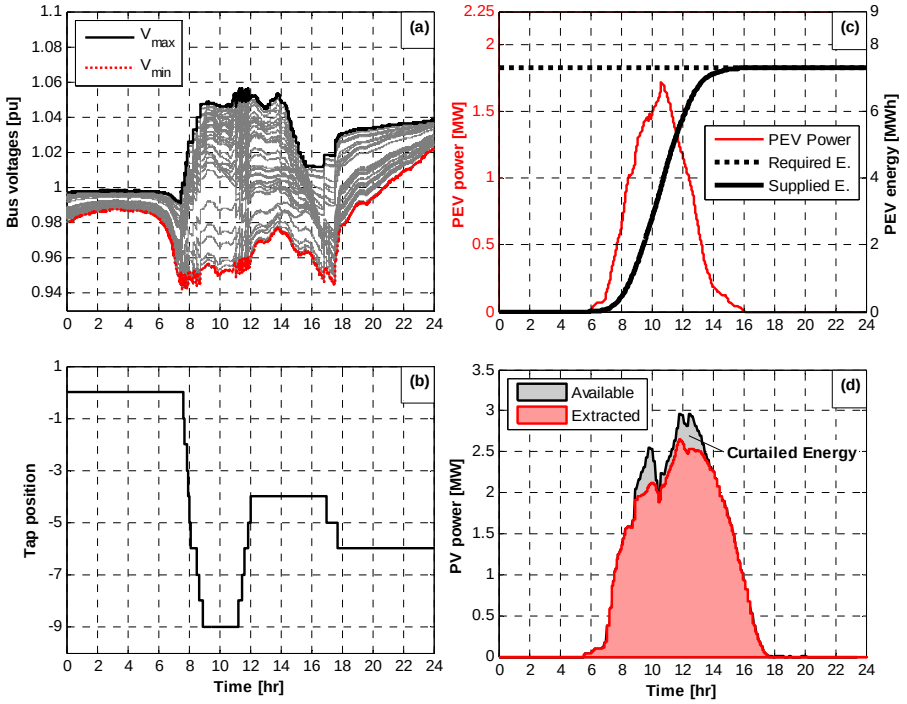

Figure 4.9: Response of proposed coordination algorithm, assuming DG active power curtailment

Figure 4.10 illustrates the response of the proposed coordination algorithm assuming PEV reactive power dispatch without DG reactive power support. The reactive power support of PEV can play an important role in voltage regulation. Utilizing PEV reactive power can relax the tap operation (10 taps/day) and maximize DG active power extraction. Alternatively, Figure 4.11 denotes the response of the proposed coordination algorithm utilizing DG reactive power dispatch without PEV reactive power support. DG reactive power can maximize the DG active power with reasonable tap operation (18 taps/day). DG reactive power support results in a relatively higher tap operation compared with PEV reactive power support, due to DG reactive power limitation during peak power generation. Finally, Figure 4.12 illustrates the response of the proposed coordination algorithm when both PEV and DG reactive power supports are incorporated in the voltage regulation. Combining both PEV and DG in the voltage regulation leads to a proper voltage regulation with relatively relaxed tap operation (4 taps/day) compared with all previous cases, while satisfying both PEV and DG self-objectives.

4.5.3 Coordination between Multiple OLTCs

Installing extra OLTCs in the system will provide more flexibility for the voltage regulation. Each OLTC will be responsible for regulating the voltage at a particular zone downstream of it to the next

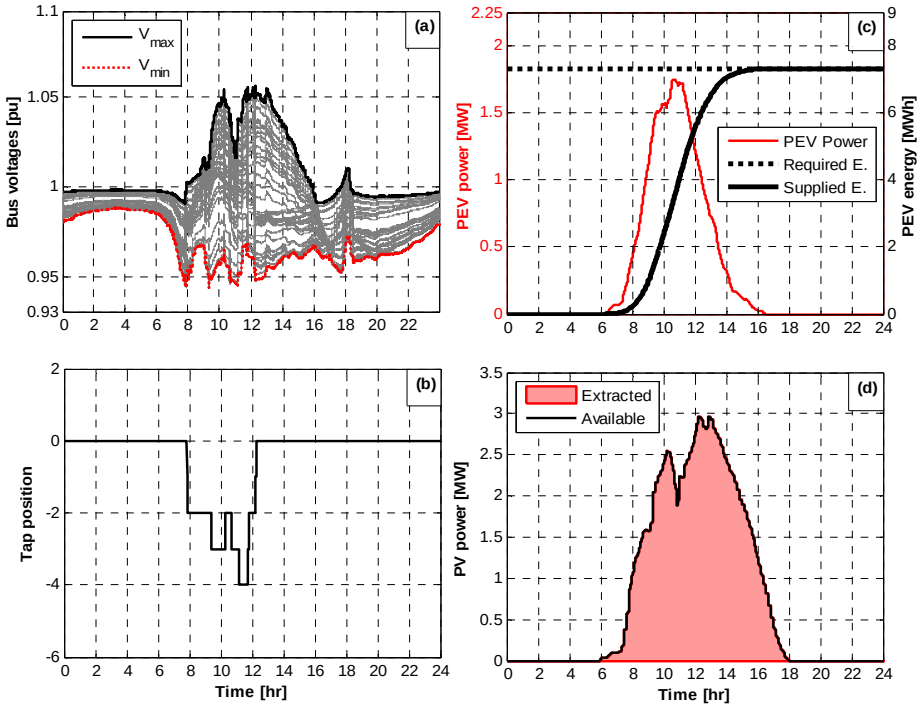

Figure 4.10: Response of proposed coordination algorithm, assuming PEV reactive power dispatch

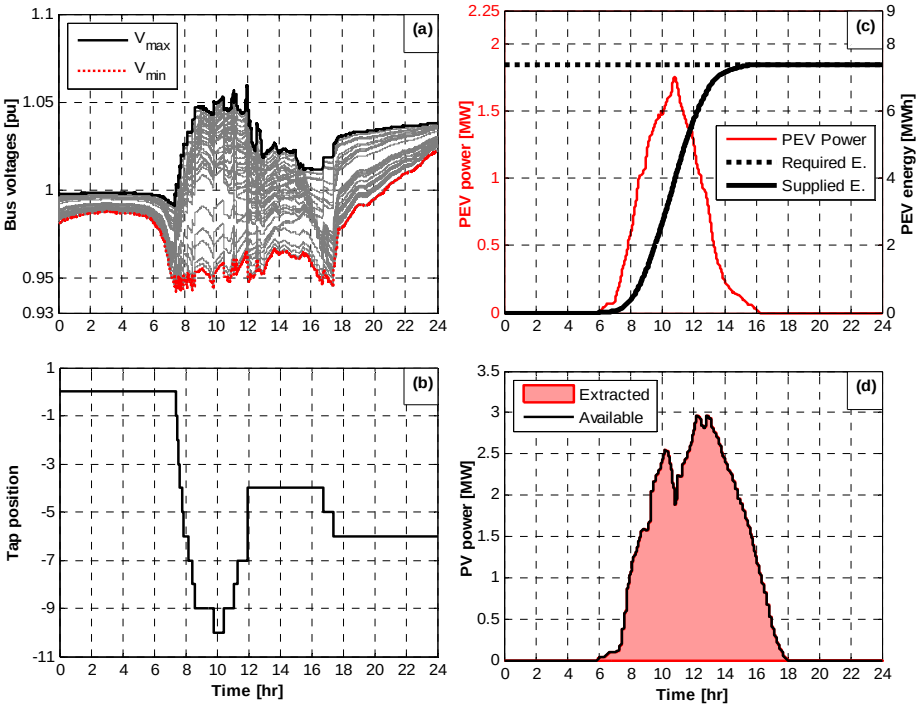

Figure 4.11: Response of proposed coordination algorithm, assuming DG reactive power dispatch

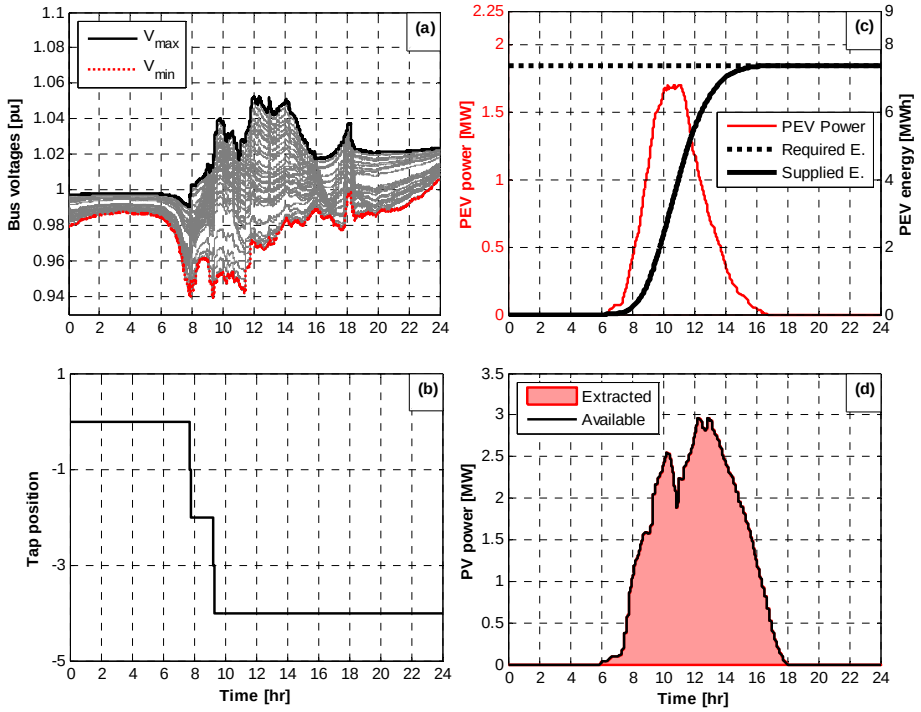

Figure 4.12: Response of proposed coordination algorithm, assuming both PEV and DG reactive power dispatch

OLTC, as shown in Figure 4.13. For each zone, the COC should reply on the maximum and minimum voltages of that particular zone. In addition, OLTC feasibility conditions, as defined by (3.10), need to be fulfilled for each voltage control zone. Therefore, (3.10) should be generalized as

$$\Delta V_{(z)} \le \Delta V_{Limit} - \Delta a_{(z)} \tag{4.29}$$

where $\Delta V_{(z)} = V^z_{\max} - V^z_{\min}$, $V^z_{\max}$ and $V^z_{\min}$ are the maximum and minimum voltage at zone z, and $\Delta a_{(z)}$ is the step change of the nominal turns ratio of the OLTC controlling zone z. Coordination between the OLTCs can be done through the control time delay, defined in (3.5). The downstream OLTCs should have less time delay as compared with the upstream OLTCs. When two zones are interconnected through a tie switch, forming a partially meshed network, the COCs of those interconnected zones should rely on the maximum and minimum voltages of the partially meshed network, while (4.29) can still be held.

To investigate the robustness of the proposed algorithm in dealing with multiple OLTCs, another OLTC, i.e., OLTC2, is installed downstream of Bus 6 in the test network. The extra OLTC allocation planning should ensure that the maximum and minimum voltages of the original system occur at two different control zones, to guarantee relaxed operation of the OLTCs [37]. Four different cases are

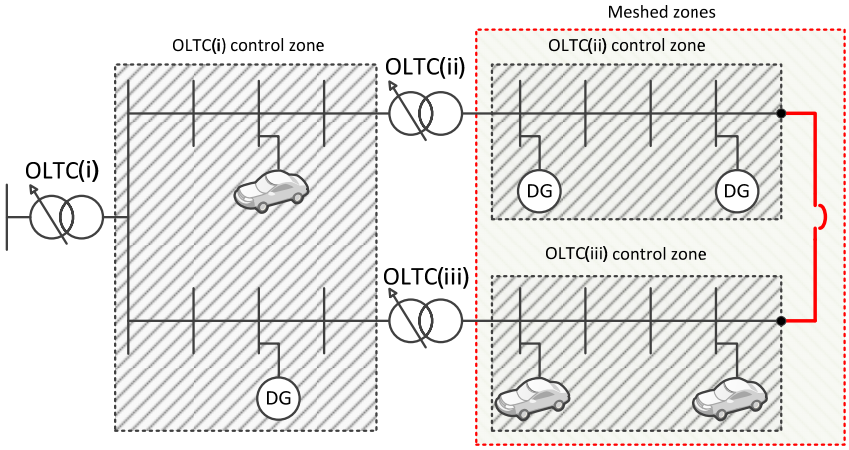

Figure 4.13: Control zones for multiple OLTCs

considered. Figure 4.14(a) and Figure 4.14(b) demonstrate the response of the proposed COC, without the DG and PEV voltage support. Compared to Case A, the hunting problem is solved when an extra OLTC is installed in the system, and thus, there is no need to curtail DG active powers.

A more relaxed operation for both OLTC1 and OLTC2 can be attained when the DG and PEV reactive power supports are involved in voltage regulation. Figure 4.14(c) and Figure 4.14(d) indicate the response of the proposed algorithm when the DG reactive power support is activated. The tap operation of OLTC2 is reduced from 15 taps/day to 5 taps/day. Activating the PEV reactive power support without the DG reactive power relaxes both OLTCs, as indicated in Figure 4.14(e) and Figure 4.14(f). Maximum relaxation occurs when both PEV and DG reactive power supports are involved in voltage regulation, as shown in Figure 4.14(g) and Figure 4.14(h). In this instance, the proposed algorithm regulates the system voltage without the need of activating OLTC2. In all four cases, the proposed algorithm can satisfy the desired SOC and maximize DG active powers. Although installing extra OLTCs can relax the tap operation and avoid hunting problems, the application of the proposed algorithm can defer the need for installing extra OLTCs.

Lastly, the proposed algorithm is tested with multiple OLTCs in a partially meshed network, which is formed by closing a tie switch between Buses 33 and 37. The conventional OLTC controllers result in an excessive tap operation, as shown in Figure 4.15(a) and Figure 4.15(b). Applying the proposed algorithm with activated DG and PEV reactive power supports results in only one tap operation for OLTC1, while satisfying the self-objectives of PEVs and DGs. These results prove the validity of the proposed algorithm in dealing with multiple OLTCs in partially meshed networks. The application of the proposed algorithm can also defer the need of installing extra

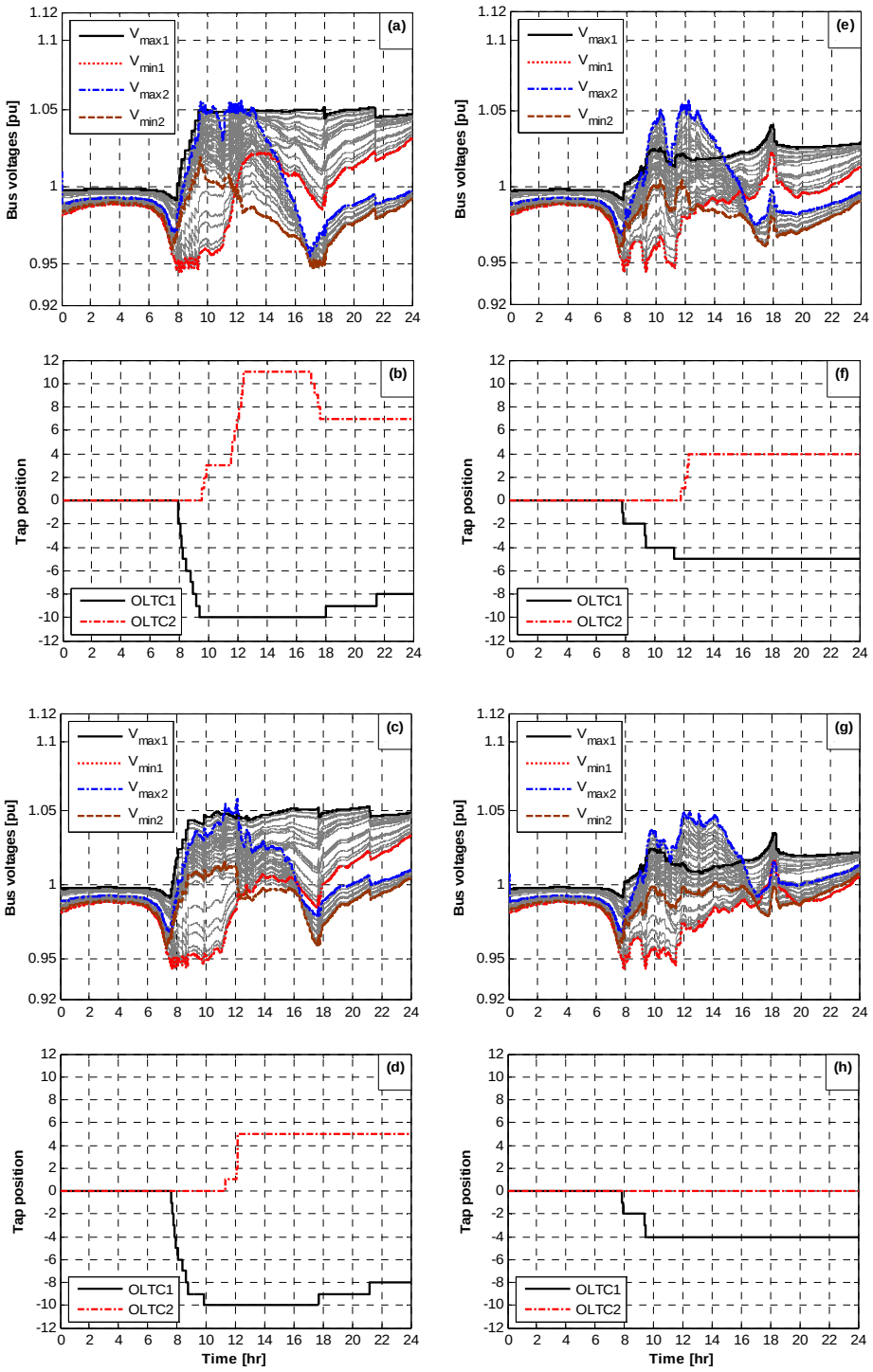

Figure 4.14: Responses of multiple OLTCs: (a & b) without PEV and DG voltage support, (c & d) with DG reactive power support, (e & f) with PEV reactive power support, (g & h) with both PEV and DG reactive power supports

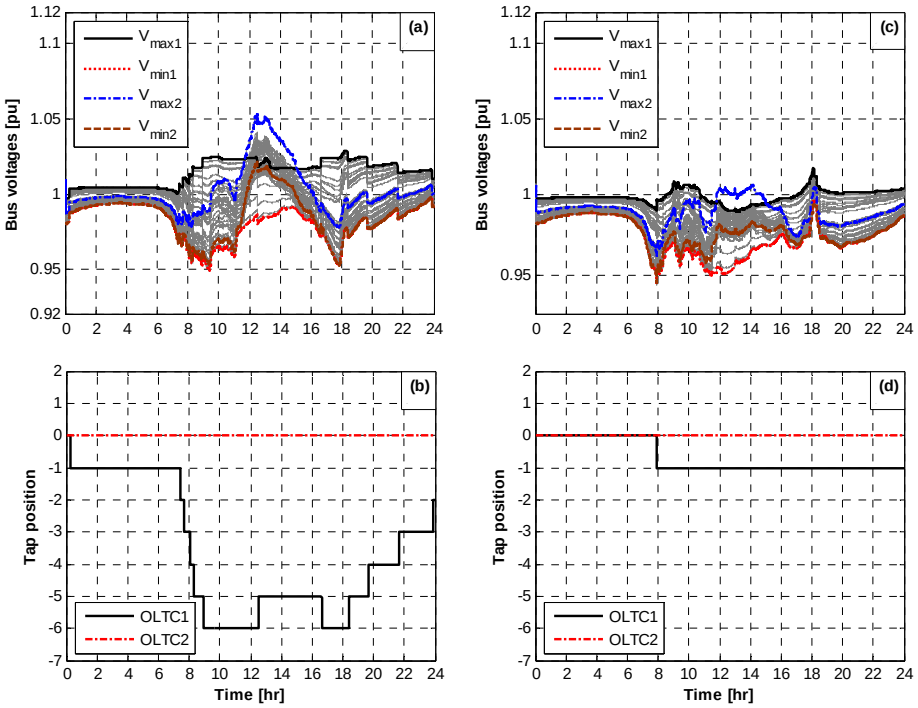

Figure 4.15: Responses of OLTCs in a meshed network: (a & b) conventional OLTC control, (c & d) proposed algorithm with PEV and DG reactive power supports

OLTCs in partially meshed networks. It is noteworthy that the voltage violation in partially meshed networks is less severe than that in radial networks due to reduced reverse power flow in partially meshed networks.

4.6 Discussion

This chapter studied the interactions of PEVs, DGs and OLTCs. A high penetration of PEVs and DGs can have negative impacts on OLTCs and can also result in a hunting problem. The main reason for this problem is the chronological power profiles of PEVs and renewable DGs that stimulate both overvoltage and undervoltage simultaneously. A new optimal coordinated voltage regulation scheme was proposed to tackle this problem and satisfy the self-objective of each voltage control device (i.e., OLTC operators need to relax the tap operations to extend the OLTC life times, PEV owners need to maximize their SOC, and DG owners need to reduce their active power curtailments).

The proposed voltage regulation was formulated as a non-linear programming consisting of a three-stage optimization problem. These stages aim to: 1) satisfy the PEV power demand, 2) maximize the DG-extracted power, and 3) minimize the system voltage deviation. The implicit objective of the third stage was to relax OLTCs, as both DGs and PEVs are considered primary voltage control

devices. Real-time simulations were performed to show the effectiveness of the proposed algorithm using OPAL RTS in an HiL application. The real-time simulations clarified the OLTC hunting problem and illuminated the role of PEV and DG reactive powers in the solution. The results also demonstrated the ability of the proposed coordination to maximize PEV demand power and PV extracted power, relax OLTC tap operation, and defer the need to install extra OLTCs.

Chapter 5
Multivariable Grid Admittance Identification for Impedance Stabilization of ADNs

5.1 Introduction

Previous chapters present new DG supervisory level control algorithms that adapt the DG active and reactive power references to mainly achieve proper voltage regulation in ADNs with relaxed OLTC operation under different load/generation power profiles, and grid topologies. In order to guarantee a stable performance of the DG primary controllers, while implementing the dispatched DG active and reactive powers, the DG output impedance should be adaptively reshaped. This adaptation should take into account the time-varying operating points and the uncertainty in the grid impedance. As reported in [102], [103], a stable DG connected to a certain grid can suffer from instability when connected to another grid with different impedance. In [20], the effect of CPLs on the DG performance is investigated, indicating negative impedance instability due to the tight regulation. Increasing the grid inductance may also lead to unstable DG performance as discussed in [73]. Thus, conventional design techniques may lead to instability issues because they ignore the interaction between the DG and grid. DG primary controllers can be designed by assessing the system eigenvalues of its corresponding detailed state-space model. Practically, power system engineers do not have access to the details of all converter-based DGs and loads connected to the system, and thus, assessing the system stability using the detailed state-space model becomes impossible. On the other hand, impedance-based stability criteria represent the system under study by two interconnected subsystems, i.e., DG and grid impedances. In such a case, the detailed information about the grid components does not need to be disclosed. From that perspective, the impedance stability criteria can be considered valuable tools that can be used to assess the system stability and design DG controllers.

In order to design DG adaptive controllers based on the impedance criteria, both DG and grid impedances need to be known beforehand. This chapter and the next one discuss the multivariable grid impedance identification and the multivariable DG impedance modeling, which are then utilized to design DG adaptive controllers. In this chapter, a novel online multivariable identification algorithm with adaptive model order selection is proposed for estimating the grid admittance

(impedance). It is noteworthy, the terms "grid impedance" and "grid admittance" are used interchangeably. The advantage of the proposed algorithm is that it is able to estimate both passive and active grid admittances without additional hardware. The new algorithm utilizes a refined instrumental variable for continuous-time (CT) system identification (RIVC) [104]. The RIVC can provide direct CT identification for the grid admittance model, offering the following benefits not available with discrete-time (DT) identification [105]–[107]:

1. Direct physical insight into system properties, such as the system time constant and damping
2. Freedom from dependence on the sampling period, with the ability to deal with non-uniform sampled data
3. Inherited prefiltering that can improve the statistical efficiency of the estimated parameters

The RIVC can also deal with technical issues arising from direct CT identification: the need for input-output time derivatives and noise modeling. The first issue is addressed by means of state-variable filters, and the second is avoided altogether because of the RIVC hybrid-parameterization structure, which identifies a DT model for noise and a CT model for the process.

The proposed algorithm is capable of adapting the grid admittance model structure online in order to provide accurate estimation without over-parameterization [108]. An over-parameterized model tends to increase computational time and can also fail to capture the underlying dynamics represented by excited grid admittance. An additional suggestion presented in this chapter is a new grid admittance excitation method, which is based on sensitivity analysis in order to guarantee persistence of excitation (PE) through the injection of controlled voltage pulses by the DG control system. A PE condition is necessary for nonlinear model identification because it improves the convergence of the parameters and attenuates the effect of measurement noise [109]. The final element described in this chapter is the real-time validation of the proposed identification algorithm in both grid-connected and isolated microgrids using the RTS provided by OPAL with an HiL application.

This chapter is organized as follows. Section 5.2 illustrates the effect of grid impedance variation on the system dynamic performance. Section 5.3 describes the problem of active grid admittance identification, and Section 5.4 explains the theoretical background of the RIVC. Section 5.5 discusses grid admittance excitation and the selection of the model structure. Validation results and conclusions are presented in Section 5.6 and Section 5.7, respectively.

5.2 Effect of the Grid Impedance on the system Stability

To show the effect of varying the grid impedance on the system stability, two scenarios are presented in this section. The first scenario examines the performance of a PQ-based (dispatchable) DG connected to a grid which is modeled by a voltage source in series with a grid Thevenin's impedance. Two case studies are considered in this scenario, namely, stiff and weak grid cases. To emulate the stiff grid case, the grid impedance parameters, i.e., R_g and L_g, are adjusted at 0.1 Ω and 1.0 mH, respectively; while 0.3 Ω and 3.0 mH are assigned to R_g and L_g in the case of weak grid, respectively. The PQ-based DG control parameters are fixed in both cases. Figure 5.1 illustrates the response of the PQ-based DG when its active and reactive power references are increased by 20% at $t = 0.5$ s. The DG can exhibit a stable performance when the grid impedance is low, i.e., the stiff grid condition, as indicated in Figure 5.1(a). The DG active and reactive power can track their reference values, and the DG output current and voltage neither suffer from oscillations nor harmonic distortions. Conversely, the DG performance in the case of weak grid is demonstrated in Figure 5.1(b). At the moment of increasing the DG active and reactive power references, i.e., $t = 0.5$ s, the DG output power, voltage, and current oscillate excessively, indicating instability. These results coincide with the conclusion reported by [73] that the relates the decrease of the stability margin to the increase of the grid inductance.

In the second scenario, the dynamic performance of a droop-based DG is examined when it supplies a CPL, creating a simple DG-load configuration. The impedance models for the DG and CPL are explained briefly in Chapter 6 and Appendix B, respectively. For a light load, i.e., case A, the system maintains stability because the Nyquist plot remains within the unit circle, as shown in Figure 5.2(a). However, with a sudden load increase, i.e., case B, an encirclement of -1 happens, indicating impedance instability that results in an oscillatory performance, as shown in Figure 5.2(b). These results also illustrates the impedance instability associated with CPLs (tightly regulated converters). Such loads have inherited negative input impedances which decrease the overall stability margin. This negative impedance can be understood by the fact that when the CPL terminal voltage increases, the drawn current decreases, and vice versa. Although, the DG control parameters are fixed in the above two scenarios, the DG responses differently when the grid impedance changes. Unless the grid impedance is identified, the DG output impedance cannot be reshaped so that system stability is restored.

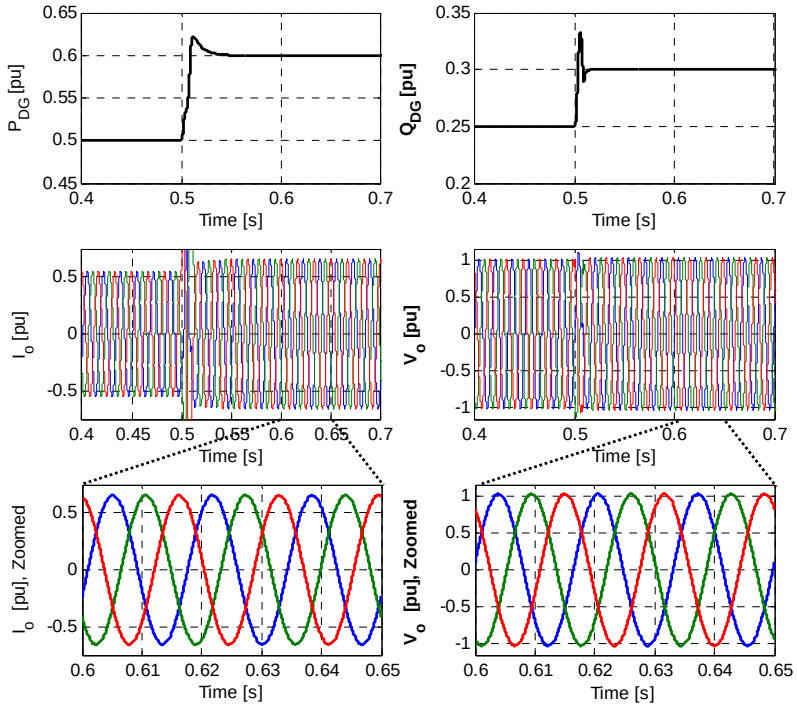

(a)

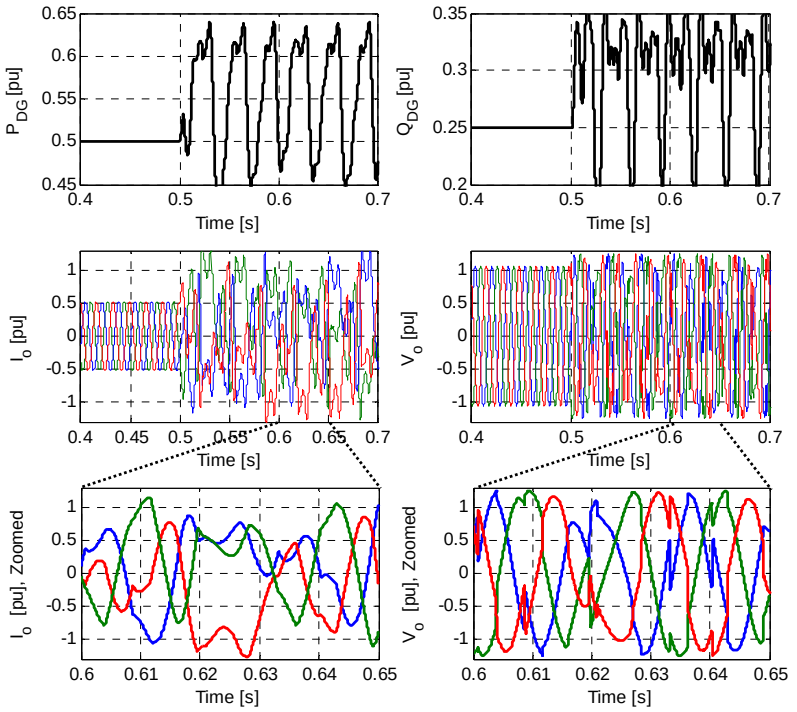

(b)

Figure 5.1: Effect of the grid impedance on the performance of PQ-based DG: (a) stiff grid; (b) weak grid

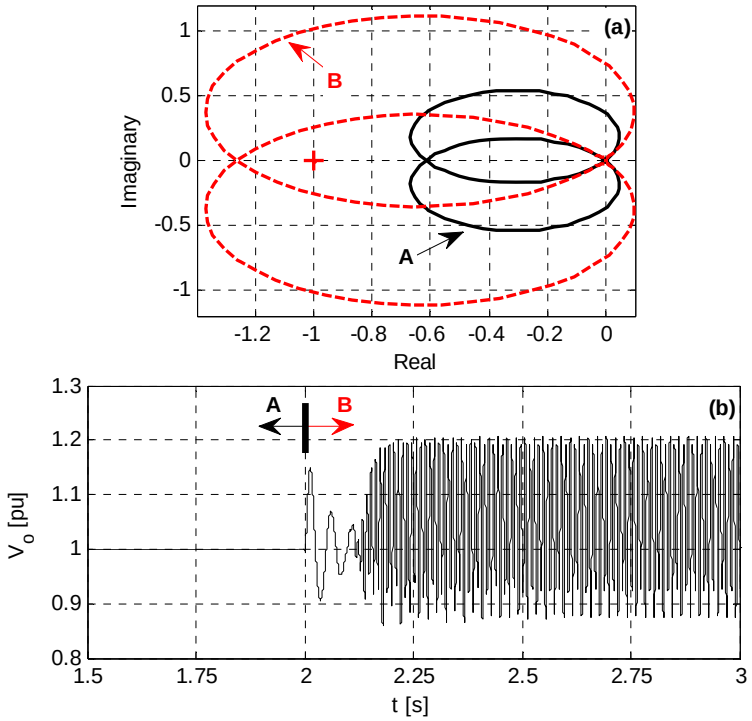

Figure 5.2: Stability of a DG-CPL system: (a) Nyquist plots; (b) DG output voltage

5.3 Multivariable Grid Admittance Modeling

For three-phase ac systems, an equilibrium dc operating point can be obtained when the system is modeled using a synchronously rotating $d-q$ reference frame. Thus, the grid admittance $\mathrm{Y_{Grid}}$ is a 2×2 transfer matrix that can be formulated as

$$\begin{bmatrix}\Delta I_{od}\\ \Delta I_{oq}\end{bmatrix}=\underbrace{\begin{bmatrix}Y_{g,dd} & Y_{g,dq}\\ Y_{g,qd} & Y_{g,qq}\end{bmatrix}}_{\mathrm{Y_{Grid}}}\begin{bmatrix}\Delta V_{od}\\ \Delta V_{oq}\end{bmatrix} \tag{5.1}$$

where ΔI_{odq} and ΔV_{odq} are the small perturbations of the DG output current and voltage, respectively, around a specific operating point. Previous estimated models of grid admittance were assumed to be represented by a combination of passive elements: R_g, L_g, and C_g, which create a passive grid admittance model. However, this assumption is imprecise since grid admittance is dependent on other DG and CPL impedances, which are time-varying and nonlinear. Grid admittance should therefore be represented by an active model. This section illustrates the differences between

passive and active grid admittance models. For a passive grid, DG output voltages can be expressed in a synchronous $d-q$ frame as

$$V_{od} - V_{gd} = (R_g + sL_g)I_{od} - \omega L_g I_{oq} \tag{5.2}$$

$$V_{oq} - V_{gq} = (R_g + sL_g)I_{oq} + \omega L_g I_{od} \tag{5.3}$$

where R_g, L_g, and ω are the equivalent grid resistance, inductance, and system frequency, respectively. The DG output voltages can be represented in a small-signal sense as

$$\Delta V_{od} = (R_g + sL_g)\Delta I_{od} - \omega_o L_g \Delta I_{oq} \tag{5.4}$$

$$\Delta V_{oq} = (R_g + sL_g)\Delta I_{oq} + \omega_o L_g \Delta I_{od} \tag{5.5}$$

The passive grid admittance $\mathrm{Y_{Grid}}$ can thus be given by

$$\begin{aligned} \mathrm{Y_{Grid}(s)} &= \frac{\begin{bmatrix} R_g + sL_g & \omega_o L_g \\ -\omega_o L_g & R_g + sL_g \end{bmatrix}}{L_g^2 s^2 + 2L_g R_g s + \left(R_g^2 + \omega_o^2 L_g^2\right)} \\ &= \begin{bmatrix} Y_{g,dd}(\mathrm{s}) & Y_{g,dq}(\mathrm{s}) \\ Y_{g,qd}(\mathrm{s}) & Y_{g,qq}(\mathrm{s}) \end{bmatrix} \end{aligned} \tag{5.6}$$

where ω_o is the system frequency at a specific operating point. As determined from (5.6), grid admittance can be modeled using a proper second-order transfer matrix with three unknowns: R_g, L_g, and ω_o. Rather than identifying four second-order transfer functions, (5.4) and (5.5) can be reformulated to incorporate four first-order transfer functions, as follows:

$$\Delta I_{od} = G_1(\mathrm{s})\Delta V_{od} + G_2(\mathrm{s})\Delta I_{oq} \tag{5.7}$$

$$\Delta I_{oq} = G_3(\mathrm{s})\Delta V_{oq} + G_4(\mathrm{s})\Delta I_{od} \tag{5.8}$$

where

$$\begin{cases} G_1(\mathrm{s}) = G_3(\mathrm{s}) = \dfrac{1}{R_g + sL_g} \\ G_2(\mathrm{s}) = -G_4(\mathrm{s}) = \dfrac{\omega_o L_g}{R_g + sL_g} \end{cases} \tag{5.9}$$

The grid admittance matrix can hence be written in terms of G_1, G_2, G_3, and G_4 as

$$Y_{\text{Grid}}(s) = \frac{\begin{bmatrix} G_1(s) & G_2(s)G_3(s) \\ G_1(s)G_4(s) & G_3(s) \end{bmatrix}}{1 - G_2(s)G_4(s)} \tag{5.10}$$

The model given by (5.7) and (5.8) represents two continuous multi-input-single-output (MISO) systems. The RIVC is applied in order to identify its parameters. The theoretical background of the RIVC and the proposed model order selection are explained briefly in Sections 5.4 and 5.5, respectively.

Inverter-based DGs are typically connected to one of two types of ADN topologies: grid-connected and isolated-microgrid [4]. In a grid-connected topology, the system voltage and frequency are governed by the grid, and the DGs usually operate in current-control mode. In contrast, in isolated microgrids, at least one DG must operate according to droop characteristics, acting as a slack bus, in order to balance the grid voltage and frequency. The remaining DGs can either operate according to droop characteristics or track maximum renewable power levels. Figure 5.3 represents two islanded microgrids. The grid admittance in such a case is the equivalent load admittance. In Figure 5.3(a), the load admittance is passive because it consists of passive elements, while in Figure 5.3(b), the grid admittance is active because it comprises the admittance of DG2. Without loss of generality, DG1 is assumed to operate according to droop characteristics, whereas DG2 represents a PV-based DG that tracks the maximum available solar power. Figure 5.4 indicates the estimated DG output currents when DG1 is connected to the passive microgrid admittance shown in Figure 5.3(a). Assuming first-order transfer functions for G_1, G_2, G_3, and G_4 leads to an accurate matching between the actual and estimated DG output currents. This result conforms to the typically considered assumption regarding grid admittance, i.e., that it consists of passive elements. On the other hand, Figure 5.5 illustrates the estimated currents output by DG1 when it is connected to the active microgrid admittance depicted by Figure 5.3(b). A first-order transfer function model for G_1, G_2, G_3, and G_4 fails to provide accurate matching between the actual and estimated DG output currents. This mismatch confirms that the grid admittance structure has shifted from its conventional passive nature to an active one. Although the estimate of ΔI_{od} looks reasonable, it is not as accurate as in the passive grid case illustrated in Figure 5.4. If that reasonable estimate implies appropriate identification of G_1 and G_2, the identified G_3 and G_4 are still inaccurate because of the imprecise estimate of ΔI_{oq}. Consequently, the estimated Y_{Grid} cannot represent the actual dynamics of the grid admittance, based on the first-order transfer function modeling.

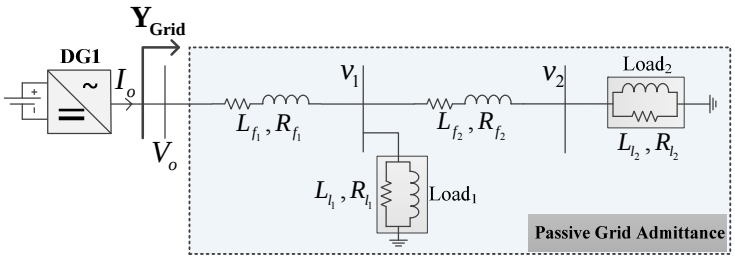

(a)

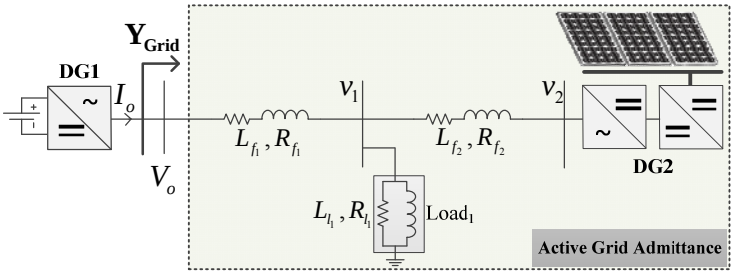

(b)

Figure 5.3: Grid admittance from DG1 perspective: (a) passive grid admittance model; (b) active grid admittance model

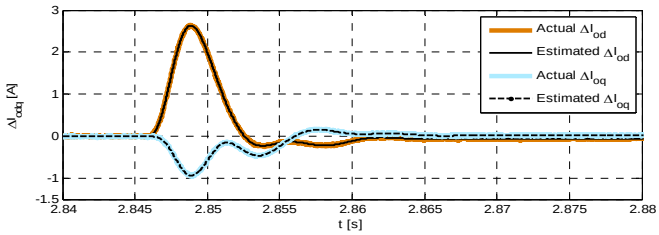

Figure 5.4: Estimated DG output currents for a passive grid, assuming a first-order model

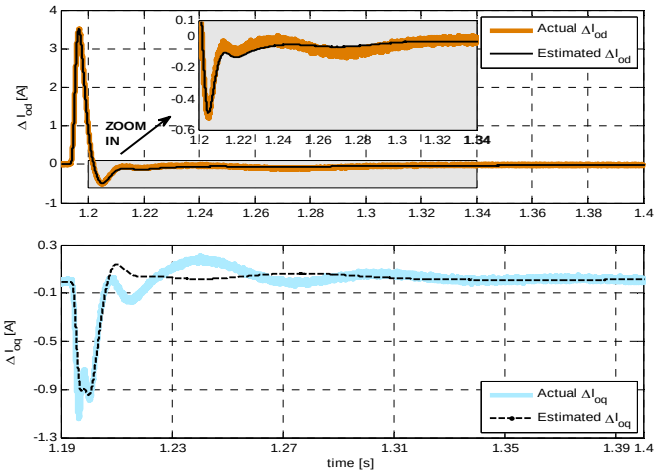

Figure 5.5: Estimated DG output currents for an active grid, assuming a first-order model

The next section discusses the online identification of the multivariable grid admittance model with an active nature. The proposed identification algorithm is generic, i.e., applicable for both passive and active grid admittances. It can be added as an ancillary function within DSP-based DG controllers, for both grid-connected and isolated microgrid topologies, without the need for extra hardware.

5.4 Continuous-Time Grid Admittance Identification

A linear time-invariant MISO CT system, with n_u input values and a single output value, can be described using the following differential equation:

$$x(t) = \frac{B_1(p)}{A(p)}u_1(t) + \frac{B_2(p)}{A(p)}u_2(t) + \cdots + \frac{B_{n_u}(p)}{A(p)}u_{n_u}(t) \tag{5.11}$$

where $x(t)$ is the noise-free output and $u_1(t), u_2(t), \cdots, u_{n_u}(t)$ represent the input. Both input and output are assumed to be uniformly sampled with a sampling time of $h \in \Re^+$ at $t_k = kh$ for $k = 1, 2, \cdots, N$, where N is the total number of samples. To simplify the notation, p is introduced as the differential operator: $p^i x(t) = \mathrm{d}^i x(t) / \mathrm{d}t^i$. The MISO system given by (5.11) can fit the grid admittance model described by (5.7) and (5.8), as follows:

$$\Delta X_{od}(t) = \underbrace{\left(\frac{B_1(p)}{A_d(p)}\right)}_{G_1}\Delta V_{od}(t) + \underbrace{\left(\frac{B_2(p)}{A_d(p)}\right)}_{G_2}\Delta I_{oq}(t) \tag{5.12}$$

$$\Delta X_{oq}(t) = \underbrace{\left(\frac{B_3(p)}{A_q(p)}\right)}_{G_3}\Delta V_{oq}(t) + \underbrace{\left(\frac{B_4(p)}{A_q(p)}\right)}_{G_4}\Delta I_{od}(t) \tag{5.13}$$

with

$$\begin{cases} B_1(p) &= \mathrm{b}_{(0,1)}\, p^{m_1} + \mathrm{b}_{(1,1)}\, p^{m_1-1} + \cdots + \mathrm{b}_{(m_1,1)} \\ B_2(p) &= \mathrm{b}_{(0,2)}\, p^{m_2} + \mathrm{b}_{(1,2)}\, p^{m_2-1} + \cdots + \mathrm{b}_{(m_2,2)} \\ B_3(p) &= \mathrm{b}_{(0,3)}\, p^{m_3} + \mathrm{b}_{(1,3)}\, p^{m_3-1} + \cdots + \mathrm{b}_{(m_3,3)} \\ B_4(p) &= \mathrm{b}_{(0,4)}\, p^{m_4} + \mathrm{b}_{(1,4)}\, p^{m_4-1} + \cdots + \mathrm{b}_{(m_4,4)} \\ A_d(p) &= p^{n_d} + a_{1d}\, p^{n_d-1} + \cdots + a_{n_d} \\ A_q(p) &= p^{n_q} + a_{1q}\, p^{n_q-1} + \cdots + a_{n_q} \end{cases} \tag{5.14}$$

where X_{od} and X_{oq} are the $d-q$ components of the noise-free DG output currents, and $m_1,\cdots,m_4$, and n_d and n_q are the numerator and denominator orders, respectively. For proper MISO models, $n_d \geq \max(m_1, m_2)$ and $n_q \geq \max(m_3, m_4)$.

An additive noise $\varepsilon_{dq}(t_k)$ can be considered to be superimposed on the output $\Delta X_{odq}(t_k)$ to generate the measured output $\Delta I_{odq}(t_k)$, i.e.,

$$\Delta I_{od}(t_k) = \Delta X_{od}(t_k) + \varepsilon_d(t_k) \tag{5.15}$$

$$\Delta I_{oq}(t_k) = \Delta X_{oq}(t_k) + \varepsilon_q(t_k) \tag{5.16}$$

The primary objective is to identify the CT model parameters in (5.14), i.e., $a_{1d},\cdots,a_{n_d}$, $a_{1q},\cdots,a_{n_q}$ and $b_{(0,1)},\cdots,b_{(m_1,1)},\cdots,b_{(0,4)},\cdots,b_{(m_4,4)}$, based on N acquired samples of the system output and input: $\left\{\Delta I_{odq}(t_k), \Delta V_{odq}(t_k), \Delta I_{oqd}(t_k)\right\}_{k=1}^{N}$.

As an illustrative example that provides a better explanation of the RIVC and its simplified version (SRIVC) [105], the algorithm has been employed to estimate $\Delta I_{od}(t_k)$. From (5.12) and (5.15), the additive noise $\varepsilon_d(t_k)$ can be written as

$$\begin{aligned}\varepsilon_d(t_k) &= \Delta I_{od}(t_k) - \frac{B_1(p)}{A_d(p)}\Delta V_{od}(t_k) - \frac{B_2(p)}{A_d(p)}\Delta I_{oq}(t_k) \\ &= A_d(p)\Delta I_{od,f_A}(t_k) - B_1(p)\Delta V_{od,f_A}(t_k) - B_2(p)\Delta I_{oq,f_A}(t_k)\end{aligned} \tag{5.17}$$

where

$$\begin{cases} \Delta I_{od,f_A}(t_k) &= \dfrac{1}{A_d(p)}\Delta I_{od}(t_k) \\ \Delta V_{od,f_A}(t_k) &= \dfrac{1}{A_d(p)}\Delta V_{od}(t_k) \\ \Delta V_{od,f_A}(t_k) &= \dfrac{1}{A_d(p)}\Delta I_{oq}(t_k) \end{cases}. \tag{5.18}$$

To avoid the problem associated with measuring the time-derivatives, the output and input are filtered, using $A_d(p)$. Based on (5.17), the CT linear regression model can be given as

$$\Delta I_{od,f_A}^{(n_d)}(t_k) = \phi_{f_A}^T(t_k)\theta_e + \varepsilon_d(t_k). \tag{5.19}$$

where

$$\phi_{f_A}(t_k)=\Big[-\Delta I_{od,f_A}^{(n_d-1)}(t_k),-\Delta I_{od,f_A}^{(n_d-2)}(t_k),\cdots,-\Delta I_{od,f_A}(t_k)$$
$$\Delta V_{od,f_A}^{(m_1)}(t_k),\Delta V_{od,f_A}^{(m_1-1)}(t_k),\cdots,\Delta V_{od,f_A}(t_k) \tag{5.20}$$
$$\Delta I_{oq,f_A}^{(m_2)}(t_k),\Delta I_{oq,f_A}^{(m_2-1)}(t_k),\cdots,\Delta I_{oq,f_A}(t_k)\Big]^T,$$

$$\theta_e=\Big[a_{1d},\cdots,a_{n_d},b_{(0,1)},\cdots,b_{(m_1,1)},b_{(0,2)},\cdots,b_{(m_2,2)}\Big]^T. \tag{5.21}$$

In these calculations, $\Delta I_{odq,f_A}^{(i)}(t_k)$ and $\Delta V_{od,f_A}^{(i)}(t_k)$ represent the i^{th} time derivatives of $\Delta I_{odq,f_A}(t_k)$ and $\Delta V_{od,f_A}(t_k)$, respectively. For example, the filtered output $\Delta I_{od,f_A}(t_k)$ and its derivatives $\Delta I_{od,f_A}^{(i)}(t_k)$ can be acquired by sampling the states of the controllable canonical model formed by $1/A_d(p)$. As depicted in Figure 5.6, the RIVC involves two stages [110], as explained in the following sections.

5.4.1 Stage I: Initialization

The SRIVC is used for obtaining an initial guess about the estimated parameters θ_e. The SRIVC algorithm involves the following four stages.

1) Designing a Stable Filter: To avoid the problem that arises from obtaining the input and output time derivatives of a CT process, the following state-variable filter is defined:

$$f_c(p)=\frac{1}{(p+\alpha)^{n_d}} \tag{5.22}$$

where α is a positive real number that is usually selected to be equal to or greater than the expected system bandwidth.

2) Obtaining the Regression Vector $\phi_{f_c}(t_k)$: The input and output are filtered using $f_c(p)$ to obtain the regression vector $\phi_{f_c}(t_k)$ from the sampled data.

3) Calculating an Initial Estimate $\hat{\theta}_{e(1)}$: Applying the LS method gives an initial estimate $\hat{\theta}_{e(1)}$ of θ_e based on (5.19), as follows:

$$\hat{\theta}_{e(1)}=\left(\frac{1}{N}\sum_{k=1}^{N}\phi_{f_c}(t_k)\phi_{f_c}^T(t_k)\right)^{-1}\frac{1}{N}\left(\sum_{k=1}^{N}\phi_{f_c}(t_k)\Delta I_{od,f_A}^{(n_d)}(t_k)\right) \tag{5.23}$$

where

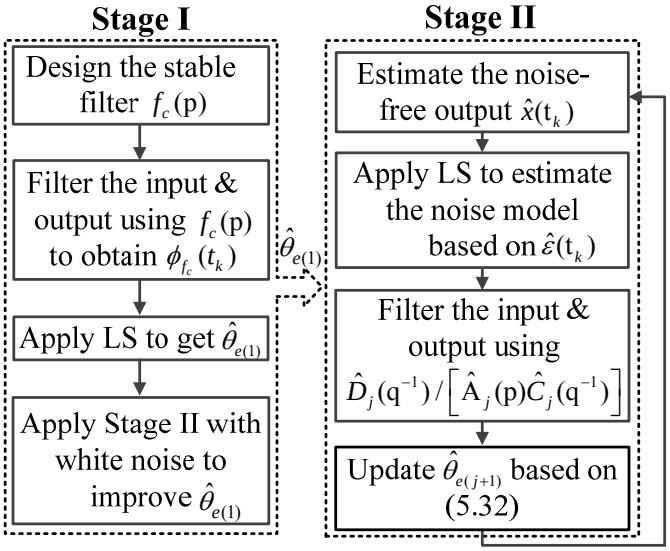

Figure 5.6: Flowchart of the RIVC

$$\Delta I_{od,f_A}^{(n_d)}(t_k)=\frac{p^{n_d}}{\left(p+\alpha\right)^{n_d}}\Delta I_{od}(t_k), \tag{5.24}$$

$$\begin{aligned}\phi_{f_A}(t_k)=\Big[&-\Delta I_{od,f_c}^{(n_d-1)}(t_k),-\Delta I_{od,f_c}^{(n_d-2)}(t_k),\cdots,-\Delta I_{od,f_c}(t_k)\\&\Delta V_{od,f_c}^{(m_1)}(t_k),\Delta V_{od,f_c}^{(m_1-1)}(t_k),\cdots,\Delta V_{od,f_c}(t_k)\\&\Delta I_{oq,f_c}^{(m_2)}(t_k),\Delta I_{oq,f_c}^{(m_2-1)}(t_k),\cdots,\Delta I_{oq,f_c}(t_k)\Big]^T\\=\frac{1}{\left(p+\alpha\right)^{n_d}}\Big[&-p^{n_d-1}\Delta I_{od}(t_k),-p^{n_d-2}\Delta I_{od}(t_k),\cdots,-\Delta I_{od}(t_k),\\&p^{m_1}\Delta V_{od}(t_k),p^{m_1-1}\Delta V_{od}(t_k),\cdots,\Delta V_{od}(t_k),\\&p^{m_2}\Delta I_{oq}(t_k),p^{m_2-1}\Delta I_{oq}(t_k),\cdots,\Delta I_{oq}(t_k)\Big]^T.\end{aligned} \tag{5.25}$$

4) Iteratively Improving the Initial Estimate $\hat{\theta}_{e(1)}$: Stage II (discussed later) is applied, assuming a white noise model, i.e., $\hat{D}(q^{-1})=\hat{C}(q^{-1})=1$, until $\hat{\theta}_{e(1)}$ converges to its true value θ_e. The convergence criterion is defined based on the normalized maximum relative error of the estimated parameters, as given in (5.26).

$$\max_i\left|\frac{\hat{\theta}_{e(j)}(i)-\hat{\theta}_{e(j-1)}(i)}{\hat{\theta}_{e(j)}(i)}\right|<\mu,\qquad\forall i=1,2,\cdots,n_p \tag{5.26}$$

where $\mu \in \Re^+$ is close to zero; j is the iteration index; and n_p is the total number of the estimated parameters: i.e., $n_p = n_d + \sum_{i=1}^{n_u} m_i + n_u$.

5.4.2 Stage II: Iterative Estimation

After the iterative estimation in Stage I converges, $\hat{\theta}_{e(j)}$ is used for initializing Stage II: i.e., $\hat{\theta}_{e(1)} = \hat{\theta}_{e(j)}$, where j represent the iteration index of Stage II. The additive noise $\varepsilon_d(t_k)$, in Stage II, is modeled as a DT autoregressive–moving-average (ARMA) process:

$$\varepsilon_d(t_k) = \frac{C(q^{-1})}{D(q^{-1})} e(t_k) \tag{5.27}$$

where

$$\begin{aligned} C(q^{-1}) &= 1 + \mathrm{c}_1 q^{-1} + \cdots + c_{m_c} q^{-m_c} \\ D(q^{-1}) &= 1 + d_1 q^{-1} + \cdots + d_{m_d} q^{-m_d} \end{aligned} . \tag{5.28}$$

In these calculations, $e(t_k)$ is a DT white noise with variance σ^2 and a zero mean, and q^{-1} is the backward shift operator. The iterative estimation consists of the following four stages, which are repeated until the previously defined convergence criterion is reached.

1) Generating the Estimated Noise-Free Output $\Delta \hat{\mathrm{X}}_{od}(t_k)$*:* In this stage, $\Delta \hat{\mathrm{X}}_{od}(t_k)$ is generated in terms of the estimated polynomials $\hat{A}_{d,j}(p)$, $\hat{B}_{1,j}(p)$, and $\hat{B}_{2,j}(p)$, which are calculated based on $\hat{\theta}_{e(j)}$, as follows:

$$\Delta \hat{\mathrm{X}}_{od}(t_k) = \frac{\hat{B}_{1,j}(p)}{\hat{A}_{d,j}(p)} \Delta V_{od}(t_k) + \frac{\hat{B}_{2,j}(p)}{\hat{A}_{d,j}(p)} \Delta I_{oq}(t_k) . \tag{5.29}$$

2) Estimating the DT Noise Model: First, the estimated additive noise is calculated: $\hat{\varepsilon}_d(t_k) = \Delta I_{od}(t_k) - \Delta \hat{\mathrm{X}}_{od}(t_k)$. The LS method is then applied for the estimation of the ARMA noise model, as given by

$$\hat{\varepsilon}_d(t_k) = \frac{\hat{C}_j(q^{-1})}{\hat{D}_j(q^{-1})} e(t_k) . \tag{5.30}$$

3) Filtering Using $\hat{D}_j(q^{-1})\Big/\Big[\hat{C}_j(q^{-1})\hat{A}_{d,j}(p)\Big]$*:* To obtain the updated estimate $\hat{\theta}_{e(j+1)}$, the input, output, and $\Delta\hat{\mathrm{X}}_{od}$ must be filtered using the estimated CT filter $1\big/\hat{A}_{d,j}(p)$. The resulting signals and their derivatives at t_k are passed through the DT filter $\hat{D}_j(q^{-1})\big/\hat{C}_j(q^{-1})$ to obtain

$$\begin{aligned} Y_f(t_k) &= \Big[\Delta I_{od,f}^{(n_d)}(t_k), \Delta I_{od,f}^{(n_d-1)}(t_k), \cdots, \Delta I_{od,f}(t_k)\Big]^T \\ U_f(t_k) &= \Big[\Delta V_{od,f}^{(m_1)}(t_k), \Delta V_{od,f}^{(m_1-1)}(t_k), \cdots, \Delta V_{od,f}(t_k) \\ &\qquad \Delta I_{oq,f}^{(m_2)}(t_k), \Delta I_{oq,f}^{(m_2-1)}(t_k), \cdots, \Delta I_{oq,f}(t_k)\Big]^T \\ \hat{\mathrm{X}}_f(t_k) &= \Big[\Delta\hat{\mathrm{X}}_{od,f}^{(n_d)}(t_k), \Delta\hat{\mathrm{X}}_{od,f}^{(n_d-1)}(t_k), \cdots, \Delta\hat{\mathrm{X}}_{od,f}(t_k)\Big]^T. \end{aligned} \tag{5.31}$$

4) Updating the Estimated Parameters $\hat{\theta}_{e(j+1)}$*:* The last step is the determination of the updated estimate $\hat{\theta}_{e(j+1)}$:

$$\hat{\theta}_{e(j+1)} = \left(\frac{1}{N}\sum_{k=1}^{N}\hat{\phi}_f(t_k)\phi_f^T(t_k)\right)^{-1}\frac{1}{N}\left(\sum_{k=1}^{N}\hat{\phi}_f(t_k)\Delta I_{od,f}^{(n_d)}(t_k)\right) \tag{5.32}$$

where

$$\Delta I_{od,f}^{(n_d)}(t_k) = \frac{\hat{D}_j(q^{-1})p^{n_d}}{\hat{C}_j(q^{-1})\hat{A}_{d,j}(p)}\Delta I_{od}(t_k) \tag{5.33}$$

$\phi_f(t_k)$, and $\hat{\phi}_f(t_k)$ are defined in (5.34) and (5.35), respectively.

$$\begin{aligned} \phi_f(t_k) &= \Big[-\Delta I_{od,f}^{(n_d-1)}(t_k), -\Delta I_{od,f}^{(n_d-2)}(t_k), \cdots, -\Delta I_{od,f}(t_k), \Delta V_{od,f}^{(m_1)}(t_k), \Delta V_{od,f}^{(m_1-1)}(t_k), \cdots, \Delta V_{od,f}(t_k), \Delta I_{oq,f}^{(m_2)}(t_k), \Delta I_{oq,f}^{(m_2-1)}(t_k), \cdots, \Delta I_{oq,f}(t_k)\Big]^T \\ &= \frac{\hat{D}_j(q^{-1})}{\hat{C}_j(q^{-1})\hat{A}_{d,j}(p)}\Big[-p^{n_d-1}\Delta I_{od}(t_k), -p^{n_d-2}\Delta I_{od}(t_k), \cdots, -\Delta I_{od}(t_k), p^{m_1}\Delta V_{od}(t_k), p^{m_1-1}\Delta V_{od}(t_k), \cdots, \Delta V_{od}(t_k), p^{m_2}\Delta I_{oq}(t_k), p^{m_2-1}\Delta I_{oq}(t_k), \cdots, \Delta I_{oq}(t_k)\Big]^T \end{aligned} \tag{5.34}$$

$$\begin{aligned} \hat{\phi}_f(t_k) &= \Big[-\Delta\hat{X}_{od,f}^{(n_d-1)}(t_k), -\Delta\hat{X}_{od,f}^{(n_d-2)}(t_k), \cdots, -\Delta\hat{X}_{od,f}(t_k), \Delta V_{od,f}^{(m_1)}(t_k), \Delta V_{od,f}^{(m_1-1)}(t_k), \cdots, \Delta V_{od,f}(t_k), \Delta I_{oq,f}^{(m_2)}(t_k), \Delta I_{oq,f}^{(m_2-1)}(t_k), \cdots, \Delta I_{oq,f}(t_k)\Big]^T \\ &= \frac{\hat{D}_j(q^{-1})}{\hat{C}_j(q^{-1})\hat{A}_{d,j}(p)}\Big[-p^{n_d-1}\Delta\hat{X}_{od}(t_k), -p^{n_d-2}\Delta\hat{X}_{od}(t_k), \cdots, -\Delta\hat{X}_{od}(t_k), p^{m_1}\Delta V_{od}(t_k), p^{m_1-1}\Delta V_{od}(t_k), \cdots, \Delta V_{od}(t_k), p^{m_2}\Delta I_{oq}(t_k), p^{m_2-1}\Delta I_{oq}(t_k), \cdots, \Delta I_{oq}(t_k)\Big]^T \end{aligned} \tag{5.35}$$

5.5 Excitation and Model Order Selection

5.5.1 Grid Admittance Excitation

As mentioned previously, grid admittance identification can be classified into two categories: non-invasive and invasive. The non-invasive approach utilizes disturbances that already exist in the networks as a means of estimating grid admittance. However, this approach is marred by imprecision because it fails to guarantee a PE, especially in the case of a high signal-to-noise ratio (SNR). The active grid admittance is also nonlinear, and should thus be linearized around a specific operating point. As depicted in Section 5.3, the resultant linearized model must be represented by a high-order transfer matrix, which is not guaranteed to be dynamically excited by a non-invasive approach. The proposal is therefore for the DG control system to apply two pulse-excitation signals in order to excite the grid dynamics in the $d-q$ frame.

To ensure the convergence of the model parameters to their true values, the applied pulses should be persistently exciting. Sensitivity analysis is therefore conducted for the selection of the best candidate control reference signals over which the pulse-excitation signals are superimposed. The sensitivity analysis represents variations in the DG output currents with respect to the applied excitation signals. To guarantee a PE [111], such variations in the DG output currents must be maximized over a wide range of frequencies. In the study presented in this chapter, to illustrate the proposed sensitivity analysis, two DG control systems are considered: droop-based and dispatchable, as shown in Figure 5.7. The droop-based DG is connected through an LC filter (R_f, L_f, and C_f) to a load represented by a series RL circuit (R_l and L_l). The dispatchable DG is connected to a grid modeled by a voltage source V_g in series with an RL circuit (R_g and L_g). The superimposed excitation signals are applied to the control reference signals and are represented by E_{dq}, as indicated in Figure 5.7. The control reference signals are V_{odq}^{ref}, I_{dq}^{ref}, and V_{dq}^{*} for the droop-based DG and PQ_o^{ref}, I_{dq}^{ref}, and V_{dq}^{*} for the dispatchable DG, where V_{dq}^{*} and PQ_o^{ref} represent the converter reference voltages in the $d-q$ frame and the DG reference active and reactive powers, respectively.

To examine the sensitivity of the DG output currents to the applied excitations, the sensitivity transfer function S_{ij} from a specific input $\Delta E_{(j)}$ to a specific output $\Delta I_{o(i)}$ is derived, using a block diagram reduction, as follows:

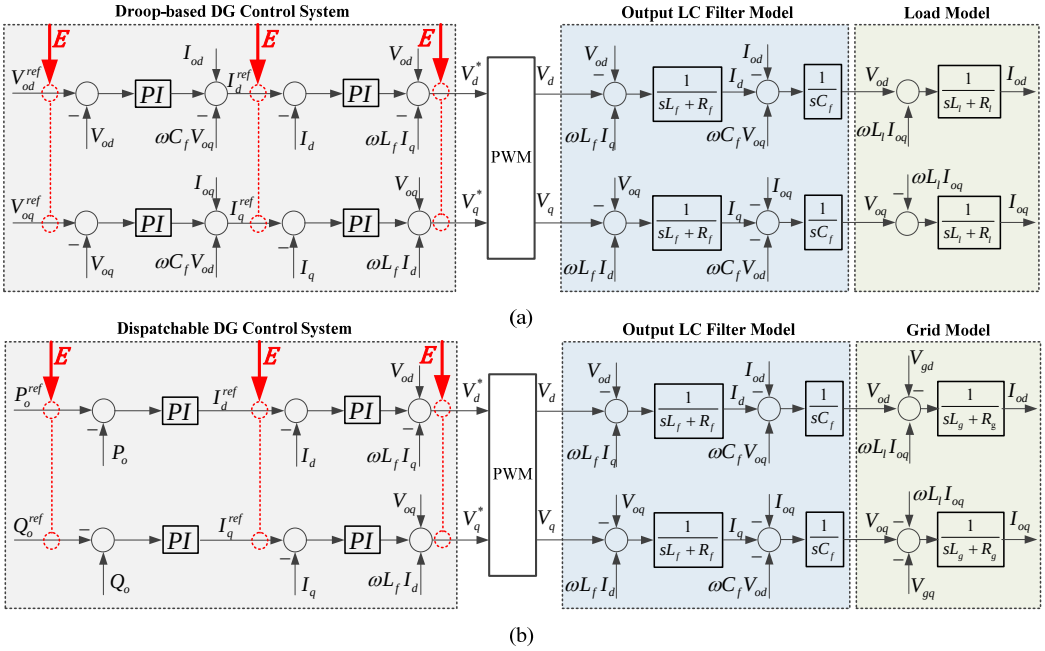

Figure 5.7: DG control systems with invasive grid excitation: (a) droop-based DG connected to an RL load; (b) dispatchable DG connected to a grid

$$S_{ij} = \left.\frac{\Delta I_{o(i)}}{\Delta E_{(j)}}\right|_{\substack{\Delta E_{(k)}=0 \\ k\neq j}} \tag{5.36}$$

$$I_o \in \left\{ I_{od}, I_{oq} \right\}$$

$$E \in \begin{cases} \left\{ V_{od}^{ref}, V_{oq}^{ref}, I_d^{ref}, I_q^{ref}, V_d^*, V_q^* \right\}, & \text{mode1} \\ \left\{ P_o^{ref}, Q_o^{ref}, I_d^{ref}, I_q^{ref}, V_d^*, V_q^* \right\}, & \text{mode2} \end{cases}$$

where mode1 and mode2 denote the droop-based and dispatchable DG controls, respectively. Figure 5.8 provides the magnitude plots of the sensitivity transfer functions in the frequency domain. The higher the transfer function magnitude at a specific excitation $\Delta E_{(j)}$, the more sensitive the DG output current $\Delta I_{o(i)}$ to such an excitation. For example, Figure 5.8(b) indicates the sensitivity of ΔI_{oq} for the droop-based DG at different excitations, as defined by mode1. It is apparent that ΔI_{oq} is more sensitive to the excitation imposed on ΔV_q^*. In both droop-based and dispatchable DGs, I_{od} and I_{oq} are more sensitive to the excitation applied at V_d^* and V_q^*, respectively. This effect is attributable to the relatively higher gains of the sensitivity transfer functions, from V_{dq}^* to I_{odq}, over a

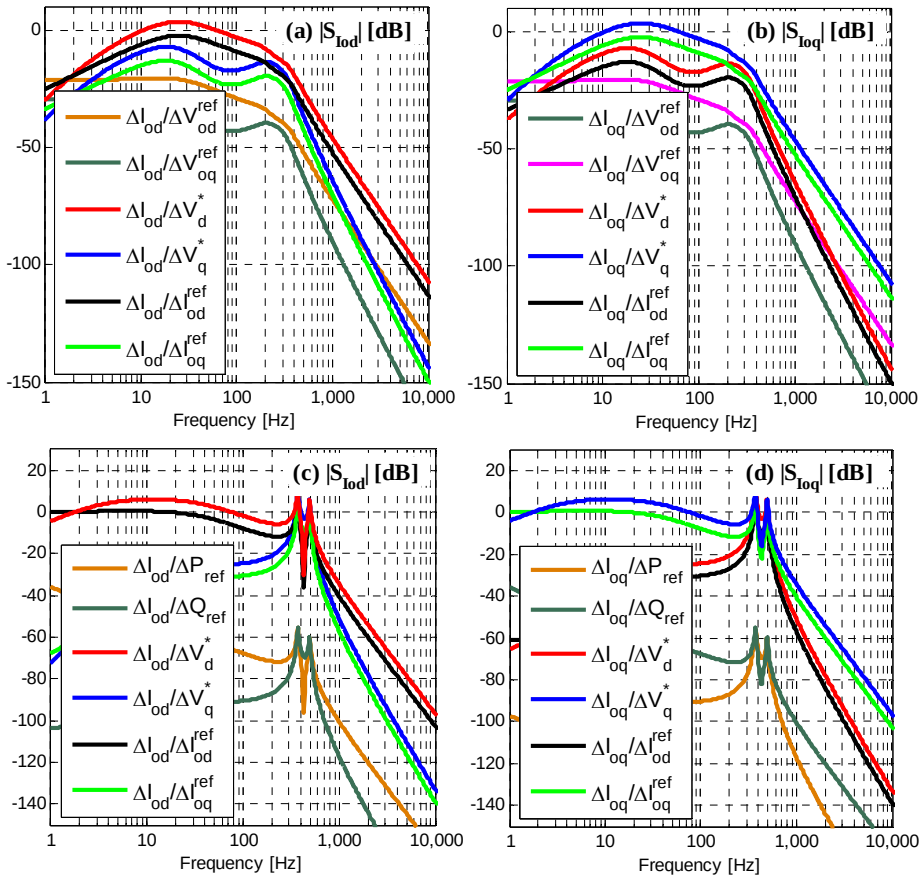

Figure 5.8: Sensitivity of DG output currents to variant excitations: (a &b) droop-based DG, (c & d) dispatchable DG

wide frequency spectrum. This result is therefore as expected because the application of the excitation signals at the converter reference signals avoids control loop filtration. Such an application can thus ensure better PE than with other candidate control reference signals and also avoids any alteration of the steady state operating point.

The excitation voltage pulses E_{dq} are characterized by their magnitude A_E and width T_E, as can be seen in Figure 5.9(a). To avoid any alteration of the operating condition, the magnitude A_E is limited: $A_E \leq 5\%$. To reduce the settling time of the DG output currents and for better representation of an impulse disturbance that has a rich frequency domain spectrum, the pulse width T_E should be very small. On the other hand, when T_E is extremely small, the excited grid dynamics may become indistinguishable. To illustrate this trade-off, the RIVC algorithm is employed for the estimation of the passive grid admittance shown in Figure 5.3(a). Figure 5.9(b) demonstrates the effect on the

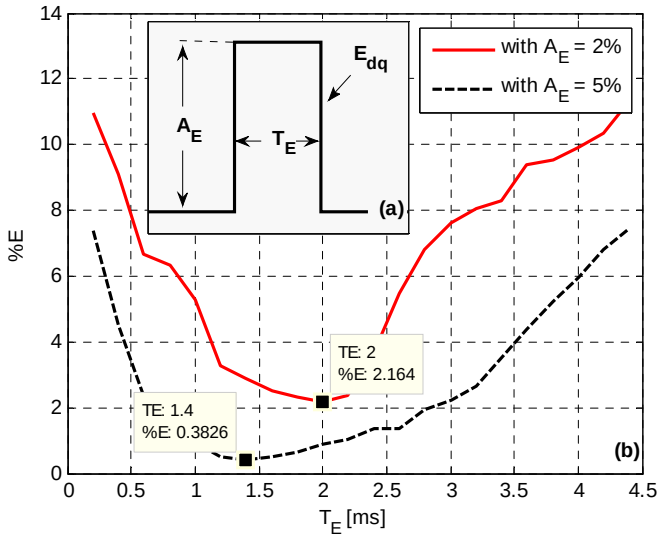

Figure 5.9: Effect of the pulse characteristics on the estimation error

estimation error when T_E is varied at different values of A_E. The figure shows the trade-off between increasing and decreasing T_E. At a specific A_E, an optimal value of T_E results in the minimization of the estimation error. Increasing A_E can reduce the estimation error; however, it should be limited in order to reduce stress on the system. In this study, A_E is adjusted at 5% and T_E is set at 1.4 ms. To avoid unnecessary grid excitations, the DG operation can be divided into different zones, each with pre-specified voltage and current thresholds. Whenever the operating zone changes, E_{dq} is applied for the estimation of the grid admittance. Alternatively, a voltage disturbance can be applied periodically in order to update the grid admittance information [55], [112].

5.5.2 Adaptive Model Order Selection

Prior to the identification process, the model structure, i.e., n_d, n_q, and $m_1, \cdots, m_4$, must be precisely selected to fit the sampled data and to avoid over-parameterization. Identification of the model structure involves calculating two statistical measures for a range of model orders: the coefficient of determination (R_T^2) and Young's information criterion (YIC), which are defined as follows [105], [113]:

$$R_T^2 = 1 - \frac{\hat{\sigma}^2}{\hat{\sigma}_y^2} \tag{5.37}$$

$$YIC = Log_e\left\{\frac{\hat{\sigma}^2}{\hat{\sigma}_y^2}\right\} + Log_e\frac{1}{n_p}\sum_{i=1}^{n_p}\frac{p_{ii}}{\hat{\theta}_i^2} \tag{5.38}$$

where $\hat{\sigma}^2$ is the variance of the model residuals; $\hat{\sigma}_y^2$ is the variance of the output signal; and p_{ii} is the i^{th} diagonal element of the estimated parametric error covariance matrix P_{cov}, which is calculated based on the last iteration of the RIVC algorithm and is given by

$$P_{\text{cov}} = \hat{\sigma}^2\left[\sum_{k=1}^{N}\hat{\phi}_f(t_k)\hat{\phi}_f^T(t_k)\right]^{-1}. \tag{5.39}$$

The coefficient of determination R_T^2 is a normalized measure of how well the model and system output values match. The closer R_T^2 is to unity, the better; however, this measure is insufficient for avoiding over-parameterization [105] and should thus be combined with YIC. The first YIC term reflects the accuracy of the model with respect to fitting the data. The more negative the value of the term becomes, the smaller the model's residuals. On the other hand, the second YIC term provides a measure of how the error covariance matrix P_{cov} is conditioned. In the case of over-parameterised models, the instrumental product matrix (IPM), i.e., $\sum_{k=1}^{N}\hat{\phi}_f(t_k)\hat{\phi}_f^T(t_k)$, tends toward singularity, resulting in a highly increased value of p_{ii}. In such cases, the second YIC term will dominate the first term, indicating over-parameterization.

Due to the time-varying nature of the active grid admittance, the proposed identification method should provide adaptive model order selection. This chapter proposes an adaptive model order selection algorithm capable of dealing with active admittance uncertainties: load variations and grid reconfigurations. Figure 5.10 shows the proposed adaptive model order selection for active grid admittance identification, where ΔT represents the algorithm update time. The grid is initially excited using E_{dq}. The dc components of the DG output voltages and currents are then eliminated in order to estimate the grid admittance at a specific operating condition. The previously used (or initially assumed) model structure is employed for fitting the estimated admittance model. The change in YIC at a specific identification cycle (h) is calculated as

$$\Delta YIC(h) = \frac{YIC(h) - YIC(h-1)}{YIC(h-1)} \times 100. \tag{5.40}$$

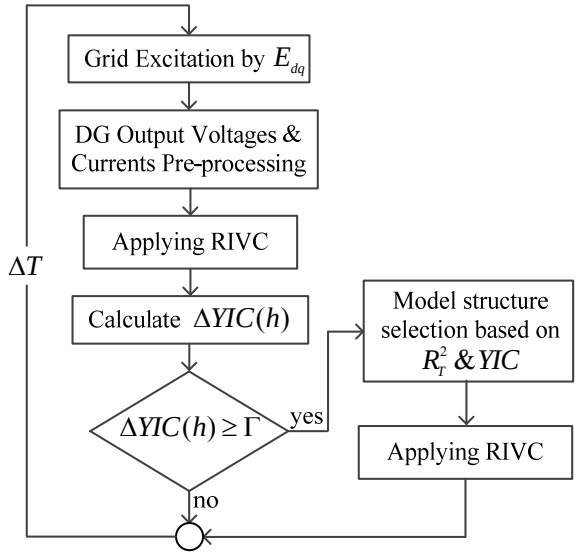

Figure 5.10: The schematic diagram of the proposed model order selection

Table 5.1: Best Candidate Models Ranked by YIC

(a)				(b)			
n_d	m_1, m_2	YIC	R_T^2	n_q	m_3, m_4	YIC	R_T^2
3	3 3	-14.4	0.999	3	3 3	-11.8	0.997
4	4 1	-12.5	0.999	2	1 3	-11.7	0.970
3	3 1	-10.4	0.996	4	3 4	-10.6	0.997
1	2 1	-9.8	0.996	3	4 4	-10.3	0.997
3	4 3	-9.7	0.999	4	1 3	-10.1	0.980

When $\Delta YIC(h)$ is greater than a specific threshold Γ (i.e., 5 %), indicating a variation in the admittance structure, the model order is reselected from different candidate models based on R_T^2 and YIC. Increasing the number of candidate models can lead to a more representative model structure, but with a greater computational burden. Without loss of generality, the noise model order is assumed to be fixed without any adaptation because it is independent of the system dynamics. However, the CT model order is assumed to vary from first order, representing passive grids, to fourth order, representing active grids. For example, the best model orders that can fit the active grid admittance shown in Figure 5.3(b) are listed in Table 5.1, sorted by best YIC. The best model has the highest negative YIC value and a relatively high R_T^2 value, as indicated in the shaded row of Table 5.1. As

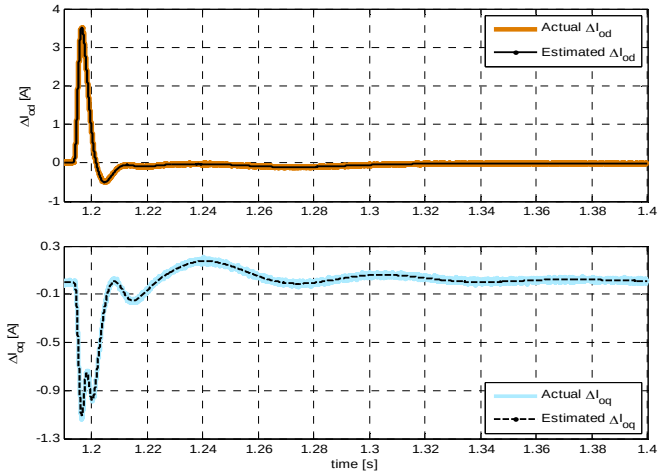

Figure 5.11: Estimation of DG output currents for active grid case, using the proposed algorithm.

shown in Figure 5.11, when the model order structure is selected based on R_T^2 and *YIC* measures, applying the RIVC algorithm to identify the grid admittance model can result in an accurate match between actual and estimated DG output currents.

5.6 Real-Time Validation

This section describes case studies that were conducted as a means of testing the robustness and effectiveness of the proposed multivariable grid admittance identification algorithm. The test networks are illustrated in Figure 5.12, and were tested in real time using OPAL RTS. The network parameters are given in Appendix A.

Two OPAL RTS were employed for conducting the HiL application [75], [89], which was used for validating the DG controller that integrates the proposed identification, as illustrated in Figure 5.13. The DG controller was emulated using RTS1, producing a RCP and exchanges real-time data with the virtual network modeled in RTS2. It is worth mentioning that modeling both the DG controller and the virtual network using the same RTS results in a setup categorization as a SiL application. Detailed switching models were used for representing actual converter behavior. OPAL RTS is able to provide high-frequency sampling of IGBTs because of its (field-programmable-gate-array) FPGA interface and interpolating function blocks that compensate for inter-step events arising during the sampling time. For the purposes of this study, although PWM signals permit a resolution down to 10 ns, the RTS models were run with a fixed-step sampling time of 50 μs. The test system was built using Simulink/SimPowerSystems along with blocksets provided by ARTEMiS [86]. To

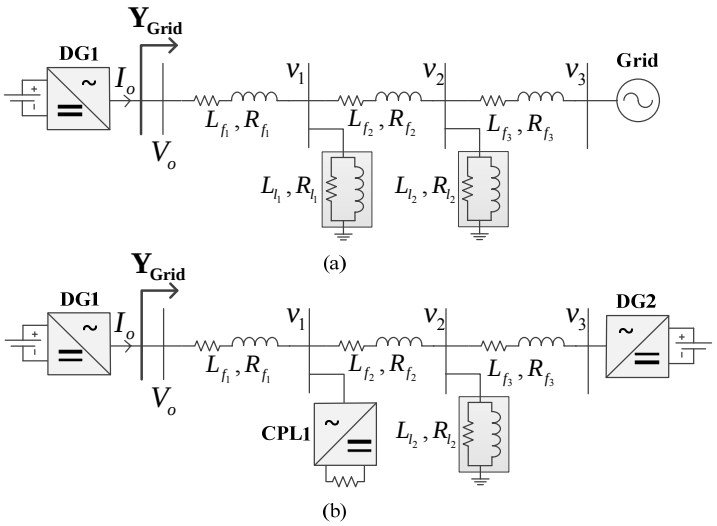

Figure 5.12: Test networks: (a) passive admittance model, (b) active admittance model

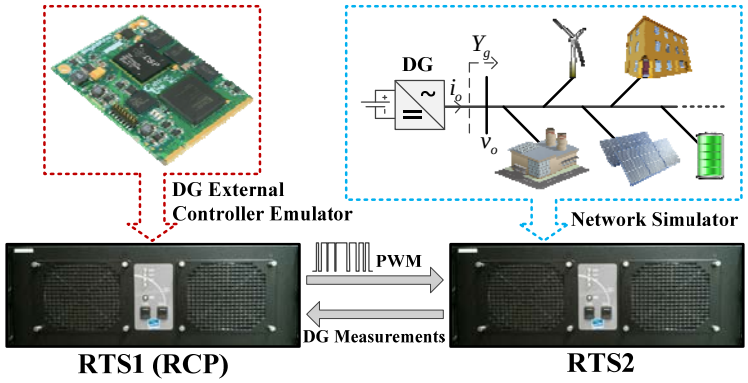

Figure 5.13: The hardware-in-the-loop setup

test the validity of the proposed online estimation algorithm, the following case studies were conducted.

5.6.1 Passive Grid Admittance Identification

Figure 5.12(a) depicts a passive grid admittance model from the perspective of DG1, which represents a dispatchable DG with the control system shown in Figure 5.7(b). The initial excitation voltage pulses E_{dq} are applied at $t = 1.0$ s and are superimposed on the converter reference voltages V_{dq}^{*} in order to ensure a PE. The resultant changes in the DG output voltages and currents, ΔI_{odq} and ΔV_{odq}, are acquired during T_N, where T_N represents the settling time of ΔI_{odq}, as indicated in

Figure 5.14(b). It should be noted that T_N is a system-dependent parameter because it signifies the system response to the applied excitation. The proposed identification algorithm is then applied in order to estimate the grid admittance, where t_h denotes the estimation time. As illustrated by (5.7) and (5.8), ΔV_{od} and ΔI_{oq} are used for estimating ΔI_{od}, resulting in G_1 and G_2. On the other hand, ΔV_{oq} and ΔI_{od} are employed for estimating ΔI_{oq}, resulting in G_3 and G_4. Figure 5.14(a) reveals the accuracy of the proposed algorithm when estimating grid resistance and inductance: R_g and L_g, respectively. The corresponding estimated DG output currents, in contrast to the actual DG output currents, are shown in Figure 5.14(b). This figure also provides details related to the algorithm update time: $\Delta T = T_N + t_h$, which starts at $t = 1.0$ s and ends at $t = 1.04$ s.

The performance of the proposed method relative to that of the identification algorithm presented in [63] is demonstrated by the results shown in Figure 5.14(c) and Figure 5.14(d). The method suggested in [63] employs an extended Kalman filter (EKF) to estimate only passive grid admittance. The proposed algorithm can reduce the total estimation error from 6.26 % to 0.245 %. This improvement is attributable to two factors: 1) the proposed algorithm iteratively updates the estimated parameters; 2) as reported in [63], [114], the tuning of the EKF parameters is complex. From a time response perspective, the proposed algorithm can update the passive grid admittance in 40 ms, which is approximately equivalent to the settling time required by the EKF method. These results confirm the ability of the proposed identification algorithm to estimate passive grid admittance with a high degree of accuracy.

To investigate the effect of the PE on the accuracy of the estimation, E_{dq} is applied at 1) DG reference powers PQ_o^{ref}, 2) DG reference currents I_{dq}^{ref}, and 3) DG converter reference voltages V_{dq}^*. Figure 5.15 indicates the percentage error in both R_g and L_g for different grid admittance excitations. The application of E_{dq} at V_{dq}^* improves estimation accuracy, which corresponds with the rationale for the sensitivity analysis presented in Section 5.5.

5.6.2 Active Grid Admittance Identification

To test the success of the proposed algorithm with respect to estimating active grid admittance, as shown in Figure 5.12(b), E_{dq} is applied at $t = 1.0$ s. Following the procedures explained previously, ΔI_{odq} and ΔV_{odq} are acquired during T_N. To obtain G_1, G_2, G_3, and G_4, the proposed algorithm is

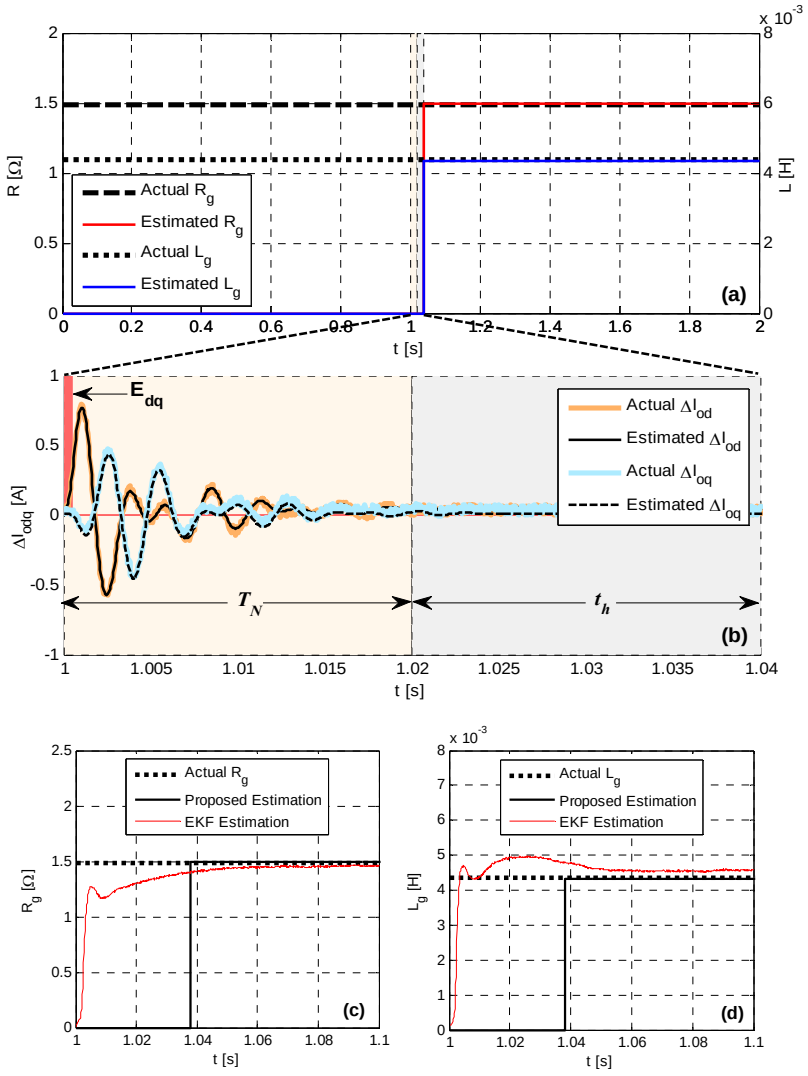

Figure 5.14: The response of the proposed identification algorithm for passive networks

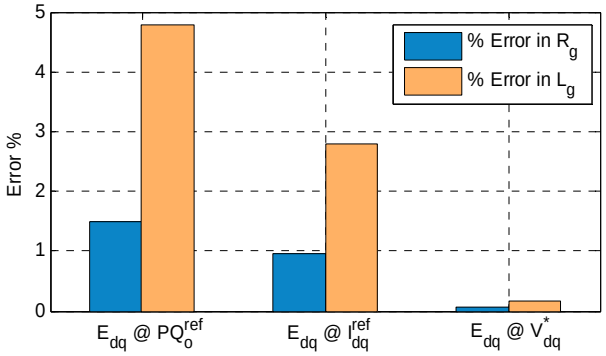

Figure 5.15: Percentage estimation error for different excitations

then applied for estimating the DG output currents, as shown in Figure 5.16. It is worth mentioning that, in this case, the update time ΔT is 80 ms. Again, Figure 5.16(a) confirms that the first-order model for $G_1, G_2, G_3,$ and G_4 fails to represent the dynamics of the excited grid admittance. However, the proposed active grid admittance modeling results in an accurate match between the actual and estimated DG output currents, as indicated in Figure 5.16(b).

To test the success of the proposed algorithm, its comparative performance was evaluated using the frequency sweep estimation method proposed in [59]. This method injects an unbalanced line-to-line current between two lines of the ac system in order to acquire the grid impedance model in the $d-q$ frame, as illustrated in Appendix C.

Figure 5.17 reveals the success of the proposed algorithm in estimating the grid admittance dynamics in the frequency domain. Based on [59], seven logarithmically spaced injected frequencies per decade are used for sweeping the grid admittance, with a total computational time of 1.2 min. The relation between the computational time of the proposed algorithm and model order is illustrated in Figure 5.18. The computational time increases for higher-order models. In contrast with the results obtained by [59], the fourth-order model employed in the proposed identification requires about 30 ms to estimate grid admittance. The proposed algorithm is thus able to provide an accurate estimate of grid admittance as well as: 1) a parametric admittance CT model, which is more suitable for online adaptive control; 2) no necessity for additional hardware; and 3) significantly reduced computational time because the application of FFT is no longer needed at each injected frequency.

5.6.3 Effect of Grid Condition

To test the robustness of the proposed algorithm, its performance was examined with respect to weak and stiff grid conditions. The feeder parameters of the test networks shown in Figure 5.12 were adapted to represent a variety of grid conditions. To emulate a weaker grid, the feeder impedances were increased by 50 %, while a 50 % decrease in the feeder impedances was employed to exemplify a stiffer grid. Figure 5.19 indicates the response of the proposed algorithm in the case of stiff and weak grids. The proposed algorithm is able to estimate grid admittance with a high level of accuracy for a variety of grid conditions. With respect to passive grid admittance, the root-mean-square error (RMSE) in the estimated ΔI_{odq} varies from 0.21 %, to 0.34 %, to 0.83 %, for weak, nominal, and stiff grid conditions, respectively. A similar RMSE pattern, i.e., 0.32 %, 0.47 %, and 0.92 %, can also be observed in the case of active grid admittance. This slight error increase can be explained by the fact

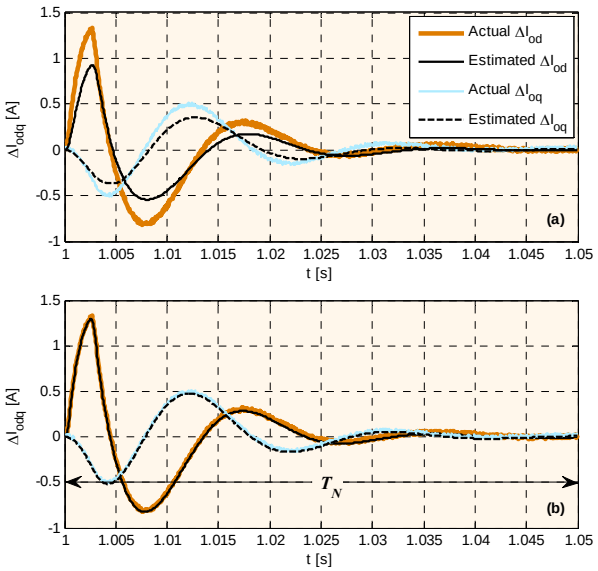

Figure 5.16: Estimation of DG output currents based on: (a) a passive grid model, (b) an active grid model

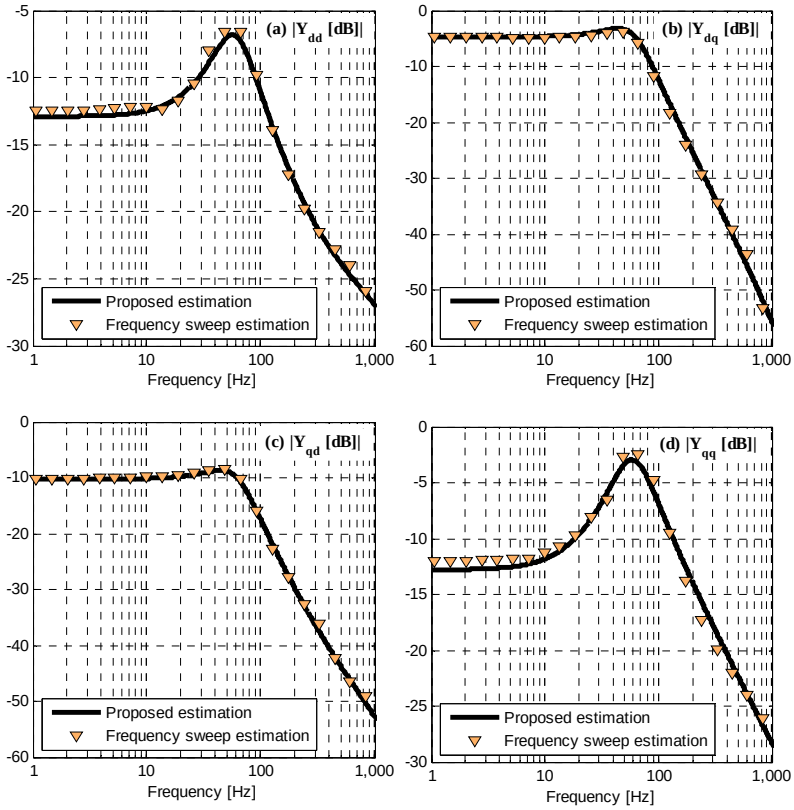

Figure 5.17: Verification of the estimated active grid admittance in the frequency domain

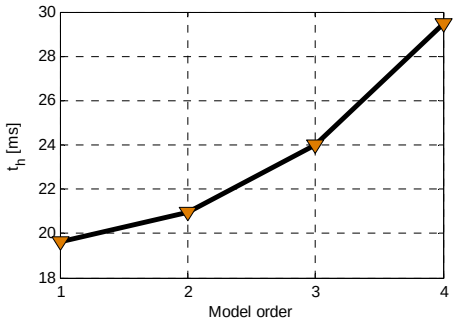

Figure 5.18: Computational time for different model orders

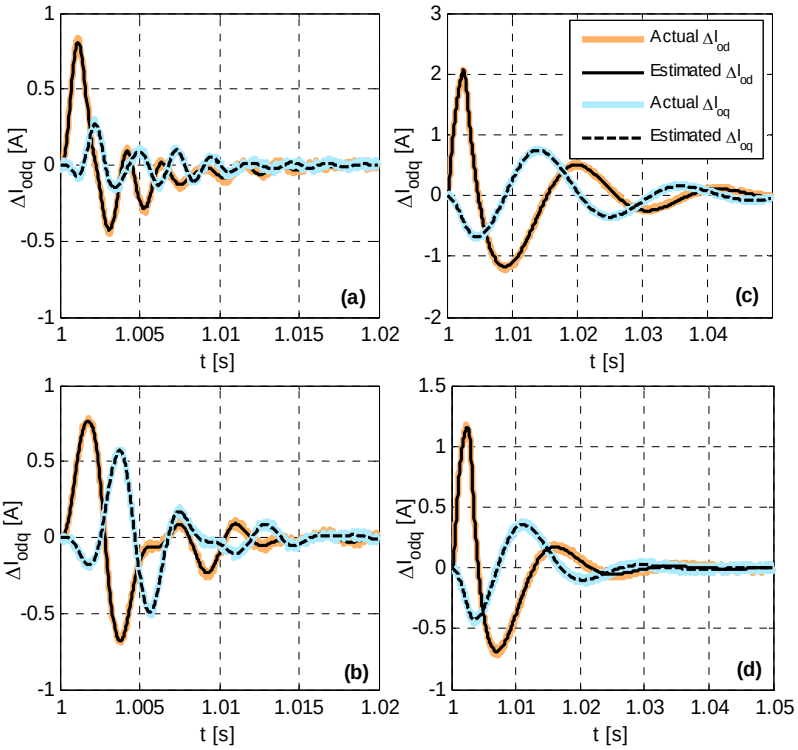

Figure 5.19: Response to a variety of grid conditions: (a) stiff grid with passive admittance; (b) weak grid with passive admittance; (c) stiff grid with active admittance; (d) weak grid with active admittance.

that the sensitivity of the DG output currents to the applied excitation is reduced slightly when the network impedance decreases.

5.7 Discussion

Grid admittance is an essential parameter for impedance stabilization. In this chapter, a novel identification algorithm is proposed for online grid admittance estimation. The differences between passive and active grid admittance models have also been illustrated. Active grid admittance arises

from a high penetration of DGs and nonlinear loads, which alters the conventional passive nature of grid admittance to an active one. The proposed online estimator can be added as an ancillary function within the DSP controller of inverter-based DGs, and the proposed RIVC can be employed for multivariable grid admittance identification. Due to the time-varying and nonlinear nature of active grid admittance, an online adaptive model order selection algorithm is proposed. The proposed model order selection provides accurate selection of the best model structure without over-parameterization. Real-time simulations using an HiL application and OPAL RTS were performed in order to test the effectiveness of the proposed algorithm in ADNs. The results confirm the accuracy and convergence of the proposed identification method for estimating both passive and active grid admittances without additional hardware requirements.

Chapter 6
Multivariable DG Impedance Modeling and Adaptive Reshaping

6.1 Introduction

In Chapter 5, the effect of grid impedance variations on system stability was illustrated using two scenarios (PQ- and droop-based DGs). It was shown that systems dominated by inverter-based DGs and loads are prone to negative impedance instability due to tight power regulation [20]. Increased grid inductance may also lead to unstable DG performance. In order to assess impedance stability and design appropriate DG adaptive controllers, two multivariable models are required: grid and DG impedance models. In Chapter 5, a new grid admittance (impedance) identification algorithm was proposed that took into account the nature of both passive and active grid admittance.

By estimating grid impedance, DG output impedance can be reshaped according to impedance stability criteria to maintain system stability and improve dynamic performance. This chapter proposes a new DG output impedance reshaping algorithm, in the presence of grid impedance variations and time-varying DG operating points. These are dispatched by the proposed SCL algorithms proposed in Chapters 3 and 4. The proposed control scheme is applicable in both grid-connected (PQ-based) and islanded (droop-based) DGs. The DG multivariable output impedances are derived in the $d-q$ domain and validated using the frequency sweep impedance estimation method with chirp excitation [115].

The DG controller parameters are optimally tuned based on impedance stability criteria, which are formulated using the derived DG impedance models and the estimated grid impedance. The optimization problem is solved offline and aims to maximize the system bandwidth and damping. The solutions provided by the optimization stage, at wide ranges of grid impedances and operating conditions, are employed to train a proposed neural network (NN)-based adaptation scheme which updates controller parameters online. The final element described in this chapter is the real-time validation of the proposed DG control algorithm in both grid-connected and islanded modes using OPAL RTS with an HiL application.

The rest of this chapter is organized as follows. Section 6.2 explains DG output impedance modeling and validation using the frequency sweep method. Section 6.3 discusses the proposed DG impedance reshaping algorithm that involves optimal tuning and adaptive gain scheduling. Validation results and conclusions are presented in Section 6.4 and Section 6.5, respectively.

6.2 Proposed DG Multivariable Impedance Modeling and Validation

The impedance stability criterion, first proposed by Middlebrook [49], divides the system under study into interconnected DG source and grid subsystems. For VSCs, the characteristic equation $\Phi(s)$ of that interconnected system can be given as follows [51]:

$$\Phi(s) = \mathcal{I} + Z_{DG}(s)Y_{Grid}(s) \tag{6.1}$$

where $\mathcal{I}$ is the identity matrix of size 2, $Z_{DG}(s)$ is the DG impedance matrix, and $Y_{Grid}(s)$ is the grid admittance matrix. Both $Z_{DG}(s)$ and $Y_{Grid}(s)$ are 2×2 matrices modeled in the $d-q$ frame. Stability can be guaranteed if the ratio of DG output impedance to grid impedance satisfies the Nyquist stability criterion, i.e., $Z_{DG}Y_{Grid}$ should not encircle the $(-1,0)$ point on the Nyquist plot. The above stability criterion is applicable with droop-based DGs that are typically employed in the islanded mode of operation, because the DG in this case operates in the voltage control mode emulating a slack bus. In [51], a generalized impedance stability criterion is proposed for grid-connected DGs that are typically controlled in the current injection mode, i.e., current-controlled VSC. In such a case, the characteristic equation $\Phi(s)$ is given by

$$\Phi(s) = \mathcal{I} + Z_{Grid}(s)Y_{DG}(s) \tag{6.2}$$

where $Z_{Grid}(s)$ is the grid impedance matrix and $Y_{DG}(s)$ is the DG admittance matrix. Consequently, the impedance stability criterion is dependent on the ratio of grid impedance to DG impedance. From (6.1) and (6.2), it can be observed that the stability requirements of droop-based DGs (voltage-controlled VSC) are opposite to that of PQ-based DGs (current-controlled VSC). For better impedance stability measures, voltage sources should have low (ideally zero) output impedances, while current sources should show high (ideally infinite) output impedances. In order to formulate the impedance stability criteria defined by (6.1) and (6.2), the DG and grid impedances should be known. The grid impedance parameters can be estimated using the identification algorithm proposed in Chapter 5. In this section, multivariable DG impedance models are derived for both grid-connected and islanded modes of operation [116].

6.2.1 Impedance Modeling of Grid-Connected DGs

Figure 6.1 indicates the block diagram of a grid-connected DG controlled to inject dispatchable active and reactive powers, i.e., PQ-based DG. The DG inverter model in the $d-q$ synchronous frame represents the dynamics of the interfacing LC filter [19], and is given by (2.1) – (2.4). The instantaneous active (p_o) and reactive (q_o) powers can be calculated in terms of the measured output voltages and currents at the PCC, as given by (2.14) and (2.15). Then, p_o and q_o can be filtered using a low-pass filter (LPF) G_f with a cut-off frequency ω_p to obtain the average active (P_o) and reactive (Q_o) powers. These correspond to the fundamental component

$$P_o = G_f\, p_o \tag{6.3}$$

$$Q_o = G_f\, q_o \tag{6.4}$$

where

$$G_f = \frac{\omega_p}{s+\omega_p}. \tag{6.5}$$

Typically a PLL derives V_{oq} to zero, and thus the small-signal representation of P_o and Q_o can be given by

$$\Delta P_o = 1.5 G_f \left(\mathrm{V}_{od}^{o}\, \Delta \mathrm{I}_{od} + \mathrm{I}_{od}^{o}\, \Delta V_{od} + \mathrm{I}_{oq}^{o}\, \Delta V_{oq} \right) \tag{6.6}$$

$$\Delta Q_o = 1.5 G_f \left(\mathrm{I}_{od}^{o}\, \Delta V_{oq} - \mathrm{V}_{od}^{o}\, \Delta \mathrm{I}_{oq} - \mathrm{I}_{oq}^{o}\, \Delta V_{od} \right) \tag{6.7}$$

Furthermore, the small-signal representation of the voltage cross-decoupling terms can be derived as

$$\Delta\left(\omega C_f V_{oq}\right) = \omega_o C_f \Delta V_{oq} \tag{6.8}$$

$$\Delta\left(\omega C_f V_{od}\right) = \omega_o C_f \Delta V_{od} + C_f V_{od}^{o} \Delta\omega \tag{6.9}$$

In (6.9), the change in the system frequency $\Delta\omega$ can be denoted in terms of ΔV_{oq}, using the PLL dynamic model PLL [24], i.e.,

$$\Delta\omega = G_{pll} G_{vf} \Delta V_{oq} \tag{6.10}$$

where G_{pll} is the PLL controller (i.e., $G_{pll} = K_{pll,p} + K_{pll,\mathrm{i}} / s$), and G_{vf} is the voltage LPF of PLL (i.e., $G_{vf} = \omega_v / (\mathrm{s}+\omega_v)$). Hence, (6.9) can be rewritten as

$$\Delta\left(\omega C_f V_{od}\right) = \omega_o C_f \Delta V_{od} + C_f G_{pll} G_{vf} V_{od}^{o} \Delta V_{oq} \tag{6.11}$$

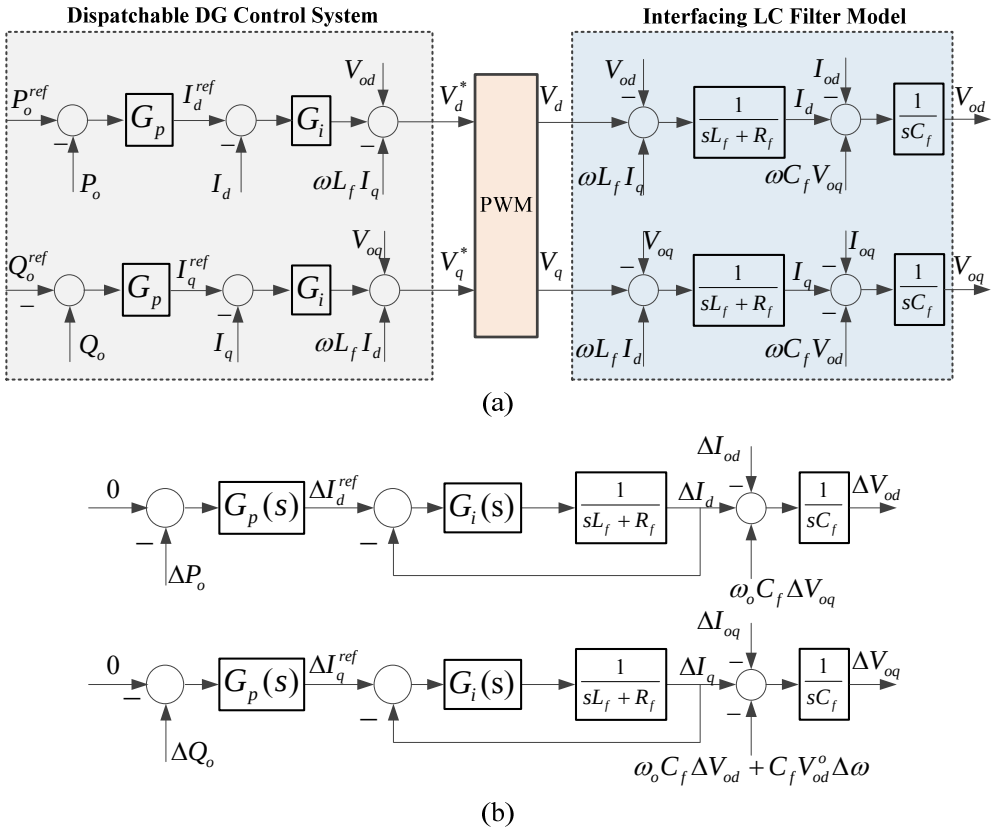

Figure 6.1: Grid-connected DG control system: (a) large signal model; (b) small-signal model

The small-signal block diagram representation of the PQ-based DG model can then be created as depicted in Figure 6.1(b). The block diagram is constructed based on neglecting the inverter-switching dynamics, which can be represented by a half-sample time delay, because the control dynamics are much slower than the switching dynamics [18]. This assumption is well accepted. Moreover, it will be shown that the proposed impedance model can mimic the exact dynamics of an actual inverter. By using (6.8) and (6.11) to simplify the small-signal block diagram, the dynamics of the $d-q$ control loops can be expressed as

$$sC_f\Delta V_{od} = -\underbrace{\left(\frac{G_iG_p}{R_f+sL_f+G_i}\right)}_{G_{ip}}\Delta P_o - \Delta I_{od} + \omega_o C_f \Delta V_{oq} \tag{6.12}$$

$$sC_f\Delta V_{oq} = G_{ip}\Delta Q_o - \Delta I_{oq} - \omega_o C_f \Delta V_{od} - C_f G_{pll} G_{vf} V_{od}^o \Delta V_{oq} \tag{6.13}$$

where G_p is the DG power controller (i.e., $G_p = K_{pp} + K_{pi}/s$), and G_i is the DG current controller (i.e., $G_i = K_{ip} + K_{ii}/s$). By substituting (6.6) and (6.7) in (6.12) and (6.13), the $d-q$ control loops can be expressed only by the DG output voltage and current, as follows:

$$\varphi_1 \Delta V_{od} + \varphi_2 \Delta V_{oq} = \gamma_1 \Delta I_{od} + \gamma_1 \Delta I_{oq} \tag{6.14}$$

$$\varphi_3 \Delta V_{od} + \varphi_4 \Delta V_{oq} = \gamma_3 \Delta I_{od} + \gamma_4 \Delta I_{oq} \tag{6.15}$$

where

$$\begin{cases} \varphi_1 = sC_f + 1.5 G_{ip} G_f I_{od}^o \\ \varphi_2 = -\omega_o C_f + 1.5 G_{ip} G_f I_{oq}^o \\ \varphi_3 = \omega_o C_f + 1.5 G_{ip} G_f I_{oq}^o \\ \varphi_4 = sC_f - 1.5 G_{ip} G_f I_{od}^o + C_f G_{pll} G_{vf} V_{od}^o \end{cases}, \quad \begin{cases} \gamma_1 = -1 - 1.5 G_{ip} G_f V_{od}^o \\ \gamma_2 = 0 \\ \gamma_3 = 0 \\ \gamma_4 = \gamma_1 \end{cases} \tag{6.16}$$

Hence, the multivariable DG output impedance model for PQ-based DGs, i.e., $Z_{\mathrm{DG,PQ}}$, can be given by

$$Z_{\mathrm{DG,PQ}} = \begin{bmatrix} Z_{dd}(s) & Z_{dq}(s) \\ Z_{qd}(s) & Z_{qq}(s) \end{bmatrix} = -\begin{bmatrix} \varphi_1 & \varphi_2 \\ \varphi_3 & \varphi_4 \end{bmatrix}^{-1} \begin{bmatrix} \gamma_1 & \gamma_2 \\ \gamma_3 & \gamma_4 \end{bmatrix} \tag{6.17}$$

6.2.2 Impedance Modeling of Droop-based DGs

The DG output impedance for droop-based DGs can be derived by following the same procedure explained above. Figure 6.2(a) denotes the droop-based DG control system that compromises two cascade control loops, namely, current and voltage loops. By substituting (6.6) and (6.7) in (2.17) and (2.18), ΔV_{od}^{ref} and $\Delta\omega$ can be derived as

$$\Delta V_{od}^{ref} = a_1 \Delta I_{oq} + a_2 \Delta V_{od} + a_3 \Delta V_{oq} \tag{6.18}$$

$$\begin{aligned} \Delta\omega &= -m\Delta P \\ &= -1.5 m G_f \left(\mathrm{V}_{od}^o \, \Delta \mathrm{I}_{od} + \mathrm{I}_{od}^o \, \Delta V_{od} + \mathrm{I}_{oq}^o \, \Delta V_{oq} \right) \end{aligned} \tag{6.19}$$

where

$$\begin{cases} a_1 = 1.5 n G_f V_{od}^o \\ a_2 = 1.5 n G_f I_{oq}^o \\ a_3 = -1.5 n G_f I_{od}^o \end{cases} \tag{6.20}$$

Using (6.19), $\Delta\left(\omega C_f V_{od}\right)$ can be derived as

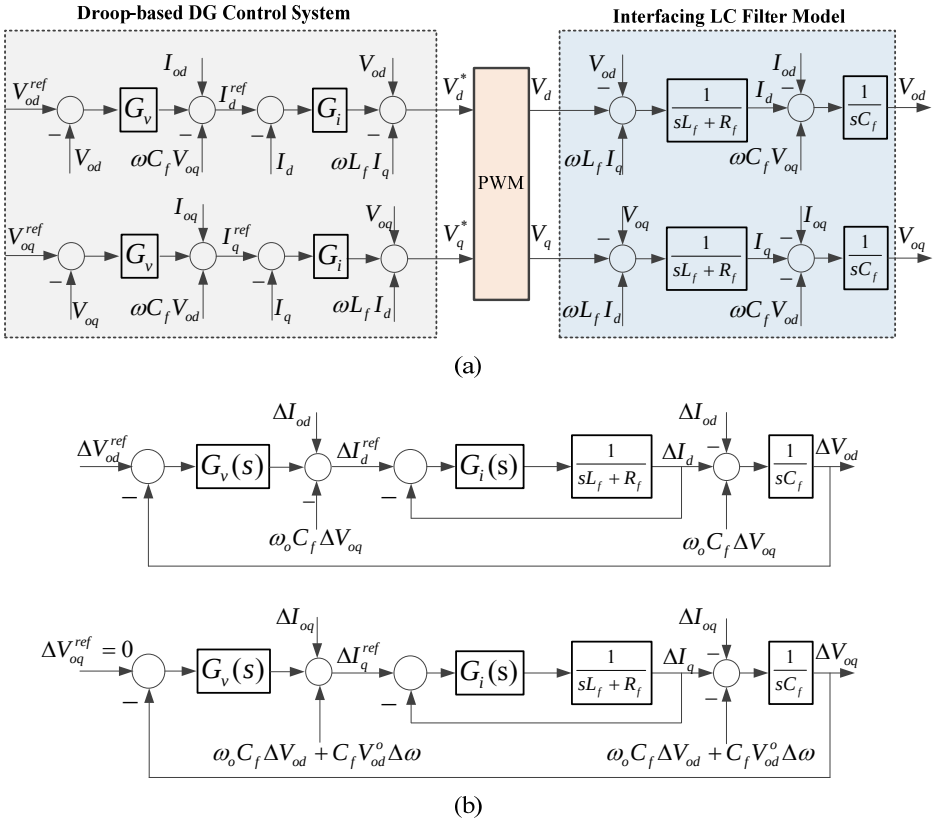

Figure 6.2: Droop-based DG control system: (a) large signal model; (b) small-signal model

$$\begin{aligned}\Delta\left(\omega C_f V_{od}\right) &= \omega_o C_f \Delta V_{od} + C_f V_{od}^o \Delta\omega \\ &= b_1 \Delta I_{od} + b_2 \Delta V_{od} + b_3 \Delta V_{oq}\end{aligned} \tag{6.21}$$

with

$$\begin{cases} b_1 = -1.5 m C_f G_f \left(V_{od}^o\right)^2 \\ b_2 = \omega_o C_f - 1.5 m C_f G_f V_{od}^o I_{od}^o \\ b_3 = -1.5 m C_f G_f V_{od}^o I_{oq}^o \end{cases} \tag{6.22}$$

Simplifying the block diagrams shown in Figure 6.2(b) using (6.18) and (6.21), the dynamics of the $d-q$ control loops can be modeled only in terms of the DG output voltage and current, as follows:

$$\alpha_1 \Delta V_{od} + \alpha_2 \Delta V_{oq} = \beta_1 \Delta I_{od} + \beta_2 \Delta I_{oq} \tag{6.23}$$

$$\alpha_3 \Delta V_{od} + \alpha_4 \Delta V_{oq} = \beta_3 \Delta I_{od} + \beta_4 \Delta I_{oq} \tag{6.24}$$

where

$$\begin{cases} \alpha_1 = sC_f + (1-a_2)G_v G_I^{cl} \\ \alpha_2 = (\omega_o C_f - a_3 G_v) G_I^{cl} - \omega^o C_f \\ \alpha_3 = b_2 (1 - G_I^{cl}) \\ \alpha_4 = sC_f + (G_v - b_3) G_I^{cl} + b_3 \end{cases}, \quad \begin{cases} \beta_1 = G_I^{cl} - 1 \\ \beta_2 = a_1 G_v G_I^{cl} \\ \beta_3 = b_1 (G_I^{cl} - 1) \\ \beta_4 = \beta_1 \end{cases} \tag{6.25}$$

where G_v represents the DG voltage controller (i.e., $G_v = K_{vp} + K_{vi}/s$), and G_I^{cl} is the transfer function of the DG current loop and is given by

$$G_I^{cl} = \frac{G_i}{R_f + sL_f + G_i} \tag{6.26}$$

By arranging (6.23) and (6.24) in a matrix form, the multivariable DG output impedance model for droop-based DGs, i.e., $Z_{DG,droop}$, can be calculated by

$$Z_{DG,droop} = -\begin{bmatrix} \alpha_1 & \alpha_2 \\ \alpha_3 & \alpha_4 \end{bmatrix}^{-1} \begin{bmatrix} \beta_1 & \beta_2 \\ \beta_3 & \beta_4 \end{bmatrix} \tag{6.27}$$

6.2.3 DG Impedance Model Verifications

In order to verify the derived multivariable impedance models, the frequency sweep impedance estimation method with a chirp excitation is employed [115]. A chirp signal can be a swept-cosine signal with a time-varying instantaneous frequency. In this study, a linear chirp excitation is used, and the perturbation signal is thus given by

$$\tilde{e} = E_m \cos\left(2\pi \left[f_o + (f_1 - f_o)t / 2T \right] t\right) \tag{6.28}$$

The linear chirp signal $\tilde{e}$ can approximate the spectrum properties of band-limited white noise, and can represent a voltage or current perturbation applied at the DG terminal. The main advantages of the chirp signal over band-limited white noise are: 1) the peak of the noise is approximately twice the chirp signal, which increases the cost of the injection circuit, and 2) the operating point to be measured is less disturbed with smaller peak injections.

Two voltage or current perturbations are needed to estimate the transfer matrix of the DG impedance or admittance. As shown in Figure 6.3(a), two voltage perturbations are employed in PQ-based DGs because the DG is controlled in the current injection mode, where IMU refers to the impedance measurement unit developed by [115]. Alternatively, two current perturbations are

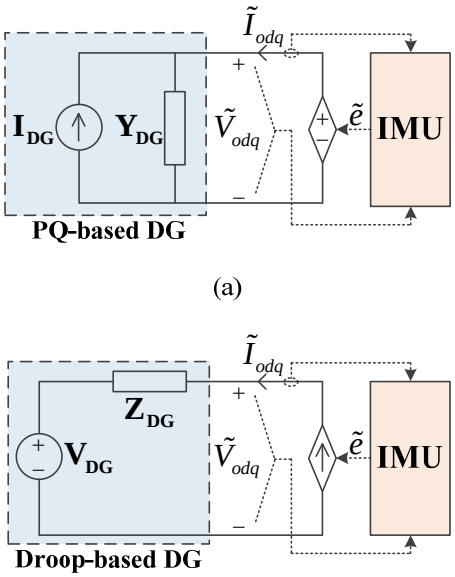

Figure 6.3: DG impedance/admittance measurement setup: (a) PQ-based case; (b) droop-based case

injected at the droop-based DG terminals, since it operates in the voltage control mode, as shown in Figure 6.3(b). In the case of PQ-based DG, the first voltage perturbation can be made by only injecting $\tilde{V}_{od1}$ and setting $\tilde{V}_{oq1}$ to zero. The opposite case is implemented in the second voltage perturbation (i.e., $\tilde{V}_{od2}$ is set to zero while injecting $\tilde{V}_{oq2}$). The resultant current responses are acquired to form:

$$\begin{bmatrix} \tilde{I}_{od1} \\ \tilde{I}_{oq1} \end{bmatrix} = \begin{bmatrix} Y_{dd} & Y_{dq} \\ Y_{qd} & Y_{qq} \end{bmatrix} \begin{bmatrix} \tilde{V}_{od1} \\ 0 \end{bmatrix} \tag{6.29}$$

$$\begin{bmatrix} \tilde{I}_{od2} \\ \tilde{I}_{oq2} \end{bmatrix} = \begin{bmatrix} Y_{dd} & Y_{dq} \\ Y_{qd} & Y_{qq} \end{bmatrix} \begin{bmatrix} 0 \\ \tilde{V}_{od2} \end{bmatrix} \tag{6.30}$$

After acquiring the perturbed DG voltages and currents, DFT is applied to obtain their corresponding spectra. The admittance matrix of the PQ-based DG can then be calculated by combining (6.29) and (6.30):

$$\mathrm{Y}_{\mathrm{DG,PQ}} = \begin{bmatrix} Y_{dd} & Y_{dq} \\ Y_{qd} & Y_{qq} \end{bmatrix} = \begin{bmatrix} \tilde{I}_{od1}(\mathrm{s}) & \tilde{I}_{od2}(\mathrm{s}) \\ \tilde{I}_{oq1}(\mathrm{s}) & \tilde{I}_{oq2}(\mathrm{s}) \end{bmatrix} \begin{bmatrix} \tilde{V}_{od1}(\mathrm{s}) & 0 \\ 0 & \tilde{V}_{oq2}(\mathrm{s}) \end{bmatrix}^{-1} \tag{6.31}$$

Likewise, by injecting two decoupled current perturbations at the droop-based DG terminals, its impedance matrix can be estimated:

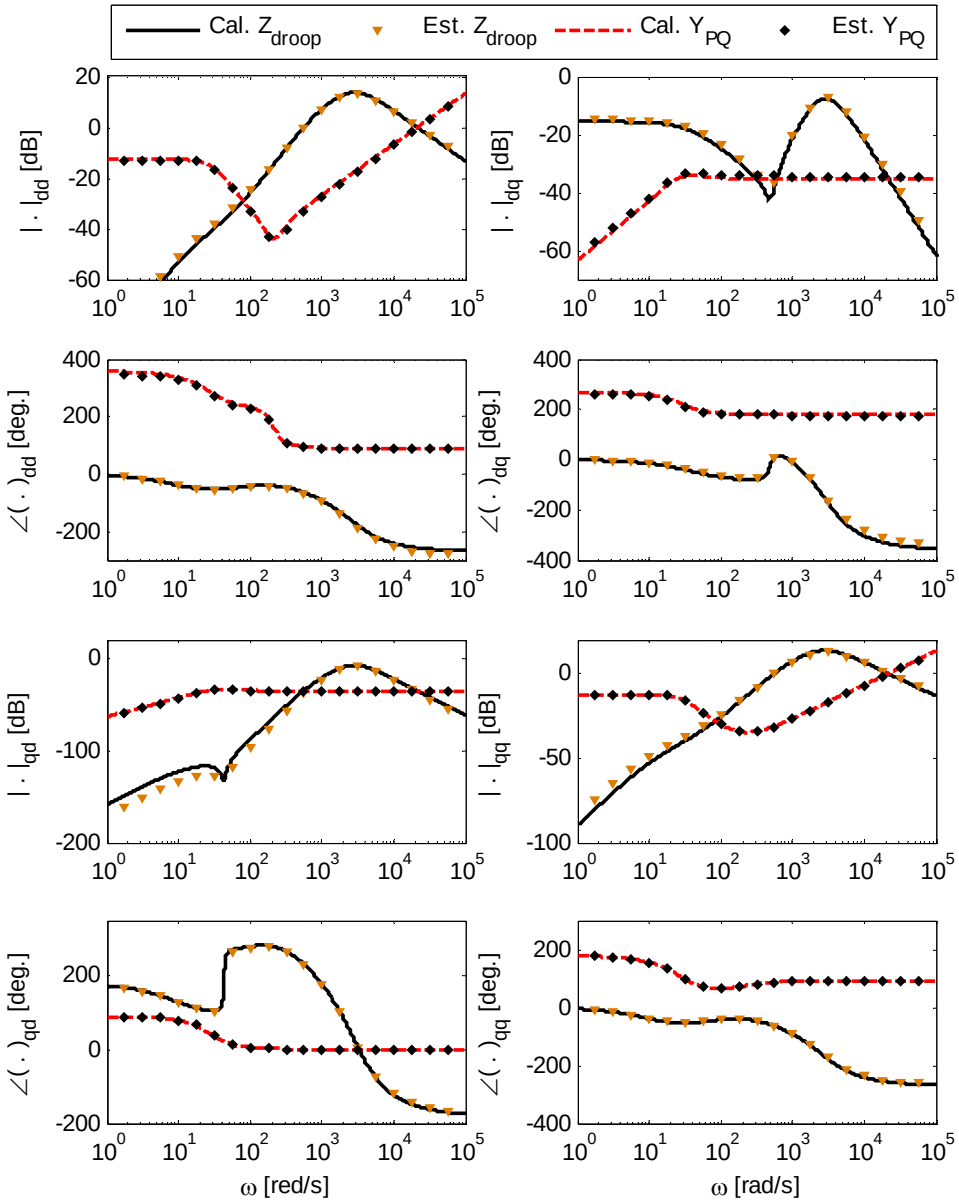

Figure 6.4: DG impedance/admittance model validation

$$Z_{\text{DG,droop}} = \begin{bmatrix} Z_{dd} & Z_{dq} \\ Z_{qd} & Z_{qq} \end{bmatrix} = \begin{bmatrix} \tilde{V}_{od1}(s) & \tilde{V}_{od2}(s) \\ \tilde{V}_{oq1}(s) & \tilde{V}_{oq2}(s) \end{bmatrix} \begin{bmatrix} \tilde{I}_{od1}(s) & 0 \\ 0 & \tilde{I}_{oq2}(s) \end{bmatrix}^{-1} \tag{6.32}$$

Figure 6.4 illustrates the frequency spectrum of the estimated and calculated transfer matrices of the PQ-based DG admittance and the droop-based DG impedance. As depicted in the figure, both of the estimated and calculated impedances (or admittances) are matched, which confirms the accuracy of the proposed multivariable DG impedance modeling. Those multivariable DG output impedance

models can now be combined with the estimated grid impedance model to assess system stability and to design DG adaptive controllers.

6.3 Proposed DG Impedance Adaptive Reshaping

Tuning DG controller gains is a challenging task, since one set of the controller gain may lead to instability issues when grid impedance or DG operating conditions changes. The conventional tuning methods either adjust the control gains based on a tedious trial and error method, or utilize the pole placement technique, which ignores the grid impedance. Thus, DG controller gains should be adaptively tuned to mitigate time-varying grid impedance and DG operating conditions. This section illustrates an optimal DG output impedance reshaping algorithm that can be adaptively implemented to achieve high bandwidth and damped performance.

6.3.1 Optimal DG Controller Tuning

Considering the impedance stability criteria defined by (6.1) and (6.2), a new control algorithm can be proposed to optimally reshape the DG output impedance. The main goal of the proposed optimal control design is to maximize the system bandwidth and improve the system damping. Therefore, two objective functions can be formulated, as follows:

$$\min_{K} F_1(\mathrm{K}) = \hat{\sigma} \tag{6.33}$$

$$\max_{K} F_2(\mathrm{K}) = \hat{\xi} \tag{6.34}$$

subject to

$$K_L \le K \le K_U \tag{6.35}$$

where $\hat{\sigma}$ and $\hat{\xi}$ are the real part and damping ratio of the dominant eigenvalue, i.e., the closest eigenvalue to $j\omega-$axis in the s-plane, respectively; and K is the vector that contains the DG control parameters and is bounded by the lower and upper boundaries K_L and K_U, respectively.

From the characteristic equation $\Phi(\mathrm{s})$, the eigenvalues of the system, i.e., $\Lambda = \mathrm{zeros}\left[\Phi(\mathrm{s})\right]$, can be calculated, and thus $\hat{\sigma}$ can be determined by

$$\hat{\sigma} = \max(\Sigma) \tag{6.36}$$

where

$$\Sigma = \left\{\sigma_i, \sigma_i = \mathrm{Re}\left(\lambda_i\right)\right\}, \quad \lambda_i \in \Lambda \tag{6.37}$$

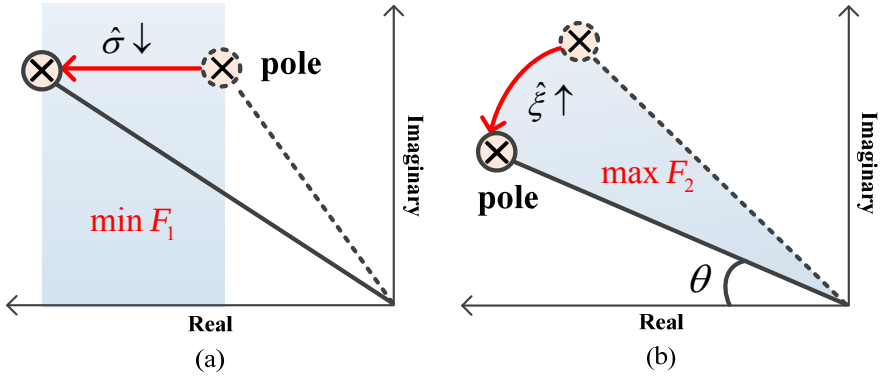

Figure 6.5: Effects of the objective functions: (a) minimizing $\hat{\sigma}$, i.e., maximizing the system bandwidth; (b) maximizing the system damping

The damping ratio $\hat{\xi}$ can be also calculated as

$$\hat{\xi} = \left| \frac{\mathrm{Re}(\lambda_i)}{\lambda_i} \right|_{\mathrm{Re}(\lambda_i)=\hat{\sigma}} \tag{6.38}$$

The gain vector K is dependent on the DG control topology, i.e.,

$$K = \begin{cases} \left[K_{pp}, K_{pi}, K_{ip}, K_{ii}, K_{pll,p}, K_{pll,i} \right] & , \quad \text{mode1} \\ \left[K_{vp}, K_{vi}, K_{ip}, K_{ii} \right] & , \quad \text{mode2} \end{cases} \tag{6.39}$$

where mode1 and mode2 denote grid-connected and droop-based DG control topologies, respectively. Figure 6.5 shows the realization of the above two objectives on the s-plane. The first objective tries to shift the system dominant pole to the left-hand side, thus increasing system bandwidth and improving system relative stability. The second objective attempts to minimize angle θ to increase system damping, thus decreasing the overshoot.

One common approach for handling the two objectives defined in (6.33) and (6.34) is simply to combine them using a weighted-sum method. The weight coefficients can critically affect the optimal solution, since F_1 and F_2 have different units and ranges. In addition, the range of variations for both functions is unknown in order to have a proper normalization. To alleviate the drawback of the weighted-sum approach, the ε-constraint method is employed [117]. The main advantage of this method is that it can identify a Pareto-optimal region regardless of whether the objective space is convex, non-convex, or discrete. The ε-constraint method solves the problem considering one of the objectives while limiting the remaining objectives within specific bounds. Thus, the optimal DG control tuning can be formulated as

$$\min_{K} F_1(\mathrm{K}) = \hat{\sigma} \tag{6.40}$$

subject to

$$G(\mathrm{K}) = \mathrm{F}_2(\mathrm{K}) - \varepsilon > 0 \tag{6.41}$$

$$K_L \le K \le K_U \tag{6.42}$$

where objective F_2 becomes a soft constraint bounded by a pre-defined value of ε. In this study, ε is considered to limit the damping ratio to a value less than that maximally obtained from the Pareto front.

6.3.2 NN-based Gain Scheduling

The previously discussed optimal DG gain tuning is valid at a certain operating point and specific grid impedance. Thus, the optimal gains obtained from the previous step need to be updated when system operating conditions or grid impedance change. To avoid the computational time of the optimization stage, the DG control gains are optimally tuned offline at a wide spectrum of operating conditions and passive grid impedances. A proposed NN-based adaptation scheme is then trained offline using the optimal gain sets obtained from the optimization stage. After training the proposed NN-based adaptation scheme, it can be used online to update DG control gains.

Figure 6.6 shows the proposed NN-based gain scheduling scheme for both grid-connected and droop-based DG control systems. The inputs of the NN-based gain scheduling algorithm are the estimated grid impedance parameters (i.e., R_g and L_g) and the DG output voltage and current (which represent the operating condition), while the outputs are the optimal DG controllers' gains. Whenever a change in either grid impedance or DG operating conditions occurs, the NN-based algorithm adapts the DG control gains online by providing the optimal gain vector K.

It is worth mentioning that the previously proposed NN-based adaptation scheme can be considered an artificially intelligent gain-scheduling adaptive control method. It has the advantage of being simple and not introducing additional nonlinearity to the DG control system since it does not include a feedback adaptation of the estimated parameters. However, when the grid impedance is active, i.e., when it is dominated by nonlinear DG and load impedances, the NN-based adaptation scheme becomes inapplicable because it is only trained assuming a passive characteristic for the grid impedance. In such a case, the optimization stage should be implemented periodically and online, taking into account the estimated active grid impedance model provided by the proposed RIVC grid

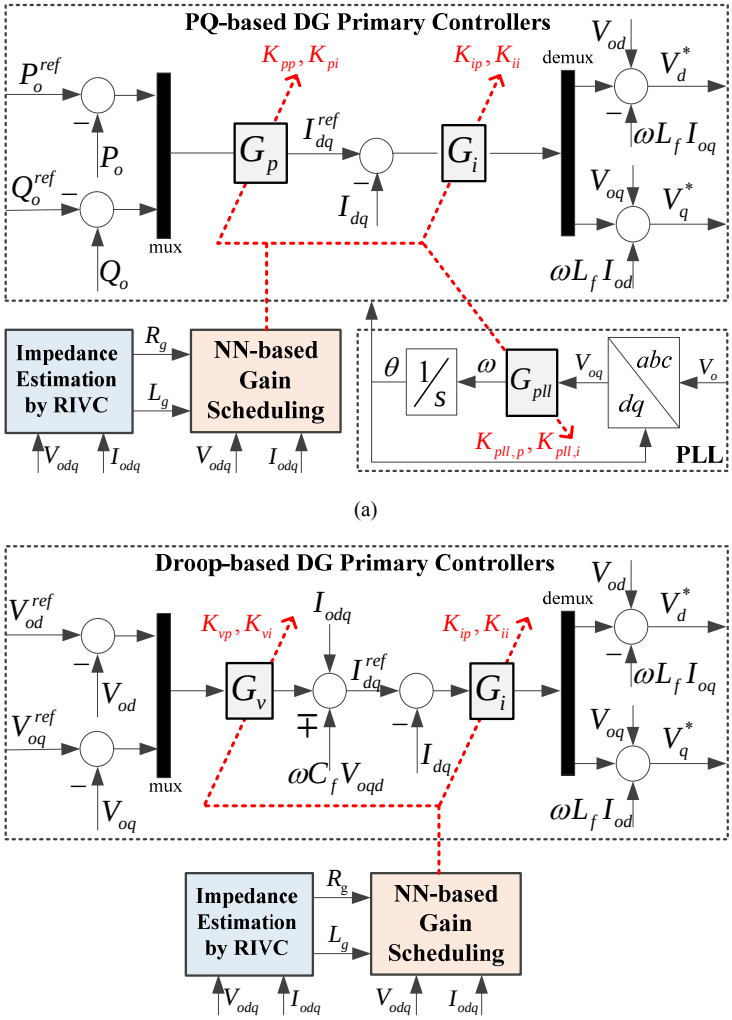

Figure 6.6: Schematic diagram of the proposed optimal adaptive DG control: (a) grid-connected DG; (b) droop-based DG

impedance identification algorithm. The solution of the optimization stage can then be used to update the DG controller gains.

6.4 Real-Time Validation

This section describes case studies that were conducted as a means of testing the robustness and effectiveness of the proposed DG output impedance reshaping algorithm. The test systems are illustrated in Figure 6.7 and were tested in real time using OPAL RTS. Two OPAL RTS were employed for conducting the HiL application [75], [89], which was used for validating the DG controller that integrates the proposed control algorithm, as illustrated in Figure 5.13. The DG

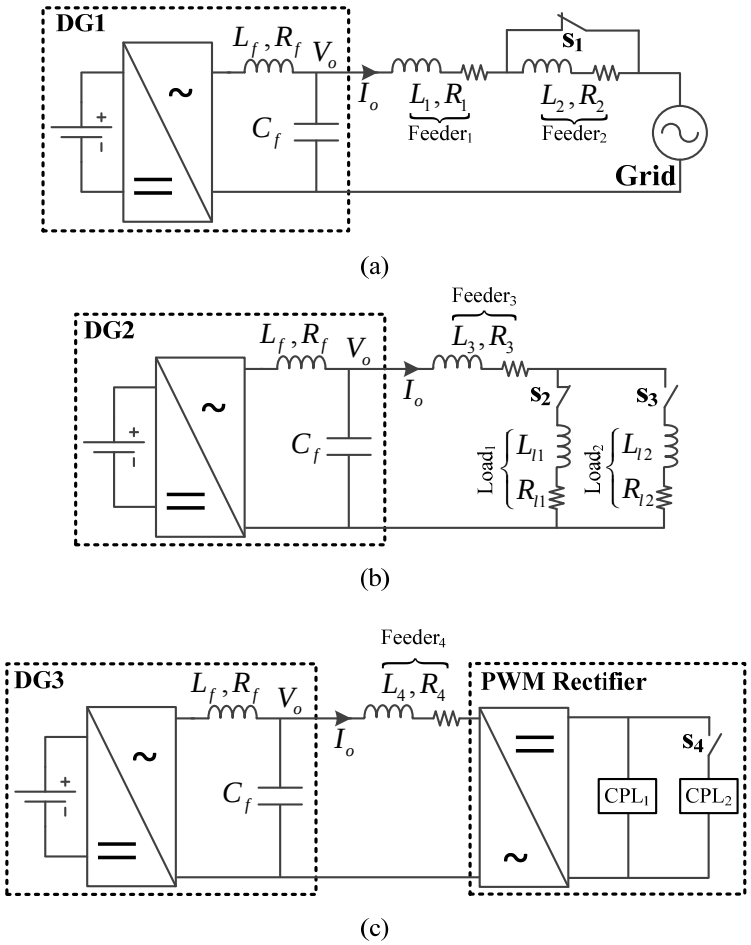

Figure 6.7: Test networks: (a) grid-connected DG, (b) droop-based DG with passive loads, (c) droop-based DG with CPL

controller was emulated using RTS1, imitating a RCP and exchanges of real-time data with the virtual network modeled in RTS2. The test networks' parameters are given in Appendix A. To test the validity of the proposed control algorithm, the following case studies were conducted.

6.4.1 Performance Evaluation of Grid-connected DGs

The test system shown in Figure 6.7(a) represents a DG connected to grid, through Feeder1 and Feeder2. The optimized controller parameters are $K = \left[K_{pp}, K_{pi}, K_{ip}, K_{ii}, K_{pll,p}, K_{pll,i} \right]$. Figure 6.8 shows the dominant eigenvalues of the test system when the DG controller parameters are conventionally and optimally designed. In this study, the damping ratio constraint ε is selected to be equal to 0.9. The proposed DG impedance reshaping algorithm can increase the system bandwidth by

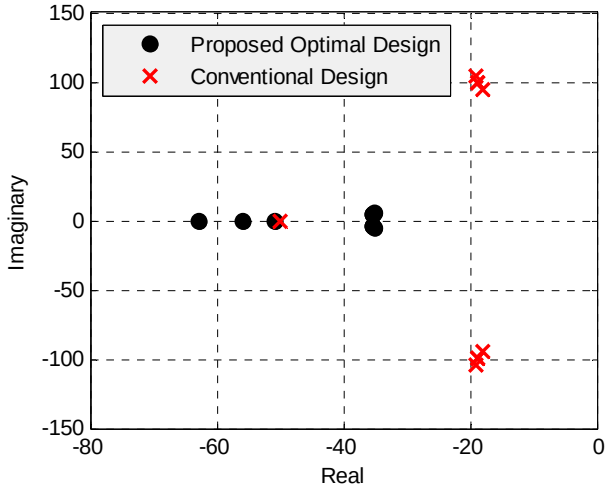

Figure 6.8: Dominant eigenvalues with and without the proposed algorithm, PQ-based DG, nominal grid condition

shifting the dominant pole towards the left hand side of the s-plane. In addition, the damping ratio of the optimized control system is improved significantly compared with the conventionally designed DG control system.

To test the robustness of the proposed control algorithm, real-time simulations are carried out at two different grid impedance conditions. The switch s_1 is normally closed, simulating a nominal grid condition, while the transition to a higher grid inductance condition is achieved by opening s_1 to insert Feeder 2. Figure 6.9(a) and Figure 6.9(b) indicate the performance of the grid-connected DG at the nominal grid impedance condition, created by closing s_1. In this case, the active and reactive power references are increased by 25% at $t = 1.0$ s. The proposed control algorithm can result in a shorter settling time, indicating higher bandwidth, and can lead to a more damped performance compared to conventional control design.

The proposed algorithm is then tested for the case of higher grid inductance condition, formed by opening s_1. The DG conventional control design results in a more oscillatory performance in contrast to the nominal grid impedance condition, as illustrated in Figure 6.9(c) and Figure 6.9(d). As reported in [73], this result is anticipated because the system stability margin decreases when the grid impedance becomes more inductive. The proposed control algorithm shows a more robust performance against the increase in the grid inductance, with faster settling time and higher damping. These results confirm the robustness and effectiveness of the proposed control algorithm when applied with grid-connected DGs.

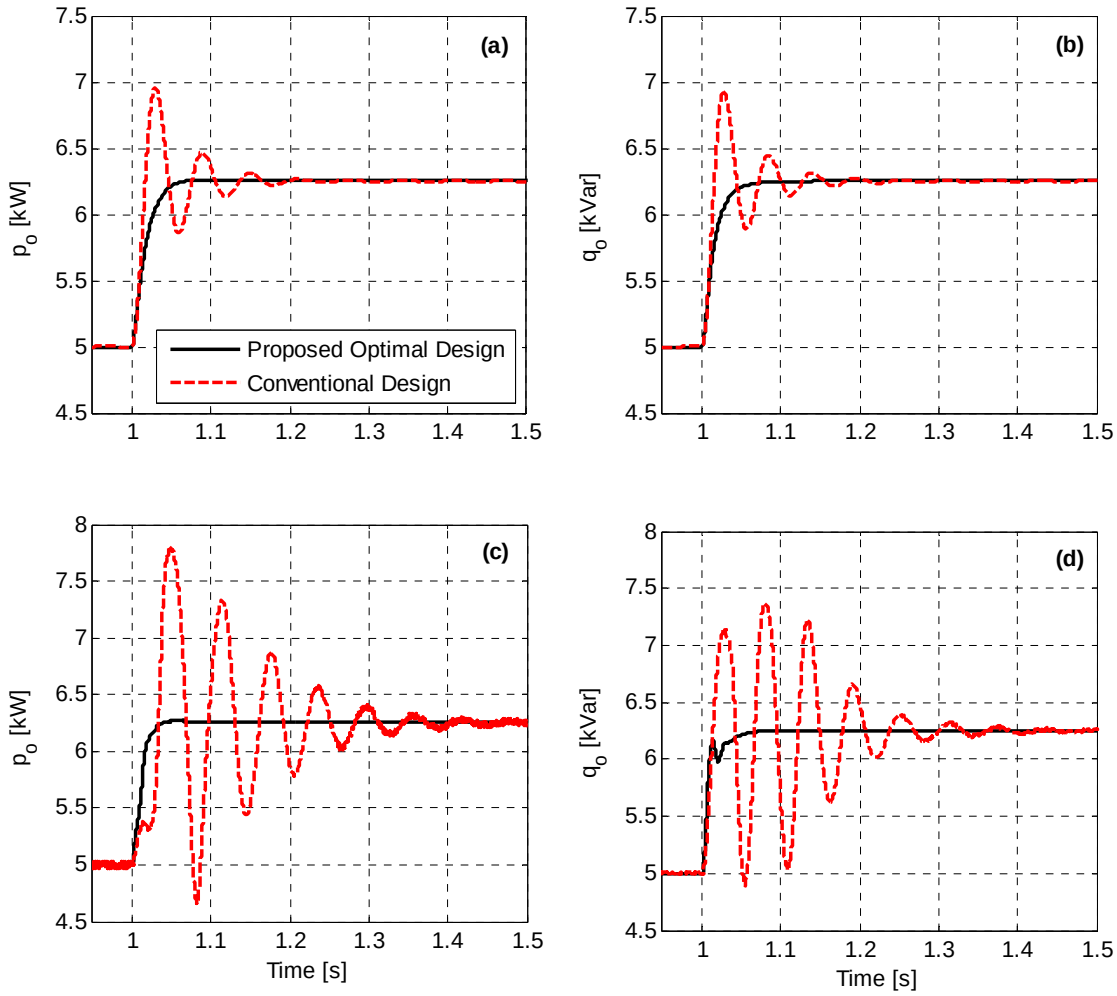

Figure 6.9: Evaluation of grid-connected DG performance at different grid conditions: (a & b) nominal grid impedance; (b & c) higher inductive grid impedance

6.4.2 Performance Evaluation of Droop-based DGs

Figure 6.7(b) demonstrates the test system that incorporates a droop-based DG connected to two loads. In the case of droop-based DGs, the proposed control algorithm optimally tunes the voltage and current controller parameters, i.e., $K = \left[K_{vp}, K_{vi}, K_{ip}, K_{ii}\right]$. Both Load_1 and Load_2 are passive and modeled by constant impedances; Load_1 has a 0.9 lagging power factor, while Load_2 is a highly inductive load. The switch s_2 is assumed to be normally closed, while switch s_3 is normally open.

Figure 6.10 shows the dominant eigenvalues of the system when the DG only supplies Load_1. Again, applying the proposed control algorithm increases the system bandwidth and improves the

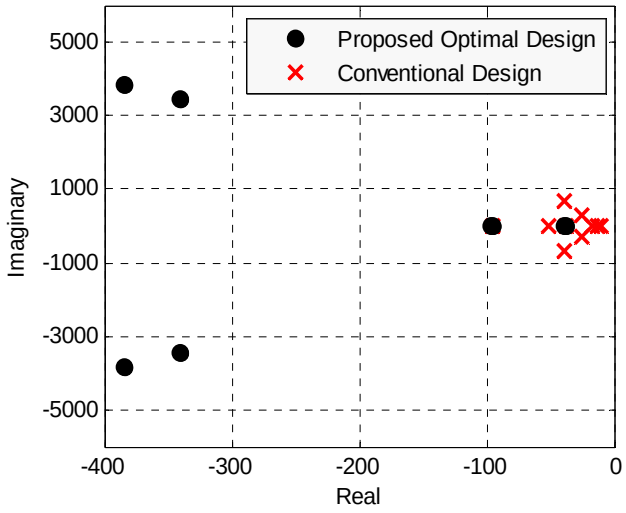

Figure 6.10: Dominant eigenvalues with and without the proposed algorithm, droop-based DG, $Load_1$ case

damping ratio by optimally allocating the dominant eigenvalue. The effectiveness of the proposed control algorithm is assessed by real-time simulations when supplying $Load_1$ and $Load_2$ separately.

The response of droop-based DG to various loading conditions is demonstrated in Figure 6.11. At each loading condition, i.e., $Load_1$ or $Load_2$, the loading is doubled at $t = 1.0$ s to test the attainment of the proposed control algorithm. The conventionally designed DG controllers suffer from oscillatory and sluggish performance, especially when supplying inductive loads, as demonstrated by Figure 6.11(c) and Figure 6.11(d). Alternatively, the proposed DG impedance reshaping algorithm indicates superior performance with faster time response and higher damping compared with the conventional control design. These results confirm the ability of the proposed control algorithm to optimally tune the controller gains of droop-based DGs and robustly mitigate passive load variations.

6.4.3 Performance Evaluation with CPLs

As discussed previously, CPLs are characterized by negative impedance, which can reduce system damping and lead to instability issues. To test the performance of the proposed optimal tuning algorithm when dealing with such loads, a droop-based DG is connected to a CPL representing a simple microgrid dominated by CPLs, as shown in Figure 6.7(c). In this instance, grid admittance should be represented by an active model. The RIVC is employed to estimate the grid admittance which represents the CPL admittance. After identifying the grid admittance, the proposed optimal tuning algorithm is applied, taking into account the DG operating condition and the estimated grid admittance. Any change occurring in the DG operating condition (i.e., related to the DG output

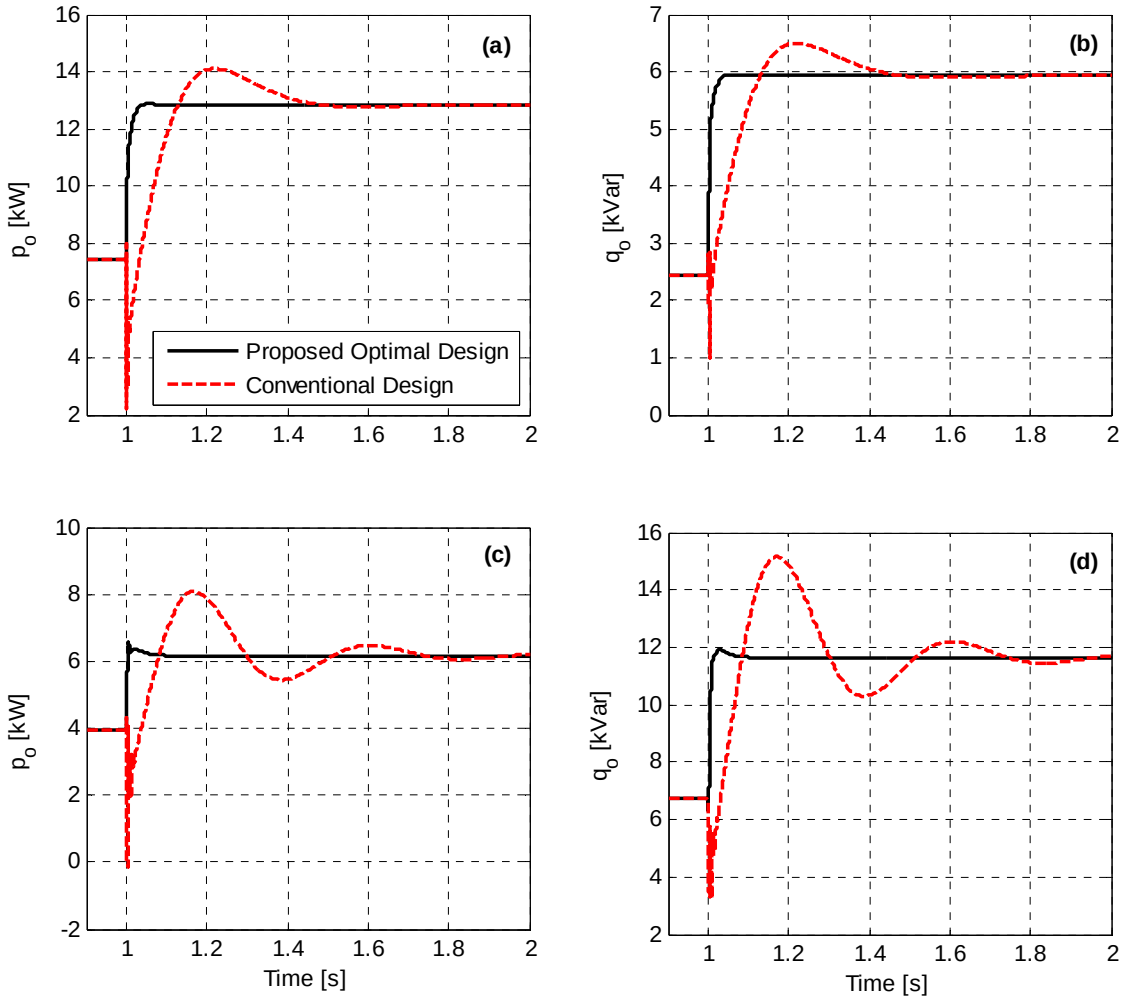

Figure 6.11: Droop-based DG performance evaluation with passive loads: (a) supplying $Load_1$ only; (b) supplying $Load_2$ only

voltage and current) is reflected on the DG output impedance, which will be reshaped by optimizing the controller parameters. Two loading scenarios are considered, namely, light and heavy loadings, by opening and closing the switch s_4, respectively.

Figure 6.12 indicates the dominant poles of the system at the light and heavy loadings. The conventionally designed DG controllers exhibit dominant poles with a lower damping ratio when lightly loaded. In addition, they cannot preserve the system stability in the case of heavy loading. In contrast, the proposed algorithm can maintain the system stability at both light and heavy loadings by

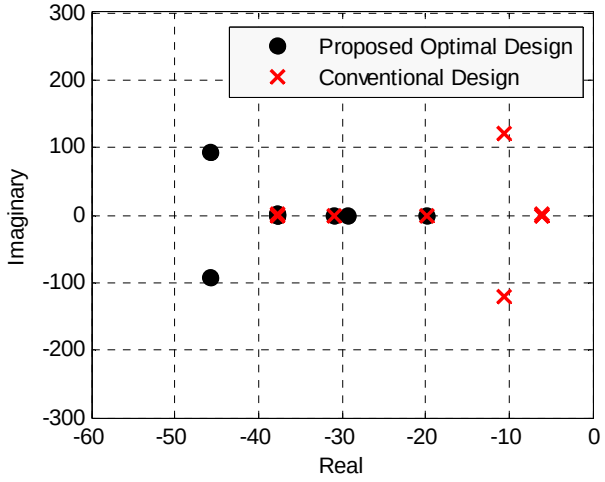

(a)

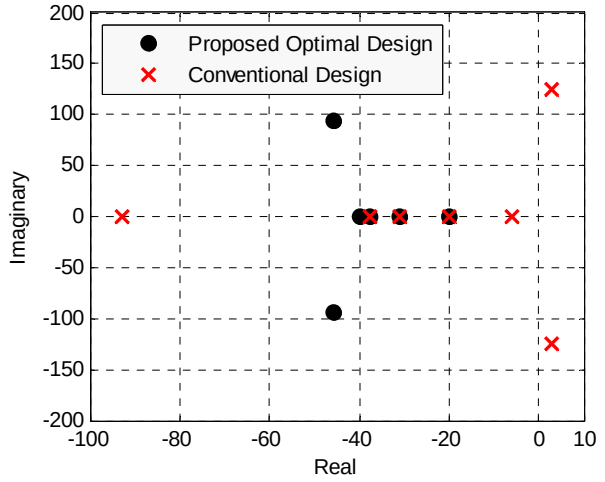

(b)

Figure 6.12: Dominant eigenvalues with and without the proposed algorithm, droop-based DG: (a) light CPL, (b) heavy CPL

moving the dominant poles to the left-hand side, and it can also increase the system damping. These results confirm the effectiveness of the proposed optimal tuning algorithm when dealing with CPLs (i.e., active grid admittances), which are characterized by high-order model representation and negative impedance. Figure 6.13 demonstrates the DG response to the light and heavy loading conditions when the CPL power is increased at t =1.0 s to the values given in Appendix A. For both light and heavy loading conditions, when the DG controller parameters are optimally tuned, the step load increase is accommodated safely with higher damping and faster time response compared with conventional DG control. Once more, the conventional control design shows instability when

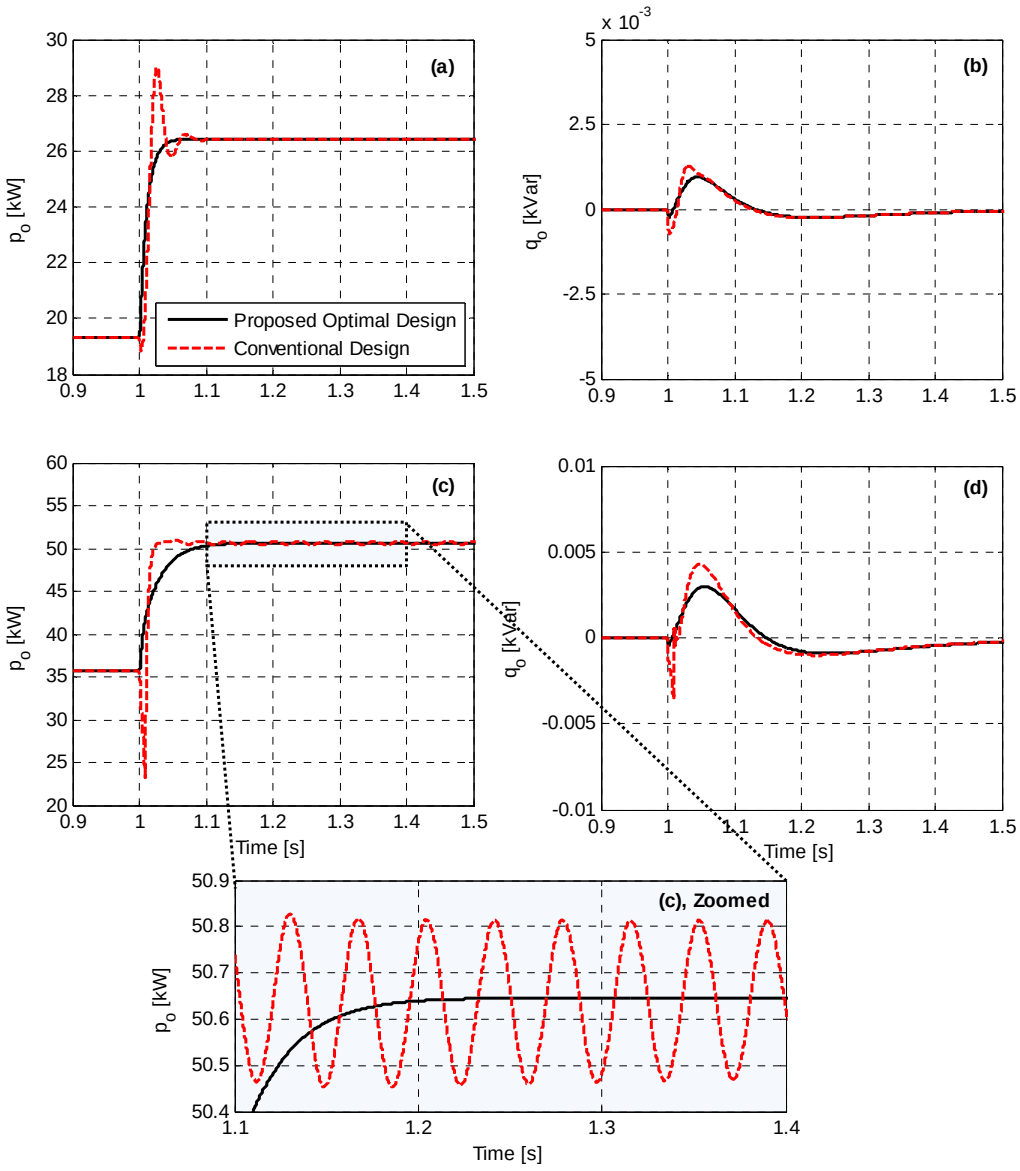

Figure 6.13: Evaluation of droop-based DG performance with CPL: (a & b) 50% loading, (c & d) 100 % loading

supplying a heavy load, as shown in Figure 6.13(c), which corresponds with the rationale for the eigenvalues analysis presented by Figure 6.12(b).

6.5 Discussion

Impedance stability criteria can assess system stability by dividing the system under study into DG source and grid subsystems. By estimating grid impedance parameters, DG output impedance can be reshaped to guarantee system stability and improve dynamic performance. This chapter proposes a

DG impedance reshaping algorithm that adaptively tunes DG control parameters to mitigate variations in grid impedance. The adaptation is done to achieve two control objectives, i.e., maximizing the system bandwidth and damping. The proposed algorithm has the advantage of being applicable with the grid-connected and islanded mode of operation. The proposed control algorithms involve three design stages. First, the multivariable DG impedance models are derived from the DG control design specifications. These proposed impedance models are validated in the frequency domain using a chirp excitation signal. Secondly, a multi-objective optimization is formulated using the ε-constraint method to maximize the system bandwidth and damping. Finally, the solutions provided by the optimization stage are employed to train a NN-based adaptation scheme that tunes the DG control parameters online. Real-time simulations using an HiL application and OPAL RTS were performed to test the effectiveness of the proposed algorithm in ADNs. The results confirm the effectiveness and robustness of the proposed control algorithm for reshaping DG output impedance to meet control objectives and mitigate both passive and active grid impedance variations.

Chapter 7
Summary, Contributions, and Future Work

7.1 Summary and Conclusions

The main goal of this thesis was allowing seamless integration of high DG penetration into the ADN paradigm by developing new DG control algorithms from both SCL and PCL perspectives. From the SCL perspective, new control algorithms were proposed in Chapters 3 and 4 in order to guarantee proper voltage regulation and relaxed tap operation for OLTCs by dispatching DG active and reactive power references. It was shown in Chapter 5 that DG dynamic performance is dependent on its operating condition as well as grid/load impedance. A change in the DG operating condition can be triggered by changing the DG active and reactive power references or DG loading. Also, the grid/load is time-varying and uncertain, and thus a DG primary controller should be adaptively tuned to mitigate such uncertainties. To achieve that purpose, a new grid admittance identification algorithm was proposed in Chapter 5 and utilized in Chapter 6 to develop DG adaptive controllers from a PCL perspective. A detailed summary of the content of each chapter is given below.

In Chapter 3, a coordinated fuzzy-based voltage regulation scheme was proposed for OLTC and DGs. The main motivation of applying fuzzy logic is that it can deal with environments of imperfect information, and thus can reduce communication requirements. The proposed regulation scheme consists of three fuzzy-based control algorithms. The first control algorithm is proposed for the OLTC such that it can mitigate the effect of DGs on the voltage profile. The second control algorithm is proposed to provide DG reactive power sharing to relax the OLTC tap operation. The third control algorithm aims to partially curtail DG active powers to restore a feasible solution from the OLTC perspective. The proposed fuzzy algorithms have the advantage of providing proper voltage regulation with relaxed tap operation, utilizing only the estimated system minimum and maximum voltages. In addition, it avoids numerical instability and convergence problems associated with centralized approaches, as it does not require an optimization algorithm to be run. Real-time simulations were developed to show the success of the proposed fuzzy algorithms on a typical distribution network using OPAL RTS. The results demonstrated the success of the proposed fuzzy algorithms under various operating conditions and system configurations.

In Chapter 4, a V2GQ support strategy was proposed for optimal coordinated voltage regulation in distribution networks with high DG and PEV penetration. The proposed algorithm employs PEVs, DGs, OLTCs to satisfy PEV charging demand and grid voltage requirements with relaxed tap operation and minimum DG active power curtailment. The voltage regulation problem is formulated as non-linear programming and consists of three consecutive stages, in which the outputs of the preceding stages are applied as constraints. The first stage aims to maximize the energy delivered to PEVs to assure PEV owner satisfaction; the second stage maximizes the DG-extracted active power; and the third stage minimizes the voltage deviation from its nominal value utilizing the available PEV and DG reactive powers. The main implicit objective of the third stage problem is relaxing the OLTC tap operation.

In addition, the conventional OLTC control is replaced by a proposed centralized controller that utilizes the output of the third stage to set its tap position. The effectiveness of the proposed algorithm, in a typical distribution network, is validated in real time using OPAL RTS in an HiL application. The results demonstrated the ability of the proposed coordination to provide proper voltage regulation with maximized PEV demand power, maximized DG extracted power, and relaxed OLTC tap operation.

In Chapter 5, a new multivariable grid admittance identification algorithm was proposed with adaptive model order selection, as an ancillary function within the inverter-based DG controllers. It was shown that DG controllers with fixed gains can suffer from instability issues when the grid admittance changes. Due to cross-coupling between the d-axis and q-axis grid admittances, a multivariable estimation is essential. First, controlled voltage pulses are injected by the DG, based on a sensitivity analysis, to ensure a persistence of excitation for the grid admittance. Then, the extracted grid dynamics are processed by the RIVC algorithm to estimate the grid admittance. The theoretical background of the RIVC algorithm was explained, accompanied by its integration within the proposed adaptive model order selection method. Unlike non-parametric identification algorithms, the proposed RIVC provides a parametric multivariable model for the grid admittance which is essential for designing DG adaptive controllers. The proposed algorithm was validated by OPAL RTS in both grid-connected and isolated ADNs, via an HiL application. The results confirmed the accuracy and convergence of the proposed identification in estimating both passive and active grid admittances, without extra hardware.

In Chapter 6, an adaptive DG control algorithm was proposed to optimally reshape the DG output impedance in order to maximize the system damping and bandwidth. The adaptation is essential to cope with variations in grid impedance and changes in DG operating conditions. The proposed algorithm is generic, i.e., can be applied in grid-connected and islanded DGs, and involves three design stages. In the first stage, the multivariable DG output impedance is mathematically derived and verified using a frequency sweep identification method. The grid impedance is also estimated using the proposed identification algorithm presented in Chapter 5 to formulate the impedance stability criteria. In the second stage, a multi-objective programming is formulated using the ε-constraint method to maximize the system damping and bandwidth. Finally, in the third stage, the solutions provided by the optimization stage are employed to train a NN-based adaptation scheme which tunes the DG control parameters online. The proposed algorithm is validated by OPAL RTS in both grid-connected and isolated ADNs, via HiL applications. It was shown that the proposed control algorithm can maintain system stability, increase system bandwidth, and improve system damping under various grid impedances and load natures.

7.2 Contributions

The main contributions of this thesis can be summarized as follows:

1. Development of a coordinated fuzzy-based voltage regulation algorithms with minimal communication requirements for ADNs with high penetration of renewable DGs to reduce DG active power curtailments and relax OLTC operation.
2. Development of an optimal coordinated voltage regulation scheme for ADNs with high penetration of PEVs and DGs to maximize the PEV power demand and DG power generation, and relax the OLTC operation.
3. Development of a multivariable grid impedance (admittance) identification tool for assessing the impedance stability of ADNs and designing DG adaptive controllers.
4. Development of a DG output impedance reshaping algorithm that can provide optimal and adaptive tuning of DG primary controllers to mitigate changes in DG operating condition and grid impedance variations.

7.3 Directions for Future Work

Building on the results illustrated in this thesis, the following subjects are suggested for future studies:

1. Investigating and assessing the impedance stability of ADNs dominated by doubly-fed induction generators (DFIGs). For this study, a multivariable impedance model for DFIGs needs to be derived and validated in the $d-q$ frame. This model, accompanied by the proposed identification algorithm in Chapter 5, will be used to assess system stability and design adaptive controllers for DFIGs.
2. Investigating and assessing the impedance stability of ADNs dominated by permanent magnet synchronous generators (PMSGs). Again, a multivariable impedance model for PMSGs is required to be derived and validated in the $d-q$ frame. This model can then be used to assess system stability and design adaptive controllers for PMSGs.
3. Developing a robust adaptive voltage controller for standalone DGs considering the uncertainties of inverter dc-link voltage to guarantee stable and robust operation during faults. Typically, the dc-link voltage is assumed to be constant when designing the controllers of DG interfacing converter. However, this assumption lacks sufficient accuracy because the dc-link voltage is dependent on renewable energy intermittent powers and grid disturbances. To guarantee a robust performance for the DG interfacing converter, its controllers should be designed taking into account the dc-link voltage fluctuations.

Appendix A

Data of Test Networks

The data of the test system shown in Figure 3.7 are given as follows:

Table A. 1: 46-bus test system data [91]

Feeder	From	To	Z_{Line} [Ω]	To-node Load/DG [MW]	
				P	Q
A	MV	A01, DGA1	0.144+0.196j	1.01, 2.0	0.29
	A01	A02	0.108+0.147j	0.80	0.23
	A02	A03	0.163+0.179j	1.01	0.29
	A03	A04	0.205+0.225j	0.80	0.23
	A04	A05	0.172+0.188j	0.30	0.09
	A05	A06, DGA2	0.174+0.191j	0.00, 2.0	0.00
	A06	A07	0.149+0.164j	1.01	0.29
	A07	A08	0.165+0.181j	1.01	0.29
	A08	A09	0.249+0.122j	0.00	0.00
	A09	A10, DGA3	0.283+0.139j	1.01, 4.0	0.29
	A10	A11	0.249+0.122j	1.01	0.29
	A11	A12	0.277+0.136j	1.01	0.29
	A12	A13	0.218+0.107j	1.01	0.29
	A13	A14, DGA4	0.302+0.148j	0.50, 2.65	0.15
	A08	A15	0.115+0.096j	1.01	0.29
	A15	A16	0.109+0.092j	0.00	0.00
	A16	A17	0.202+0.099j	1.01	0.29
	A17	A18, DGA5	0.474+0.232j	1.01, 7.5	0.29
	A16	A19	0.297+0.146j	0.00	0.00
	A19	A20	0.381+0.187j	0.50	0.15
	A20	A21, DGA6	0.318+0.156j	0.30, 6.0	0.09
B	MV	B01	0.062+0.053j	0.39	0.15
	B01	B02	0.056+0.048j	0.39	0.15
	B02	B03	0.071+0.061j	0.00	0.00
	B03	B04	0.316+0.432j	0.39	0.15
	B04	B05	0.289+0.395j	0.39	0.15
	B05	B06	0.144+0.196j	0.78	0.29
	B06	B07, DGB2	0.119+0.162j	0.39, 5.0	0.15
	B03	B08, DGB1	0.128+0.175j	0.78, 2.0	0.29
	B08	B09	0.127+0.174j	0.78	0.29
	B09	B10	0.160+0.219j	0.00	0.00
	B10	B11	0.152+0.207j	0.39	0.15
	B11	B12	0.149+0.203j	0.23	0.09
	B12	B13	0.155+0.211j	0.78	0.29
	B13	B14	0.114+0.156j	0.39	0.15
	B14	B15	0.161+0.219j	0.78	0.29
	B15	B16	0.157+0.214j	0.39	0.15
	B10	B17	0.107+0.147j	0.00	0.00
	B17	B18, DGB3	0.130+0.177j	0.00, 0.8	0.00
	B18	B19	0.520+0.710j	0.78	0.29
	B19	B20	0.142+0.156j	0.78	0.29
	B20	B21	0.813+0.604j	0.78	0.29
	B21	B22	0.811+0.603j	0.78	0.29
	B22	B23	1.034+0.769j	1.56	0.59

- OLTC parameters: $110 \pm 16 \times 0.69 / 20\,\text{kV}$, $DB = 0.0065\,\text{pu}$, $\Delta a = 0.0065$ pu, $\tau_o = 30\,\text{s}$, $T_m = 5\,\text{s}$.

The data of the test system demonstrated in Figure 4.6 are given as follows:

Table A. 2: 38-bus test system data [100]

From	To	Line	Z_{Line} [pu]	To-node Load [pu]	
				P	Q
1	2	1	0.000574+0.000293j	0.1	0.06
2	3	6	0.003070+0.001564j	0.09	0.04
3	4	11	0.002279+0.001161j	0.12	0.08
4	5	12	0.002373+0.001209j	0.06	0.03
5	6	13	0.005100+0.004402j	0.06	0.02
6	7	22	0.001166+0.003853j	0.20	0.10
7	8	23	0.004430+0.001464j	0.20	0.10
8	9	25	0.006413+0.004608j	0.06	0.02
9	10	27	0.006501+0.004608j	0.06	0.02
10	11	28	0.001224+0.000405j	0.045	0.03
11	12	29	0.002331+0.000771j	0.06	0.035
12	13	31	0.009141+0.007192j	0.06	0.035
13	14	32	0.003372+0.004439j	0.12	0.08
14	15	33	0.003680+0.003275j	0.06	0.01
15	16	34	0.004647+0.003394j	0.06	0.02
16	17	35	0.008026+0.010716j	0.06	0.02
17	18	36	0.004558+0.003574j	0.09	0.04
2	19	2	0.001021+0.000974j	0.09	0.04
19	20	3	0.009366+0.008440j	0.09	0.04
20	21	4	0.002550+0.002979j	0.09	0.04
21	22	5	0.004414+0.005836j	0.09	0.04
3	23	7	0.002809+0.001920j	0.09	0.05
23	24	8	0.005592+0.004415j	0.42	0.20
24	25	9	0.005579+0.004366j	0.42	0.20
6	26	14	0.001264+0.000644j	0.06	0.025
26	27	15	0.001770+0.000901j	0.06	0.025
27	28	16	0.006594+0.005814j	0.06	0.02
28	29	17	0.005007+0.004362j	0.12	0.07
29	30	18	0.003160+0.001610j	0.20	0.60
30	31	19	0.006067+0.005996j	0.15	0.07
31	32	20	0.001933+0.002253j	0.21	0.10
32	33	21	0.002123+0.003301j	0.06	0.04
8	34	24	0.012453+0.012453j	0.00	0.00
9	35	26	0.012453+0.012453j	0.00	0.00
12	36	30	0.012453+0.012453j	0.00	0.00
18	37	37	0.003113+0.003113j	0.00	0.00
25	38	10	0.003113+0.003113j	0.00	0.00

Table A. 3: OLTCs parameters for the 38-bus system [94]

Parameters	OLTC1	OLTC2
Voltage Rating (kV)	69 ± 16 $\times 0.45/12.66$	12.66 ± 16 $\times 0.082/12.66$
DB (pu)	0.0065	0.0065
Δa (pu)	0.0065	0.0065
No. of taps $(2N_{\max})$	32	32
τ_o (s)	30	20
T_m (s)	5	5

The parameters of the studied systems shown in Figure 5.3 and Figure 5.12 are given as follows:

Table A. 4: Passive and active grid parameters

Component	Parameters
Droop-based DG	30 kVA, 208 V (L-L); 60 Hz; voltage controller: $K_{vp} = 0.125$, $K_{vi} = 50$; current controller: $K_{ip} = 10$, $K_{ii} = 120$; ac filter: $L_f = 2.0$ mH, $R_f = 0.1\,\Omega$, $C_f = 45\ \mu$F.
PQ-based DGs	20 kVA, 208 V (L-L); 60 Hz; power controller: $K_{pp} = 0.01$, $K_{pi} = 0.5$; current controller: $K_{ip} = 10$, $K_{ii} = 120$; ac filter: $L_f = 2.0$ mH, $R_f = 0.1\,\Omega$, $C_f = 45\ \mu$F.
CPL	20 kW, 208 V (L-L); 60 Hz; dc voltage controller: $K_{vp,dc} = 0.165$, $K_{vi,dc} = 45$; current controller: $K_{ip} = 2$, $K_{ii} = 150$; ac filter: $L_f = 2.0$ mH, $R_f = 0.1\,\Omega$, $C_f = 45\ \mu$F.
Feeders	$L_{f_1} = L_{f_2} = L_{f_3} = 1.5$ mH, $R_{f_1} = R_{f_2} = R_{f_3} = 0.5\,\Omega$.
Passive Loads	$L_{l_1} = L_{l_2} = 50.0$ mH, $R_{l_1} = R_{l_2} = 50.0\,\Omega$.

The parameters of the test systems illustrated in Figure 6.7 are given as follows:

- Feeders: $L_1 = 2.0$ mH, $R_1 = 0.5\,\Omega$, $L_2 = 1.0$ mH, $R_2 = 0.05\,\Omega$, $L_3 = 2.0$ mH, $R_3 = 0.15\,\Omega$, $L_4 = 2.0$ mH, $R_4 = 0.15\,\Omega$.
- Passive loads: $L_{l_1} = 2.5$ mH, $R_{l_1} = 5.0\,\Omega$, $L_{l_2} = 10.0$ mH, $R_{l_2} = 2.5\,\Omega$.
- CPLs: $P_{CPL1} = 25.0$ kW, $P_{CPL2} = 20.0$ kW.

Appendix B

Constant-Power Load Impedance Modeling

This section illustrates the impedance modeling of constant-power loads (CPLs) in the $d-q$ frame. Typically, CPLs are interfaced though a power electronic converter as shown in Figure B. 1(a). From the $d-$axis control loop (i.e., illustrated in Figure B. 1(b)), the relation between the $d-$axis current and dc-link voltage can be given by

$$\Delta I_{od} = -\underbrace{\left(\frac{G_i G_{v,dc}}{R_f + sL_f + G_i} \right)}_{GvI} \Delta V_{dc} \tag{B.1}$$

The dc-side converter current I_{dc} can be calculated by

$$I_{dc} = I_c + I_{CPL} \tag{B.2}$$

The power balance equation can be expressed by neglecting the power losses in the filter resistance, i.e.,

$$\begin{aligned} P_o &\approx P_{in} \\ 1.5G_f \left(V_{od} I_{od} \right) &\approx V_{dc} I_{dc} \end{aligned} \tag{B.3}$$

By substituting from (B.2) in (B.3), the small-signal perturbation in the dc-link voltage can be given by

$$\Delta V_{dc} = \frac{1.5G_f \left[V_{od}^o \Delta I_{od} + I_{od}^o \Delta V_{od} \right]}{sC_{dc} V_{dc}^o} \tag{B.4}$$

The $d-$axis control dynamics can be expressed only by the DG output voltage and current, when substituting from (B.4) in (B.1), as follows:

$$\left(V_{od}^o + \frac{sC_{dc} V_{dc}^o}{1.5G_{vI}} \right) \Delta I_{od} = -I_{od}^o \Delta V_{od} \tag{B.5}$$

Thus, the $d-$axis admittance matrix of CPLs can be given by

$$Y_{dd} = \frac{-I_{od}^o}{\left(V_{od}^o + \frac{sC_{dc} V_{dc}^o}{1.5G_f G_{vI}} \right)} \tag{B.6}$$

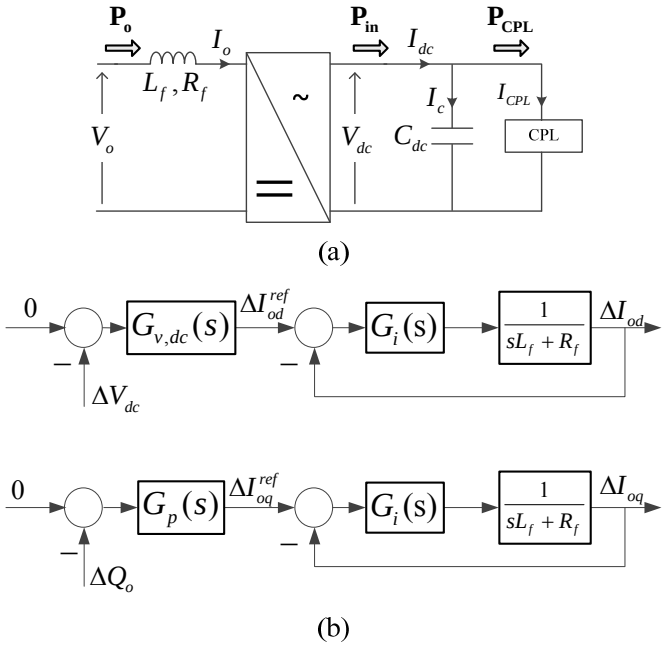

Figure B. 1: CPL control: (a) power circuit, (b) control loops

From the $q-\text{axis}$ control loop (i.e., shown in Figure B. 1(b)), the relation between the $q-\text{axis}$ current and DG output reactive power can be given by

$$\Delta I_{oq} = -\underbrace{\left(\frac{G_i G_p}{R_f + sL_f + G_i}\right)}_{Gip}\Delta Q_o \tag{B.7}$$

where

$$\Delta Q_o = 1.5 G_f \left[V_{od}^o \Delta I_{oq} - I_{od}^o \Delta V_{oq}\right] \tag{B.8}$$

The $q-\text{axis}$ admittance matrix of CPLs can be given by substituting from (B.8) in (B.7), as follows:

$$Y_{qq} = \frac{-1.5 G_f G_{ip} I_{od}^o}{1 + 1.5 G_f G_{ip} V_{od}^o} \tag{B.9}$$

Hence, the admittance matrix of CPLs can be given by

$$\mathrm{Y_{CPL}} = \begin{bmatrix} Y_{dd} & 0 \\ 0 & Y_{qq} \end{bmatrix} \tag{B.10}$$

Appendix C
Frequency Sweep Impedance Estimation

According to [59], two independent sets of injected currents are required for estimating the grid impedance matrix, because it consists of four unknowns: Z_{dd}, Z_{dq}, Z_{qd}, and Z_{qq}. The injected currents can thus be represented as follows:

$$\begin{cases} i_{a1}^{inj} = 0 \\ i_{b1}^{inj} t = -I_m \cos(\omega_{inj} t + \omega_o t) \\ i_{c1}^{inj} = I_m \cos(\omega_{inj} t + \omega_o t) \end{cases} \tag{C.1}$$

$$\begin{cases} i_{a2}^{inj} = 0 \\ i_{b2}^{inj} t = -I_m \cos(\omega_{inj} t - \omega_o t) \\ i_{c2}^{inj} = I_m \cos(\omega_{inj} t - \omega_o t) \end{cases} \tag{C.2}$$

where I_m, ω_{inj}, and ω_o are the amplitude and frequency of the injected currents, and the fundamental frequency of the system, respectively. Figure C. 1 shows a setup for estimating the grid impedance using the frequency sweep method. In the $d-q$ frame, the injected current components at the injected frequency are given by

$$\begin{cases} i_{d1}^{inj} = \frac{1}{\sqrt{3}} I_m \sin(\omega_{inj}\, \mathrm{t}) \\ i_{q1}^{inj} = \frac{1}{\sqrt{3}} I_m \cos(\omega_{inj}\, \mathrm{t}) \end{cases} \tag{C.3}$$

$$\begin{cases} i_{d2}^{inj} = -\frac{1}{\sqrt{3}} I_m \sin(\omega_{inj}\, \mathrm{t}) \\ i_{q2}^{inj} = \frac{1}{\sqrt{3}} I_m \cos(\omega_{inj}\, \mathrm{t}) \end{cases} \tag{C.4}$$

The two current vectors described by (C.3) and (C.4) are linearly independent and can hence be used for estimating the grid impedance. At the injected frequency, the currents and voltages measured at the point of common coupling (PCC), i.e., $\tilde{I}_o$ and $\tilde{V}_o$, can be extracted using fast Fourier transform (FFT), forming

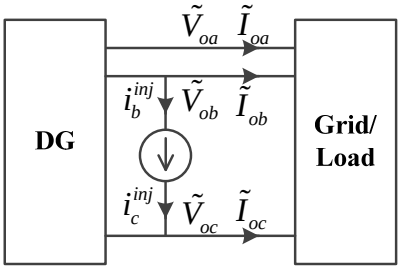

Figure C. 1: Line-to-line current injection for the frequency sweep method [59]

$$\begin{cases} \tilde{V}_{od1} = Z_{dd}\tilde{I}_{od1} + Z_{dq}\tilde{I}_{oq1} \\ \tilde{V}_{oq1} = Z_{qd}\tilde{I}_{od1} + Z_{qq}\tilde{I}_{oq1} \end{cases} \tag{C.5}$$

$$\begin{cases} \tilde{V}_{od2} = Z_{dd}\tilde{I}_{od2} + Z_{dq}\tilde{I}_{oq2} \\ \tilde{V}_{oq2} = Z_{qd}\tilde{I}_{od2} + Z_{qq}\tilde{I}_{oq2} \end{cases}. \tag{C.6}$$

The grid impedance at the injection frequency ω_{inj} can thus be calculated as follows:

$$Z_{\text{Grid}}(j\omega_{inj}) = \underbrace{\begin{bmatrix} \tilde{V}_{od1} & \tilde{V}_{od2} \\ \tilde{V}_{oq1} & \tilde{V}_{oq2} \end{bmatrix}\begin{bmatrix} \tilde{I}_{od1} & \tilde{I}_{od2} \\ \tilde{I}_{oq1} & \tilde{I}_{oq2} \end{bmatrix}^{-1}}_{Y_{\text{Grid}}^{-1}(j\omega_{inj})} \tag{C.7}$$

To sweep a wide frequency spectrum of the grid impedance, the injected currents given by (C.1) and (C.2) are applied repeatedly at different values of ω_{inj} with the application of the previously discussed grid impedance calculation procedure.

Bibliography

[1] A. P. Sakis Meliopoulos, G. Cokkinides, R. Huang, E. Farantatos, S. Choi, Y. Lee, and X. Yu, "Smart Grid Technologies for Autonomous Operation and Control," *IEEE Trans. Smart Grid*, vol. 2, no. 1, pp. 1–10, Mar. 2011.

[2] G. T. Heydt, "The Next Generation of Power Distribution Systems," *IEEE Trans. Smart Grid*, vol. 1, no. 3, pp. 225–235, Dec. 2010.

[3] M. F. Shaaban and E. F. El-Saadany, "Accommodating High Penetrations of PEVs and Renewable DG Considering Uncertainties in Distribution Systems," *IEEE Trans. Power Syst.*, vol. 29, no. 1, pp. 259–270, Jan. 2014.

[4] F. Katiraei, R. Iravani, N. Hatziargyriou, and A. Dimeas, "Microgrids management," *IEEE Power Energy Mag.*, vol. 6, no. 3, pp. 54–65, May 2008.

[5] F. Blaabjerg, R. Teodorescu, M. Liserre, and A. V. Timbus, "Overview of Control and Grid Synchronization for Distributed Power Generation Systems," *IEEE Trans. Ind. Electron.*, vol. 53, no. 5, pp. 1398–1409, Oct. 2006.

[6] J. M. Guerrero, P. C. Loh, T.-L. Lee, and M. Chandorkar, "Advanced Control Architectures for Intelligent Microgrids—Part II: Power Quality, Energy Storage, and AC/DC Microgrids," *IEEE Trans. Ind. Electron.*, vol. 60, no. 4, pp. 1263–1270, Apr. 2013.

[7] F. Z. Peng, "Special Issue on Distributed Power Generation," *IEEE Trans. Power Electron.*, vol. 19, no. 5, pp. 1157–1158, 2004.

[8] B. Maurhoff and G. Wood, "Dispersed generation-reduce power costs and improve service reliability," in *Rural Electric Power Conference. Papers Presented at the 44th Annual Conference (Cat. No.00CH37071)*, 2000, pp. C5/1–C5/7.

[9] J. Driesen and F. Katiraei, "Design for distributed energy resources," *IEEE Power Energy Mag.*, vol. 6, no. 3, pp. 30–40, May 2008.

[10] Y. Mohamed, "New control algorithms for the distributed generation interface in grid-connected and micro-grid systems," PhD thesis, ECE, University of Waterloo, Waterloo, ON, 2008.

[11] H. E. Farag, E. F. El-Saadany, and R. Seethapathy, "A Two Ways Communication-Based Distributed Control for Voltage Regulation in Smart Distribution Feeders," *IEEE Trans. Smart Grid*, vol. 3, no. 1, pp. 271–281, Mar. 2012.

[12] F. A. Viawan and D. Karlsson, "Voltage and Reactive Power Control in Systems With Synchronous Machine-Based Distributed Generation," *IEEE Trans. Power Deliv.*, vol. 23, no. 2, pp. 1079–1087, Apr. 2008.

[13] J. M. Guerrero, J. C. Vasquez, and R. Teodorescu, "Hierarchical control of droop-controlled DC and AC microgrids — a general approach towards standardization," in *2009 35th Annual Conference of IEEE Industrial Electronics*, 2009, pp. 4305–4310.

[14] J. A. P. Lopes, C. L. Moreira, and A. G. Madureira, "Defining Control Strategies for MicroGrids Islanded Operation," *IEEE Trans. Power Syst.*, vol. 21, no. 2, pp. 916–924, May 2006.

[15] D. Martin, "Design of Parallel Inverters for Smooth Mode Transfer Microgrid Applications," *IEEE Trans. Power Electron.*, vol. 25, no. 1, pp. 6–15, Jan. 2010.

[16] K. T. Tan, X. Y. Peng, P. L. So, Y. C. Chu, and M. Z. Q. Chen, "Centralized Control for Parallel Operation of Distributed Generation Inverters in Microgrids," *IEEE Trans. Smart Grid*, vol. 3, no. 4, pp. 1977–1987, Dec. 2012.

[17] J. M. Guerrero, J. C. Vasquez, J. Matas, L. G. de Vicuna, and M. Castilla, "Hierarchical Control of Droop-Controlled AC and DC Microgrids—A General Approach Toward Standardization," *IEEE Trans. Ind. Electron.*, vol. 58, no. 1, pp. 158–172, Jan. 2011.

[18] A. Yazdani and R. Iravani, *Voltage-Sourced Converters in Power Systems*. Wiley, 2010.

[19] M. A. Zamani, A. Yazdani, and T. S. Sidhu, "A Control Strategy for Enhanced Operation of Inverter-Based Microgrids Under Transient Disturbances and Network Faults," *IEEE Trans. Power Deliv.*, vol. 27, no. 4, pp. 1737–1747, Oct. 2012.

[20] A. A. A. Radwan and Y. A.-R. I. Mohamed, "Modeling, Analysis, and Stabilization of Converter-Fed AC Microgrids With High Penetration of Converter-Interfaced Loads," *IEEE Trans. Smart Grid*, vol. 3, no. 3, pp. 1213–1225, Sep. 2012.

[21] F. Katiraei, "Dynamic analysis and control of distributed energy resources in a micro-grid," PhD thesis, ECE, University of Toronto, ON, 2005.

[22] A. Yazdani and R. Iravani, "An Accurate Model for the DC-Side Voltage Control of the Neutral Point Diode Clamped Converter," *IEEE Trans. Power Deliv.*, vol. 21, no. 1, pp. 185–193, Jan. 2006.

[23] Y. Mohamed and E. F. El-Saadany, "Adaptive Decentralized Droop Controller to Preserve Power Sharing Stability of Paralleled Inverters in Distributed Generation Microgrids," *IEEE Trans. Power Electron.*, vol. 23, no. 6, pp. 2806–2816, Nov. 2008.

[24] S.-K. Chung, "A phase tracking system for three phase utility interface inverters," *IEEE Trans. Power Electron.*, vol. 15, no. 3, pp. 431–438, May 2000.

[25] M. Karimi-Ghartemani and M. R. Iravani, "A Method for Synchronization of Power Electronic Converters in Polluted and Variable-Frequency Environments," *IEEE Trans. Power Syst.*, vol. 19, no. 3, pp. 1263–1270, Aug. 2004.

[26] R. I. Bojoi, G. Griva, V. Bostan, M. Guerriero, F. Farina, and F. Profumo, "Current Control Strategy for Power Conditioners Using Sinusoidal Signal Integrators in Synchronous Reference Frame," *IEEE Trans. Power Electron.*, vol. 20, no. 6, pp. 1402–1412, Nov. 2005.

[27] M. Karimi-Ghartemani and H. Karimi, "Processing of Symmetrical Components in Time-Domain," *IEEE Trans. Power Syst.*, vol. 22, no. 2, pp. 572–579, May 2007.

[28] M. Karimi-Ghartemani, M. Mojiri, A. Safaee, J. Å. Walseth, S. A. Khajehoddin, P. Jain, and A. Bakhshai, "A New Phase-Locked Loop System for Three-Phase Applications," *IEEE Trans. Power Electron.*, vol. 28, no. 3, pp. 1208–1218, Mar. 2013.

[29] P. N. Vovos, A. E. Kiprakis, A. R. Wallace, and G. P. Harrison, "Centralized and Distributed Voltage Control: Impact on Distributed Generation Penetration," *IEEE Trans. Power Syst.*, vol. 22, no. 1, pp. 476–483, Feb. 2007.

[30] T. Senjyu, Y. Miyazato, A. Yona, N. Urasaki, and T. Funabashi, "Optimal Distribution Voltage Control and Coordination With Distributed Generation," *IEEE Trans. Power Deliv.*, vol. 23, no. 2, pp. 1236–1242, Apr. 2008.

[31] S. Deshmukh, B. Natarajan, and A. Pahwa, "Voltage/VAR Control in Distribution Networks via Reactive Power Injection Through Distributed Generators," *IEEE Trans. Smart Grid*, vol. 3, no. 3, pp. 1226–1234, Sep. 2012.

[32] L. Yu, D. Czarkowski, and F. de Leon, "Optimal Distributed Voltage Regulation for Secondary Networks With DGs," *IEEE Trans. Smart Grid*, vol. 3, no. 2, pp. 959–967, Jun. 2012.

[33] N. Daratha, B. Das, and J. Sharma, "Coordination Between OLTC and SVC for Voltage Regulation in Unbalanced Distribution System Distributed Generation," *IEEE Trans. Power Syst.*, vol. 29, no. 1, pp. 1–11, 2013.

[34] Y. P. Agalgaonkar, B. C. Pal, and R. A. Jabr, "Distribution Voltage Control Considering the Impact of PV Generation on Tap Changers and Autonomous Regulators," *IEEE Trans. Power Syst.*, vol. 29, no. 1, pp. 182–192, 2014.

[35] A. Bonfiglio, M. Brignone, F. Delfino, and R. Procopio, "Optimal Control and Operation of Grid-Connected Photovoltaic Production Units for Voltage Support in Medium-Voltage Networks," *IEEE Trans. Sustain. Energy*, vol. 5, no. 1, pp. 254–263, Jan. 2014.

[36] M. E. Baran and I. M. El-Markabi, "A Multiagent-Based Dispatching Scheme for Distributed Generators for Voltage Support on Distribution Feeders," *IEEE Trans. Power Syst.*, vol. 22, no. 1, pp. 52–59, Feb. 2007.

[37] M. E. Elkhatib, R. El-Shatshat, and M. M. A. Salama, "Novel Coordinated Voltage Control for Smart Distribution Networks With DG," *IEEE Trans. Smart Grid*, vol. 2, no. 4, pp. 598–605, Dec. 2011.

[38] X. Liu, A. Aichhorn, L. Liu, and H. Li, "Coordinated Control of Distributed Energy Storage System With Tap Changer Transformers for Voltage Rise Mitigation Under High Photovoltaic Penetration," *IEEE Trans. Smart Grid*, vol. 3, no. 2, pp. 897–906, Jun. 2012.

[39] H. E. Z. Farag, "A Novel Cooperative Protocol for Distributed Voltage Control in Active Distribution Systems," *IEEE Trans. Power Syst.*, vol. 28, no. 2, pp. 1645–1656, May 2013.

[40] L. Carradore and R. Turri, "Electric Vehicles participation in distribution network voltage regulation," in *Universities Power Engineering Conference (UPEC)*, 2010, pp. 1–6.

[41] A. S. Masoum, S. Deilami, P. S. Moses, M. A. S. Masoum, and A. Abu-Siada, "Smart load management of plug-in electric vehicles in distribution and residential networks with charging stations for peak shaving and loss minimisation considering voltage regulation," *IET Gener. Transm. Distrib.*, vol. 5, no. 8, p. 877, 2011.

[42] S. Su, J. Jiang, and W. Wang, "An autonomous decentralized voltage control scheme in PEV charging devices on the distribution network- reactive power compensation for voltage decreases caused by household loads and charging devices," *Int. Trans. Electr. Energy Syst.*, vol. 24, no. 3, pp. 412–432, Mar. 2014.

[43] Y. Mitsukuri, R. Hara, H. Kita, E. Kamiya, N. Hiraiwa, and E. Kogure, "Voltage regulation in distribution system utilizing electric vehicles and communication," in *PES T&D 2012*, 2012, pp. 1–6.

[44] E. A. A. Coelho, P. C. Cortizo, and P. F. D. Garcia, "Small signal stability for single phase inverter connected to stiff AC system," in *IEEE Industry Applications Conference. Thirty-Forth IAS Annual Meeting (Cat. No.99CH36370)*, 1999, vol. 4, pp. 2180–2187.

[45] E. A. A. Coelho, P. C. Cortizo, and P. F. D. Garcia, "Small-signal stability for parallel-connected inverters in stand-alone AC supply systems," *IEEE Trans. Ind. Appl.*, vol. 38, no. 2, pp. 533–542, 2002.

[46] Y. Li, D. M. Vilathgamuwa, and P. C. Loh, "Design, Analysis, and Real-Time Testing of a Controller for Multibus Microgrid System," *IEEE Trans. Power Electron.*, vol. 19, no. 5, pp. 1195–1204, Sep. 2004.

[47] N. Pogaku, M. Prodanovic, and T. C. Green, "Modeling, Analysis and Testing of Autonomous Operation of an Inverter-Based Microgrid," *IEEE Trans. Power Electron.*, vol. 22, no. 2, pp. 613–625, Mar. 2007.

[48] F. Katiraei, M. R. Iravani, and P. W. Lehn, "Small-signal dynamic model of a micro-grid including conventional and electronically interfaced distributed resources," *IET Gener. Transm. Distrib.*, vol. 1, no. 3, p. 369, 2007.

[49] R. Middlebrook, "Input filter considerations in design and application of switching regulators," *Proc. IEEE Ind. Appl. Soc. Conf.*, pp. 91–107, 1976.

[50] M. Belkhayat, “Stability criteria for ac power systems with regulated loads,” Ph.D. dissertation, Purdue Univ., West Lafayette, IN, 1997.

[51] J. Sun, “Impedance-Based Stability Criterion for Grid-Connected Inverters,” *IEEE Trans. Power Electron.*, vol. 26, no. 11, pp. 3075–3078, Nov. 2011.

[52] J. Sun, “AC power electronic systems: Stability and power quality,” in *2008 11th Workshop on Control and Modeling for Power Electronics*, 2008, pp. 1–10.

[53] F. C. Lee, “Impedance specifications for stable DC distributed power systems,” *IEEE Trans. Power Electron.*, vol. 17, no. 2, pp. 157–162, Mar. 2002.

[54] V. Valdivia, A. Lázaro, A. Barrado, P. Zumel, C. Fernández, and M. Sanz, “Impedance Identification Procedure of Three-Phase Balanced Voltage Source Inverters Based on Transient Response Measurements,” *IEEE Trans. Power Electron.*, vol. 26, no. 12, pp. 3810–3816, Dec. 2011.

[55] M. Ciobotaru, R. Teodorescu, P. Rodriguez, A. Timbus, and F. Blaabjerg, “Online grid impedance estimation for single-phase grid-connected systems using PQ variations,” in *2007 IEEE Power Electronics Specialists Conference*, 2007, pp. 2306–2312.

[56] M. Liserre, F. Blaabjerg, and R. Teodorescu, “Grid Impedance Estimation via Excitation of LCL -Filter Resonance,” *IEEE Trans. Ind. Appl.*, vol. 43, no. 5, pp. 1401–1407, 2007.

[57] S. Cobreces, E. J. Bueno, D. Pizarro, F. J. Rodriguez, and F. Huerta, “Grid Impedance Monitoring System for Distributed Power Generation Electronic Interfaces,” *IEEE Trans. Instrum. Meas.*, vol. 58, no. 9, pp. 3112–3121, Sep. 2009.

[58] J. Yang, W. Li, T. Chen, W. Xu, and M. Wu, “Online estimation and application of power grid impedance matrices based on synchronised phasor measurements,” *IET Gener. Transm. Distrib.*, vol. 4, no. 9, p. 1052, 2010.

[59] J. Huang, K. A. Corzine, and M. Belkhayat, “Small-Signal Impedance Measurement of Power-Electronics-Based AC Power Systems Using Line-to-Line Current Injection,” *IEEE Trans. Power Electron.*, vol. 24, no. 2, pp. 445–455, Feb. 2009.

[60] M. Cespedes and J. Sun, “Online grid impedance identification for adaptive control of grid-connected inverters,” in *2012 IEEE Energy Conversion Congress and Exposition (ECCE)*, 2012, pp. 914–921.

[61] V. Valdivia, A. Lazaro, A. Barrado, P. Zumel, C. Fernandez, and M. Sanz, “Black-Box Modeling of Three-Phase Voltage Source Inverters for System-Level Analysis,” *IEEE Trans. Ind. Electron.*, vol. 59, no. 9, pp. 3648–3662, Sep. 2012.

[62] D. Martin and E. Santi, “Autotuning of Digital Deadbeat Current Controllers for Grid-Tie Inverters Using Wide Bandwidth Impedance Identification,” *IEEE Trans. Ind. Appl.*, vol. 50, no. 1, pp. 441–451, Jan. 2014.

[63] N. Hoffmann and F. W. Fuchs, “Minimal Invasive Equivalent Grid Impedance Estimation in Inductive–Resistive Power Networks Using Extended Kalman Filter,” *IEEE Trans. Power Electron.*, vol. 29, no. 2, pp. 631–641, Feb. 2014.

[64] K. J. Astrom and B. Wittenmark, *Adaptive Control*, Second Edi. Dover Publications, 2013.

[65] D. T. Rizy and J. D. Kueck, “Adaptive Voltage Control With Distributed Energy Resources: Algorithm, Theoretical Analysis, Simulation, and Field Test Verification,” *IEEE Trans. Power Syst.*, vol. 25, no. 3, pp. 1638–1647, Aug. 2010.

[66] A. E. Leon, J. M. Mauricio, J. A. Solsona, and A. Gomez-Exposito, “Adaptive Control Strategy for VSC-Based Systems Under Unbalanced Network Conditions,” *IEEE Trans. Smart Grid*, vol. 1, no. 3, pp. 311–319, Dec. 2010.

[67] A. Hadri-Hamida, A. Allag, M. Y. Hammoudi, S. M. Mimoune, S. Zerouali, M. Y. Ayad, M. Becherif, E. Miliani, and A. Miraoui, "A nonlinear adaptive backstepping approach applied to a three phase PWM AC–DC converter feeding induction heating," *Commun. Nonlinear Sci. Numer. Simul.*, vol. 14, no. 4, pp. 1515–1525, Apr. 2009.

[68] Dae-Keun Choi, Duk-Hong Kang, and Kyo-Beum Lee, "A novel gain scheduling method for distributed power generation systems with a LCL-filter by estimating grid impedance," in *2010 IEEE International Symposium on Industrial Electronics*, 2010, pp. 3438–3443.

[69] J. R. Massing, M. Stefanello, H. A. Grundling, and H. Pinheiro, "Adaptive Current Control for Grid-Connected Converters With LCL Filter," *IEEE Trans. Ind. Electron.*, vol. 59, no. 12, pp. 4681–4693, Dec. 2012.

[70] G. Escobar, A. M. Stankovic, and P. Mattavelli, "An Adaptive Controller in Stationary Reference Frame for D-Statcom in Unbalanced Operation," *IEEE Trans. Ind. Electron.*, vol. 51, no. 2, pp. 401–409, 2004.

[71] F. Gonzalez, G. Garcera, I. Patrao, and E. Figueres, "An Adaptive Control System for Three-Phase Photovoltaic Inverters Working in a Polluted and Variable Frequency Electric Grid," *IEEE Trans. Power Electron.*, vol. 27, no. 10, pp. 4248–4261, 2012.

[72] R. M. Milasi, A. F. Lynch, and Y. W. Li, "Adaptive Control of a Voltage Source Converter for Power Factor Correction," *IEEE Trans. Power Electron.*, vol. 28, no. 10, pp. 4767–4779, 2013.

[73] M. Cespedes, S. Member, J. Sun, and S. Member, "Adaptive Control of Grid-Connected Inverters Based on Online Grid Impedance Measurements," *IEEE Trans. Sustain. Energy*, vol. 5, no. 2, pp. 516–523, 2014.

[74] L. A. Zadeh, "Is there a need for fuzzy logic?," *Inf. Sci. (Ny).*, vol. 178, no. 13, pp. 2751–2779, Jul. 2008.

[75] M. A. Azzouz, H. E. Farag, and E. F. El-Saadany, "Real-Time Fuzzy Voltage Regulation for Distribution Networks Incorporating High Penetration of Renewable Sources," *IEEE Syst. J.*, pp. 1–10, in press, 2015.

[76] D. H. Spatti, I. N. da Silva, W. F. Usida, and R. A. Flauzino, "Real-Time Voltage Regulation in Power Distribution System Using Fuzzy Control," *IEEE Trans. Power Deliv.*, vol. 25, no. 2, pp. 1112–1123, Apr. 2010.

[77] F. Milano, "Hybrid Control Model of Under Load Tap Changers," *IEEE Trans. Power Deliv.*, vol. 26, no. 4, pp. 2837–2844, Oct. 2011.

[78] B. Kasztenny, E. Rosolowski, J. Izykowski, M. M. Saha, and B. Hillstrom, "Fuzzy logic controller for on-load transformer tap changer," *IEEE Trans. Power Deliv.*, vol. 13, no. 1, pp. 164–170, 1998.

[79] E. Demirok, P. C. González, K. H. B. Frederiksen, D. Sera, P. Rodriguez, and R. Teodorescu, "Local Reactive Power Control Methods for Overvoltage Prevention of Distributed Solar Inverters in Low-Voltage Grids," *IEEE J. Photovoltaics*, vol. 1, no. 2, pp. 174–182, Oct. 2011.

[80] B. A. Robbins, C. N. Hadjicostis, and A. D. Dominguez-Garcia, "A Two-Stage Distributed Architecture for Voltage Control in Power Distribution Systems," *IEEE Trans. Power Syst.*, vol. 28, no. 2, pp. 1470–1482, May 2013.

[81] C. S. Cheng, "A modified Newton method for radial distribution system power flow analysis," *IEEE Trans. Power Syst.*, vol. 12, no. 1, pp. 389–397, 1997.

[82] N. R. Ullah, K. Bhattacharya, and T. Thiringer, "Wind Farms as Reactive Power Ancillary Service Providers—Technical and Economic Issues," *IEEE Trans. Energy Convers.*, vol. 24, no. 3, pp. 661–672, Sep. 2009.

[83] P. Denholm, J. Jorgenson, M. Hummon, T. Jenkin, and D. Palchak, "The Value of Energy Storage for Grid Applications," *National Renewable Energy Laboratory*, pp. 1–37, 2013.

[84] P. Grbović, *Ultra-Capacitors in Power Conversion Systems*. Chichester, UK: John Wiley & Sons, Ltd, 2013.

[85] A. Yamane, J. Belanger, T. Ise, I. Iyoda, T. Aizono, and C. Dufour, "A Smart Distribution Grid Laboratory," in *IECON 2011 - 37th Annual Conference of the IEEE Industrial Electronics Society*, 2011, pp. 3708–3712.

[86] "RT-LAB Version 10.4 User Guide." [Online]. Available: http://www.opal-rt.com/sites/default/files/RT-LAB_UG(1).pdf.

[87] P. Venne, J.-N. Paquin, and J. Bélanger, "The What, Where and Why of Real-Time Simulation," in *2010 IEEE PES General Meeting Tutorial_04*, 2010, pp. 37–49.

[88] O. Crăciun, A. Florescu, I. Munteanu, A. I. Bratcu, S. Bacha, and D. Radu, "Hardware-in-the-loop simulation applied to protection devices testing," *Int. J. Electr. Power Energy Syst.*, vol. 54, pp. 55–64, Jan. 2014.

[89] J.-N. Paquin, C. Dufour, and B. Jean, "A Hardware-In-the-Loop Simulation Platform for Prototyping and Testing of Wind Generator Controllers," in *CIGRÉ Canada, Conference on Power Systems*, 2008, pp. 1–5.

[90] C. Dufour and J. Belanger, "On the Use of Real-Time Simulation Technology in Smart Grid Research and Development," *IEEE Trans. Ind. Appl.*, vol. 50, no. 6, pp. 3963–3970, 2014.

[91] F. Bignucolo, R. Caldon, and V. Prandoni, "Radial MV networks voltage regulation with distribution management system coordinated controller," *Electr. Power Syst. Res.*, vol. 78, no. 4, pp. 634–645, Apr. 2008.

[92] A. Sasitharanuwat, W. Rakwichian, N. Ketjoy, and S. Yammen, "Performance evaluation of a 10kWp PV power system prototype for isolated building in Thailand," *Renew. Energy*, vol. 32, no. 8, pp. 1288–1300, Jul. 2007.

[93] J. A. Jardini, C. M. V. Tahan, M. R. Gouvea, S. U. Ahn, and F. M. Figueiredo, "Daily load profiles for residential, commercial and industrial low voltage consumers," *IEEE Trans. Power Deliv.*, vol. 15, no. 1, pp. 375–380, 2000.

[94] M. A. Azzouz, M. F. Shaaban, and E. F. El-Saadany, "Real-Time Optimal Voltage Regulation for Distribution Networks Incorporating High Penetration of PEVs," *IEEE Trans. Power Syst.*, vol. 30, no. 6, pp. 3234–3245, 2015.

[95] P. Kundur, *Power System Stability and Control*. McGraw-Hill Professional, 1994.

[96] Keliang Zhou and Danwei Wang, "Relationship between space-vector modulation and three-phase carrier-based PWM: a comprehensive analysis [three-phase inverters]," *IEEE Trans. Ind. Electron.*, vol. 49, no. 1, pp. 186–196, 2002.

[97] M. K. Kazimierczuk, *Pulse-width Modulated DC-DC Power Converters*. John Wiley & Sons, 2008.

[98] M. F. Shaaban and E. F. El-Saadany, "Probabilistic modeling of PHEV charging load in distribution systems," in *2013 3rd International Conference on Electric Power and Energy Conversion Systems*, 2013, pp. 1–6.

[99] *Communication Networks and Systems in Substations - Part 5: Communication Requirements for Functions and Device Models*. IEC 61850-5 ed2, 2003.

[100] D. Singh, R. K. Misra, and D. Singh, "Effect of Load Models in Distributed Generation Planning," *IEEE Trans. Power Syst.*, vol. 22, no. 4, pp. 2204–2212, Nov. 2007.

[101] "Ontario energy board, Title: Distribution system code, Last Updated: June 2013, URL http://www.ontarioenergyboard.ca /OEB/ Documents/Regulatory/ Distribution System Code.pdf." .

[102] J. H. R. Enslin and P. J. M. Heskes, "Harmonic Interaction Between a Large Number of Distributed Power Inverters and the Distribution Network," *IEEE Trans. Power Electron.*, vol. 19, no. 6, pp. 1586–1593, Nov. 2004.

[103] M. Liserre, R. Teodorescu, and F. Blaabjerg, "Stability of photovoltaic and wind turbine grid-connected inverters for a large set of grid impedance values," *IEEE Trans. Power Electron.*, vol. 21, no. 1, pp. 263–272, Jan. 2006.

[104] P. Young, H. Garnier, and M. Gilson, "An optimal instrumental variable approach for identifying hybrid continuous-time Box-Jenkins models," in *System Identification*, 2006, vol. 14, no. 1, pp. 225–230.

[105] H. Garnier and L. Wang, Eds., *Identification of Continuous-time Models from Sampled Data*. London: Springer London, 2008.

[106] G. P. Rao and H. Unbehauen, "Identification of continuous-time systems," *IEE Proc. - Control Theory Appl.*, vol. 153, no. 2, pp. 185–220, Mar. 2006.

[107] L. Ljung, *System Identification: Theory for the User (2nd Edition)*. Prentice Hall, 1999.

[108] M. A. Azzouz and E. F. El-Saadany, "Multivariable Grid Admittance Identification for Impedance Stabilization of Active Distribution Networks," *IEEE Trans. Smart Grid*, pp. 1–13, in press, 2015.

[109] S. Sastry and M. Bodson, *Adaptive Control: Stability, Convergence And Robustness*. Dover Publications, 2011.

[110] X. Liu, J. Wang, and W. X. Zheng, "Convergence analysis of refined instrumental variable method for continuous-time system identification," *IET Control Theory Appl.*, vol. 5, no. 7, pp. 868–877, May 2011.

[111] G. Tao, *Wiley: Adaptive Control Design and Analysis - Gang Tao*. Wiley-IEEE Press, 2003.

[112] L. Asiminoaei, R. Teodorescu, F. Blaabjerg, and U. Borup, "Implementation and Test of an Online Embedded Grid Impedance Estimation Technique for PV Inverters," *IEEE Trans. Ind. Electron.*, vol. 52, no. 4, pp. 1136–1144, Aug. 2005.

[113] P. C. Young, "Optimal IV identification and estimation of continuous-time TF models," in *World Congress*, 2002, vol. 15, no. 1, p. 1002.

[114] S. Bolognani, L. Tubiana, and M. Zigliotto, "Extended Kalman Filter Tuning in Sensorless PMSM Drives," *IEEE Trans. Ind. Appl.*, vol. 39, no. 6, pp. 1741–1747, 2003.

[115] Z. Shen, M. Jaksic, P. Mattavelli, D. Boroyevich, J. Verhulst, and M. Belkhayat, "Three-phase AC system impedance measurement unit (IMU) using chirp signal injection," in *2013 Twenty-Eighth Annual IEEE Applied Power Electronics Conference and Exposition (APEC)*, 2013, pp. 2666–2673.

[116] M. A. Azzouz and E. F. El-Saadany, "Multivariable DG Impedance Modeling and Reshaping for Impedance Stabilization of Active Distribution Networks," *to be Submitt. to IEEE Trans. Power Syst.*, 2015.

[117] K. Deb, *Multi-Objective Optimization Using Evolutionary Algorithms*, 1st ed. John Wiley & Sons, 2001.